UNIVERSITA’ DEGLI STUDI DI NAPOLI
FEDERICO II FACOLTA’ DI SCIENZE MM.FF.NN.

CORSO DI LAUREA IN FISICA
Anno Accademico 2008/2009

PhD Thesis

A SEARCH FOR THE $B \rightarrow \tau\nu$ RARE DECAY WITH THE BABAR EXPERIMENT

RELATORI:

Prof. Crisostomo Sciacca
Dr. Guglielmo De Nardo

CANDIDATO:

Giovanni Onorato

A Carmen, niente di tutto questo senza di lei

Contents

Introduction

The present work has been developed at the I.N.F.N. section of Napoli, within the BABAR collaboration. The BABAR experiment is an high energy physics experiment installed at the SLAC laboratory of the Stanford University in Menlo Park, CA (USA). The linear collider PEP-II accelerates a beam of electrons and a beam of positrons. The two beams are injected in a circular path (ring), and collide at the energy of the $\Upsilon(4S)$ resonance, which decays mainly in a B mesons pair. The energy of the two beams is different (asymmetric beams) in order to have a boost of the center of mass. At the intersection of the beam the detector is installed with the purpose to reconstruct the physics event from its decay products, charged and neutral. Our analysis consists in the measurement of the $B \to \tau\nu$ decay Branching Fraction. It is based on the full BABAR dataset, corresponding to $(467.8 \pm 5.1) \times 10^6$ pairs of $B\bar{B}$, collected at the energy of the $\Upsilon(4S)$ resonance from 1999 to 2007. The measurement has been already performed by the Napoli BABAR group using a smaller data set and the results have been published in 2008 [1], measuring a Branching Fraction of $(1.8 \pm 0.9(\text{stat.}) \pm 0.4(\text{bkg syst.}) \pm 0.2(\text{other syst.})) \times 10^{-4}$. The BABAR collaboration performed another analysis, using a different strategy that provides a totally independent data sample [2], measuring $\mathcal{B}(B \to \tau\nu\ ) = (1.6^{+0.8}_{-0.7}(\text{stat.}) \pm 0.1(\text{syst.})) \times 10^{-4}$. The combined result from the BABAR collaboration is $(1.7 \pm 0.6) \times 10^{-4}$. From the Standard Model (SM) prediction:

$$\mathcal{B}(B^- \to l^-\bar{\nu}) = \frac{G_F^2 m_B}{8\pi} m_l^2 \left(1 - \frac{m_l^2}{m_B^2}\right)^2 f_B^2 |V_{ub}|^2 \tau_B, \tag{1}$$

we can extract the product $f_B|V_{ub}|$, where f_B is the B meson decay constant, estimated only by lattice QCD simulation, and $|V_{ub}|$ is the CKM matrix element absolute value measured from B semileptonic decays. The branching fraction is also sensitive to physics beyond the Standard Model. For example, in the Two Higgs Doublet Model [3], the $B \to \tau\nu$ Branching Fraction can be expressed as:

$$\mathcal{B}_{(B\to\tau\nu)} = \mathcal{B}_{SM} \times \left(1 - \tan^2\beta \frac{m_{B^\pm}^2}{m_{H^\pm}^2}\right). \tag{2}$$

where $\tan\beta$ is the ratio of the vacuum expectation values of the two Higgs fields and m_H is the mass of the charged Higgs. Using this relation, we can impose constraints on the charged Higgs mass and on the value of $\tan\beta$.

Experimentally, we reconstruct for each event a B meson (B_{tag}) by means of its hadronic decay modes. We look for evidence of a $B \to \tau\nu$ decay in the rest of the event, searching for the four main decay channels of the τ lepton, which comprise the 71.6% of its decay modes: $\tau \to e\nu\bar{\nu}$, $\tau \to \mu\nu\bar{\nu}$, $\tau \to \pi\nu$ and $\tau \to \rho\nu$. We apply the same reconstruction procedure both to the experimental data sample and to Monte

Carlo simulated events samples. We simulate the detector response to signal events and the most important sources of backgrounds:

- $\Upsilon(4S) \to B^+B^-, \quad B^+ \to \tau^+\nu_\tau, \quad B^- \to$ generic,
- $\Upsilon(4S) \to B^+B^-, \quad B^\pm \to$ generic,
- $\Upsilon(4S) \to B^0\bar{B}^0$,
- $e^+e^- \to c\bar{c}$
- $e^+e^- \to u\bar{u}, \quad d\bar{d}, \quad s\bar{s}$
- $e^+e^- \to \tau^+\tau^-$

We calculate for each B_{tag} the mass of the B from the momenta of its decay products, using the beam energy constraint (m_{ES}). The different sources of background can be classified in the followin categories:

- the *"continuum"* background, from $e^+e^- \to q\bar{q}$ and $e^+e^- \to \tau^+\tau^-$ events. They do not peak in the m_{ES} distribution.
- the *"combinatoric"* background, with an erroneous reconstruction of B^+B^- or $B^0\bar{B}^0$ events, due incorrect assignement of tracks and neutral clusters. The m_{ES} distribution for this background does not peak.
- B^+B^- events where the charged B_{tag} is correctly reconstructed. In this case the m_{ES} distribution peaks around the B mass value ($\sim 5.27\,\text{GeV}/c^2$).

We evaluate the non-peaking component (*continuum* and *combinatoric* background) using a sub-sample of real data from the lower sideband of the m_{ES} distribution ($5.209\,\text{GeV}/c^2 < m_{ES} < 5.26\,\text{GeV}/c^2$), while we evaluate the peaking component using the B^+B^- Monte Carlo simulation. We apply selection requirements to enhance $B \to \tau\nu$ events in data and reject background events, using two discriminators. To suppress the non-peaking background we evaluate a *Likelihood Ratio*, based on B_{tag} reconstruction observables. To suppress the peaking background we tried several possible discriminators (also combining them in a multivariate analysis). We conclude that for "one prong" decays we obtain the same sensitivity using only the center mass system momentum of the τ daughter particle. We calculate, indeed, a *Likelihood Ratio* based on B_{sig} reconstruction related variables for the $\tau^- \to \rho^-\nu$ channel. In the signal event selection we do not use the most discriminating variable, that is the energy of the charged tracks and the neutral clusters not assigned to any reconstructed B (E_{extra}), but we evaluate the branching fraction fitting this variable's distribution. We optimize the selection requirements minimizing the expected uncertainty in the branching fraction fit results. We determine the uncertainties for each configuration of selection requirements, by means of toy experiments generated from the known E_{extra} probability density functions of signal and background. In order to take into account known data/Monte Carlo disagreements in E_{extra} shapes we use data and Monte Carlo control samples of $\Upsilon(4S) \to B^+B^-$ events, where both B mesons are reconstructed in hadronic decays, or one in hadronic one in semileptonic. In the selection optimization we take into account systematic uncertainties: the first is due to the Data/MonteCarlo corrections we found in the control sample, the second is due to the error on the Monte Carlo simulation used to extract the E_{extra} shapes. It is a protocol for the BABAR analysies, when possible, to avoid examining the real data in the region where one expects to find signal events (*blind procedure*). A review commette of the BABAR collaboratin is intended to check the analysis procedure. After the approval of the committe we will look at the signal region in data and fit the E_{extra} distribution to extract the final measurement.

The present document is composed of four chapters. In the first chapter we introduce the theoretical background of the $B \to \tau\nu$ decay,: an introduction to the Standard Model and the CKM matrix, the leptonic B decay theory and the $B \to \tau\nu$ branching fraction expression, in the Standard Model and in New Physics. The second chapter introduces the BABAR experiment with the description of the PEP-II collider and the BABAR detector. The tracks and neutral candidate reconstruction alghorithms used in the analysis are then described. In the third chapter we describe the B tagging techinque, the preliminary requirements we apply before the selection and the identification and calculation of the discriminators we use in the selection. In the fourth chapter we discuss the optimization of the selection requirements, and present the calculation of the expected systematic and statistical uncertainties, with a given hypotesis on the branching fraction. Last chapter describes the technique we will use to extract the final measurement.

Chapter 1

The Standard Model and the leptonic decays of the B mesons

This chapter is intended to give a theoretical framework to the study of the leptonic decays of B mesons in the Standard Model and in models of New Physics. The Cabibbo-Kobayashi-Maskawa matrix will be introduced together with the phenomenology of electro-weak interactions. Particular parameterizations of the CKM matrix are shown, in order to identify the unitary triangle. The leptonic decay of the B mesons, although theoretically simple and the absence of strong interactions in the final state, give access to the strong interactions that take place inside the parent meson. Infact these decays are sensitive to the B meson decay constant f_B only known from theory. Last part of the chapter is about the possible consequences of the $B \to \tau\nu$ decay in models of New Physics.

1.1 Introduction to the Standard Model

The Fermi's theory of the weak interaction (1934) for leptons was QED like modelled at low energy as:

$$\mathcal{L}_F = \frac{G}{\sqrt{2}} J_\alpha J^{\alpha\,\dagger} \tag{1.1}$$

that is a contact interaction between currents:

$$J_\alpha = \bar{\psi}_e \gamma_\alpha (1-\gamma_5)\psi_\nu = 2\bar{e}_L \gamma_\alpha \nu_\alpha \tag{1.2}$$

where $\psi_e \equiv e$ is a Dirac spinor and $(1-\gamma_5)/2$ is the left-handed chiral projection operator:

$$e_L = \frac{(1-\gamma_5)}{2} e. \tag{1.3}$$

i.e. only left-handed particles are involved in the theory. Each chiral projection is a combination of both positive and negative helicity states and only in the relativistic limit a left-handed 1/2-spin particle become a pure $-1/2$ helicity state. All this is a consequence of the so-called $V-A$ (Vector and Axial currents) theory. In fact, as the weak interactions are parity-violating a non-invariant under parity transformation term was needed [4] [5]. Among all the possibles bi-linear Lorentz-invariant forms only the $V - A$ combination produces particles with the left chirality and maximises the parity violation [6].

In the Standard Model with three generations of quarks and leptons [7], the weak interaction can be written, according to the gauge principle, starting from the free Lagrangian:

$$\mathcal{L}_0 = \sum_i \left(i\bar{L}_i \partial\!\!\!/ L_i + i\bar{R}_i \partial\!\!\!/ R_i \right) \qquad i = 1, 2, 3 \tag{1.4}$$

where$\partial\!\!\!/ = \gamma^\mu \partial_\mu$ and:

$$L_1 = \begin{pmatrix} \nu_e \\ e_L \end{pmatrix} \quad L_2 = \begin{pmatrix} \nu_\mu \\ \mu_L \end{pmatrix} \quad L_3 = \begin{pmatrix} \nu_\tau \\ \tau_L \end{pmatrix} \tag{1.5}$$

$$R_1 = e_R \qquad R_2 = \mu_R \qquad R_3 = \tau_R \tag{1.6}$$

where L and R stands for the left- and right-handed fields. This Lagrangian has two symmetries. The first is the $U(1)$ ipercharge symmetry Y (-1 for the left-handed fields and -2 for the right-handed fields):

$$L(x) \rightarrow L'(x) = e^{g' \frac{i}{2} Y \alpha} L(x) \qquad R(x) \rightarrow R'(x) = e^{g' \frac{i}{2} Y \alpha} R(x). \tag{1.7}$$

The second is the isotopic $SU(2)$ symmetry that has the Pauli's matrices $\vec{\tau}_i$ as generators:

$$L(x) \rightarrow L'(x) = e^{g \frac{i}{2} \vec{\tau} \cdot \vec{\omega}} \qquad R(x) \rightarrow R'(x) = R(x). \tag{1.8}$$

The theory is invariant under these global transformations (α and $\vec{\omega}$ are constants) and the extension of the invariance can be obtained by substituting $\alpha \rightarrow \alpha(x)$ and $\vec{\omega} \rightarrow \vec{\omega}(x)$ which allows to build a gauge theory.

The interactions are built defining a covariant derivative for each symmetry of the Lagrangian. The electroweak interaction can be written as:

$$\mathcal{L}_{int}^{EW} = \mathcal{L}_{CC} + \mathcal{L}_{NC} \tag{1.9}$$

where $\mathcal{L}_{CC}$ and $\mathcal{L}_{NC}$ are the charged and neutral interaction currents. The quark flavour changing transitions are governed by:

$$\mathcal{L}_{CC} = \frac{g}{2\sqrt{2}} (J_\mu W^{+\mu} + J_\mu^\dagger W^{-\mu}) \tag{1.10}$$

where

$$J_\mu = (\bar{u}d')_{V-A} + (\bar{c}s')_{V-A} + (\bar{t}b')_{V-A} + (\bar{\nu_e} e)_{V-A} + (\bar{\nu_\mu} \mu)_{V-A} + (\bar{\nu_\tau} \tau)_{V-A} \tag{1.11}$$

is the charged current and g is the $SU(2)_L$ coupling constant. For the quark sector one has:

$$J_\mu = \sum_{ij} V_{ij} J_{ij}^\mu = \sum_{ij} \bar{u}_i \gamma^\mu \frac{1}{2} (1 - \gamma_5) V_{ij} d_j \tag{1.12}$$

where V_{ij} are the elements of a unitary 3×3 matrix called Cabibbo-Kobayashi-Maskawa matrix (see below), the indices i, j run over the three quark generations and the field operators u_i, d_j and $W^{+\mu}$ annihilate u, c, t, d, s, b and a W respectively.

Interactions in the Standard Model, will be described by the gauge symmetry $SU(3)_C \otimes SU(2)_L \otimes U(1)_Y$ that is spontaneously broken into

$$SU(3)_C \otimes SU(2)_L \otimes U(1)_Y \longrightarrow SU(3)_C \otimes U(1)_Q \tag{1.13}$$

where Y and Q are the weak ipercharge and the electric charge respectively. $SU(3)_C$ [8] is the gauge symmetry for the QCD, whose generators for the quarks are represented by the Gell'Mann matrices λ^a. The theory is governed by the Lagrangian:

$$\mathcal{L} = \mathcal{L}(QCD) + \mathcal{L}(SU(2)_L \otimes U(1)_Y) + \mathcal{L}(Higgs) \tag{1.14}$$

The strong interactions are mediated by the eight gluons G_a, the weak interactions by the $W^{\pm}$, Z^0 and γ bosons and the Higgs neutral boson H^0.

In the Standard Model, quarks and leptons are arranged in $SU(2)_L$ left-handed doublets:

$$\begin{pmatrix} \nu_e \\ e- \end{pmatrix}_L \quad \begin{pmatrix} \nu_\mu \\ \mu^- \end{pmatrix}_L \quad \begin{pmatrix} \nu_\tau \\ \tau^- \end{pmatrix}_L \tag{1.15}$$

$$\begin{pmatrix} u \\ d' \end{pmatrix}_L \quad \begin{pmatrix} c \\ s' \end{pmatrix}_L \quad \begin{pmatrix} t \\ b' \end{pmatrix}_L \tag{1.16}$$

while the corresponding right-handed fields are singlets under $SU(2)_L$. The flavour of the quarks is conserved in all vertexes with neutral gauge bosons, Z^0, γ and G. Charged current processes involving $W^{\pm}$ bosons, are flavour violating and the intensity of such violation is given by the gauge coupling constant g. This coupling is relatoed to the Fermi constant by

$$\frac{G_F}{\sqrt{2}} = \frac{g^2}{8M_W^2} \tag{1.17}$$

and by the unitary 3×3 matrix CKM (Cabibbo, Kobayashi, Maskawa [9, 10]) connects the weak eigenstates (d', s', b') and the corresponding mass eigenstates (d, s, b):

$$\begin{pmatrix} d' \\ s' \\ b' \end{pmatrix} = \begin{pmatrix} V_{ud} & V_{us} & V_{ub} \\ V_{cd} & V_{cs} & V_{cb} \\ V_{td} & V_{ts} & V_{tb} \end{pmatrix} \begin{pmatrix} d \\ s \\ b \end{pmatrix} = \hat{V}_{CKM} \begin{pmatrix} d \\ s \\ b \end{pmatrix} \tag{1.18}$$

The same mixing matrix for the leptons would be the unit matrix in the hypothesis of null neutrino masses.

The fermion masses are fundamental theoretical inputs of the Standard Model whose values could also account for new physics. However both the fermion masses and the CKM elements values are originated by the fermion couplings with the Higgs field. The coupling of the Higgs field to the quarks are given by the Yukawa coupling under the $SU(2)_L$ gauge symmetry:

$$\mathcal{L}_{Yukawa} = \sum_{j,k} \left[Y_{jk} (\bar{u}_L^j, \bar{d}_L^j) \begin{pmatrix} \phi^0 \\ -\phi^+ \end{pmatrix}^* u_R^k Y_{jk'} (\bar{u}_L^j, \bar{d}_L^j) \begin{pmatrix} \phi^+ \\ \phi^0 \end{pmatrix}^* d_R^k + h.c. \right] \tag{1.19}$$

where $i, j = 1, 2, 3$ are the quark generations and Y_{jk} and $Y_{jk'}$ are the Yukawa couplings. The Higgs doublets symmetry is spontaneously broken:

$$\begin{pmatrix} \phi^+ \\ \phi^0 \end{pmatrix} \rightarrow \frac{1}{\sqrt{2}} \begin{pmatrix} 0 \\ v + H(x) \end{pmatrix}, \tag{1.20}$$

where v is the Higgs expectation value and $H(x)$ is the Higgs particle field. After the symmetry breaking the 1.19 become:

$$\mathcal{L}_{Yukawa} = \sum_{j,k} \left[Y_{jk} \bar{u}^j_L u^k_R + Y_{jk}\prime \bar{d}^j_L d^k_R + h.c. \right] \frac{1}{\sqrt{2}} (v + H(x)). \tag{1.21}$$

The terms proportional to v couple the left- and right-handed components of the quark fields and generate the mass terms. To determine the quark mass eigenstates it is necessary to diagonalise the mass matrices:

$$m_{jk} \equiv \frac{-v}{\sqrt{2}} Y_{jk}, \qquad m'_{jk} \equiv \frac{-v}{\sqrt{2}} Y'_{jk}. \tag{1.22}$$

The diagonalization is given by unitary transformations:

$$u^i_{L,R} = \sum_j T^{ij}_{L,R} u'^j_{L,R} \tag{1.23}$$

$$d^i_{L,R} = \sum_J V^{ij}_{L,R} d'^j_{L,R} \tag{1.24}$$

where the apexes represent the mass eigenstates. The quark interaction term becomes:

$$\frac{g}{\sqrt{2}} \bar{u}'_{Li} \gamma^\mu V_{ij} d'_{Lj} W^+_\mu + h.c. \tag{1.25}$$

where $V = T^\dagger_L V_L$ is the CKM unitary matrix.

1.2 The CKM parameterizations

A generic $n \times n$ unitary matrix can be defined by mean of $2n^2$ real parameters. The constraints from unitary conditions can be expressed by n^2 equations:

$$\sum_j V^*_{ij} V_{jk} = \delta_{ik} \tag{1.26}$$

reducing the number of real parameters to n^2. An additional reduction of the parameters number comes from the equation 1.12, where the interaction term appears in the form $\bar{u}_i \gamma^\mu V_{ij} d_j$: the relative field phases of the quark $\bar{u}_i$ and d_j can be redefined in the way to cancel $2n - 1$ parameters of the matrix. In the end we have $(n-1)^2$ free parameters. If we consider two family of quarks, we have 1 free parameter, and the matrix can be written as:

$$V = \begin{pmatrix} \cos\theta_c & \sin\theta_v \\ -\sin\theta_c & \cos\theta_c \end{pmatrix} \tag{1.27}$$

where θ_c is the Cabibbo. This parameter introduces a rotation in the coupling of quarks and can justify the strong suppression of decays with flavour changing neutral current. The Kobayashi and Maskawa idea was to introduce a third generation of quark; the number of parameters is 4, three quark field rotation and a not-removable phase, which is responsable of CP-violation in the Standard Model. The standard parameterization of the CKM matrix [11] is:

$$\hat{V}_{CKM} = \begin{pmatrix} c_{12}c_{13} & s_{12}c_{13} & s_{13}e^{-i\delta_{13}} \\ -s_{12}c_{23} - c_{12}s_{23}s_{13}e^{i\delta_{13}} & c_{12}c_{23} - s_{12}s_{23}s_{13}e^{i\delta_{13}} & s_{23}c_{13} \\ s_{12}s_{23} - c_{12}c_{23}s_{13}e^{i\delta_{13}} & -c_{12}s_{23} - s_{12}c_{23}s_{13}e^{i\delta_{13}} & c_{23}c_{13} \end{pmatrix}, \tag{1.28}$$

where $c_{ij} = \cos\theta_{ij}$, $s_{ij} = \sin\theta_{ij}$ and δ_{13} is the CP-violating phase. The terms c_{ij} and s_{ij} can be chosen positive and δ_{13} can vary in the interval $0 \leq \delta_{13} < 2\pi$. Since $|V_{ub}| \sim 10^{-3}$, c_{13} is really close to 1 and the terms containing s_{13} can be neglected with respect to those close to the unity. The four independent parameters are $s_{12} = |V_{us}|$, $s_{13} = |V_{ub}|$, $s_{23} = |V_{cb}|$ and δ_{13}.

A particular representation of the CKM matrix is the Wolfenstein parameterization [12] that is an expansion, inspired by the inequalities $s_{13} < s_{23} < s_{12}$ in terms of the small parameter $\lambda = s_{12} = \sin\theta_{12} = |V_{us}| = 0.22$:

$$\hat{V} = \begin{pmatrix} 1-\frac{\lambda^2}{2} & \lambda & A\lambda^3(\varrho - i\eta) \\ -\lambda & 1-\frac{\lambda^2}{2} & A\lambda^2 \\ A\lambda^3(1-\varrho-i\eta) & -A\lambda^2 & 1 \end{pmatrix} + \mathcal{O}(\lambda^4)\,, \tag{1.29}$$

the four independent parameters are now λ, A, ϱ and η. The connection with the standard parameterization is given by:

$$s_{12} = \lambda, \quad s_{23} = A\lambda^2, \quad s_{13}e^{-i\delta_{13}} = A\lambda^3(\varrho - i\eta) \tag{1.30}$$

And

$$\varrho = \frac{s_{13}}{s_{12}s_{23}}\cos\delta_{13}, \qquad \eta = \frac{s_{13}}{s_{12}s_{23}}\sin\delta_{13} \qquad A = \frac{s_{23}}{s_{12}^2} \tag{1.31}$$

that are the transformation rules between the two sets of physical parameters. The expansion in terms of λ gives the Wolfenstein matrix and the correction to higher orders. It can be shown that V_{ub} does not change in the expansion and that the corrections to V_{us} and V_{cb} occur at $\mathcal{O}(\lambda^7)$ and $\mathcal{O}(\lambda^8)$. So, with an high precision level [13]:

$$V_{us} = \lambda \qquad V_{cb} = A\lambda^2$$
$$V_{ub} = A\lambda^3(\varrho - i\eta) \qquad V_{td} = A\lambda^3(1-\bar{\varrho}-i\bar{\eta})$$

where

$$\bar{\varrho} = \varrho(1-\frac{\lambda^2}{2}) \qquad \bar{\eta} = \eta(1-\frac{\lambda^2}{2}). \tag{1.32}$$

1.2.1 The unitary triangle

The unitary of the CKM matrix implies the existence of relations between the rows and the columns of the matrix itself. The three relations involving the columns are of particular interest:

$$V_{ud}V_{us}^* + V_{cd}V_{cs}^* + V_{td}V_{ts}^* = 0 \tag{1.33}$$
$$V_{us}V_{ub}^* + V_{cs}V_{cb}^* + V_{ts}V_{tb}^* = 0 \tag{1.34}$$
$$V_{ud}V_{ub}^* + V_{cd}V_{cb}^* + V_{td}V_{tb}^* = 0 \tag{1.35}$$

They can be regarded as triangles in the complex plane (ϱ, η) and are called unitary triangles [11, 14, 15]. Figure 1.1 shows the three triangles in an arbitrary scale. The triangles are related to the K, B_s and B_d decays and the shortest side of each triangle is related to CP violating decays. The third triangle is the one of interest for *BABAR* and the opening of the triangle is related to wide effects of CP violation in the B_d meson system.

It can be shown that the triangles have equal area given by $|J|/2$ where J is given by $\Im[V_{ij}V_{kl}V_{il}^*V_{kj}^*] = J\sum_{m,n=1}^{3}\varepsilon_{ikm}\varepsilon_{jln}$ and the sign of J is related to the direction

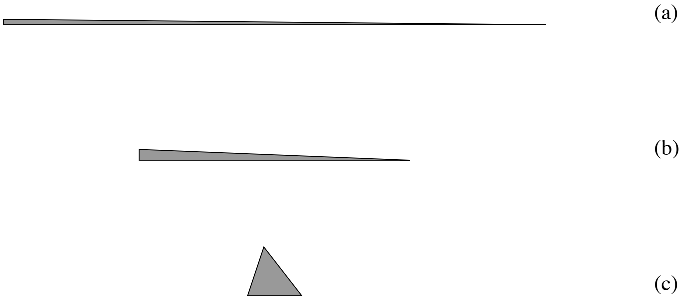

Figure 1.1: The three unitary triangles: (a) $V_{id}V^*_{is} = 0$, (b) $V_{is}V^*_{ib} = 0$, (c) $V_{id}V^*_{ib} = 0$

of the complex vectors. The triangles are invariant under any phase rotation i.e. sides and angles are not modified (the modules of the CKM matrix are constant) and can be considered physical observables.

Let us focus on the third unitary triangle. Given that

$$V_{cd}V^*_{cb} = -A\lambda^3 + \mathcal{O}(\lambda^7) \tag{1.36}$$

with a good approximation $V_{cd}V^*_{cb}$ is real and $|V_{cd}V^*_{cb}| = A\lambda^3$. Retaining the corrections at the $\mathcal{O}(\lambda^5)$ and rescaling the terms into the Equation 1.35 by $A\lambda^3$:

$$\frac{1}{A\lambda^3}V_{ud}V^*_{ub} = \bar{\varrho} + i\bar{\eta}, \qquad \frac{1}{A\lambda^3}V_{td}V^*_{tb} = 1 - (\bar{\varrho} + i\bar{\eta}) \tag{1.37}$$

where $\bar{\varrho}$ and $\bar{\eta}$ are given in the 1.32. The unitary triangle can designed in the complex plane $(\bar{\varrho}, \bar{\eta})$ as shown in Figure 1.2.

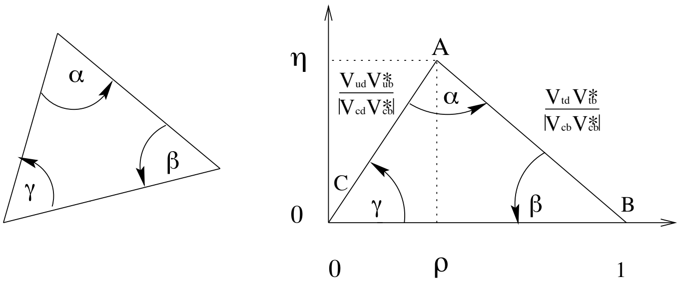

(a) (b)

Figure 1.2: The Unitary Triangle (a) before and (b) after the normalization.

And it is simple to obtain the following relations:

$$\sin(2\alpha) = \frac{2\bar{\eta}(\bar{\eta}^2 + \bar{\varrho}^2 - \bar{\varrho})}{(\bar{\varrho}^2 + \bar{\eta}^2)[(1 - \bar{\varrho})^2 + \bar{\eta}^2]} \tag{1.38}$$

$$\sin(2\beta) = \frac{2\bar{\eta}(1 - \bar{\varrho})}{(1 - \bar{\varrho})^2 + \bar{\eta}^2} \tag{1.39}$$

$$\sin(2\gamma) = \frac{2\bar{\varrho}\bar{\eta}}{(\bar{\varrho}^2 + \bar{\eta}^2)} = \frac{2\varrho\eta}{(\varrho^2 + \eta^2)} \tag{1.40}$$

where α, β and γ are the angles of the Unitary Triangle. The sides CA and BA of the triangle, called R_b and R_t, are given by:

$$R_b \equiv \left|\frac{V_{ud}V_{ub}^*}{V_{cd}V_{cb}^*}\right| = \sqrt{\bar{\varrho}^2+\bar{\eta}^2} = (1-\frac{\lambda^2}{2})\frac{1}{\lambda}\left|\frac{V_{ud}}{V_{cb}}\right| \tag{1.41}$$

$$R_t \equiv \left|\frac{V_{td}V_{tb}^*}{V_{cd}V_{cb}}\right| = \sqrt{(1-\bar{\varrho}^2)+\bar{\eta}^2} = \frac{1}{\lambda}\left|\frac{V_{td}}{V_{cb}}\right| . \tag{1.42}$$

The angles β and γ are directly related to V_{td} and V_{ub}:

$$V_{td} = |V_{td}|e^{-i\beta}, \qquad V_{ub} = |V_{ub}|e^{-i\gamma} . \tag{1.43}$$

The angle α is simply $\alpha+\beta+\gamma = 180°$. The triangle in Figure 1.2 together with $|V_{us}|$ and $|V_{cb}|$ provide a complete description of the CKM matrix and the CP-violating condition is $\eta \neq 0$, or, the area of the triangle ($|J|/2$) must be not zero.

Using the known values of the CKM parameters it possible to extract directly R_b. This gives a constraint on the position of the triangle vertex A, as shown in Figure 1.3

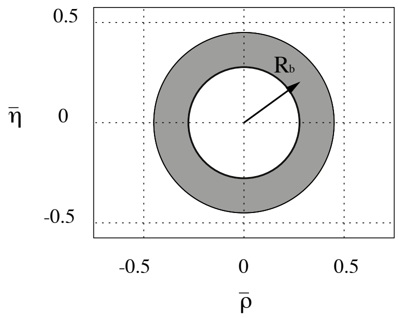

Figure 1.3: The unitary clock.

1.3 The theory of the leptonic decays

The purely leptonic decays $B^- \to \ell^-\bar{\nu}$ are of particular interest in the B mesons physics scenario due to their relatively simple theoretical description which gives access to the strong interactions binding the quarks in the initial state meson while there are no strong interactions in the final state. Moreover, the leptonic decays of the B mesons are characterised by a rather clean experimental signature.

The Feynman diagram for a B^+ leptonic decay is shown in Figure 1.4.

The B meson of mass m_B and four momentum p contains a $u\bar{b}$ pair that annihilates into a W going into a lepton-neutrino couple. The CKM element V_{ub} enters into the annihilation vertex and the four-momentum q_μ of the W is forced to be $q_\mu = p_\mu$ and $q^2 = m_B^2$.

Since the final lepton-neutrino system do not interact strongly, the matrix element can be factorised into an hadronic and a leptonic current:

$$\mathcal{M} = \frac{G_F^2 m_B}{\sqrt{2}} V_{ub}\langle 0|J_\mu|B\rangle \bar{u}(k,\sigma)\gamma_\mu(1-\gamma_5)\nu(p,s) \tag{1.44}$$

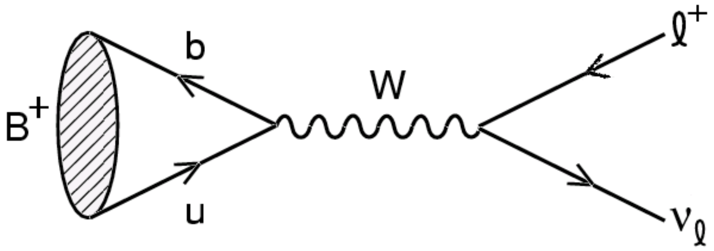

Figure 1.4: Feynman diagram for a B^+ leptonic decay.

where u and ν are the lepton and neutrino Dirac spinors. In the hadronic current, the only available quantity is the B meson four-vector p_μ and the current J_μ, even in the form $V - A$, contributes with an axial term only. The hadronic current finally become:

$$\langle 0|\bar{u}\gamma_\mu\gamma_5 b|P(p)\rangle = i f_B p_\mu, \tag{1.45}$$

where f_B is the B meson decay constant that, alone, is determined by strong interactions. Using 1.44 and 1.45 it is easy to obtain the branching fraction:

$$\mathcal{B}(B^- \to \ell^-\bar{\nu}) = \frac{G_F^2 m_B}{8\pi} m_l^2 \left(1 - \frac{m_l^2}{m_B^2}\right)^2 f_B^2 |V_{ub}|^2 \tau_B, \tag{1.46}$$

where G_F is the Fermi coupling constant, m_l and m_B are the lepton and the B meson masses, τ_B is the B^- lifetime. The dependence of $\mathcal{B}(B^- \to \ell^-\bar{\nu})$ on the lepton mass arises from helicity suppression so that low mass leptons are disfavoured with respect to high mass leptons. The ratio between the rates for the lepton species $\tau : \mu : e$ is $\sim 1 : 5 \times 10^{-3} : 10^{-7}$ which makes the τ channel the most favourite. In the Standard Model context, the observation of $B^- \to l^-\bar{\nu}$ provides a first direct measurement of f_B, as $|V_{ub}|$ is measured from semi-leptonic B meson decays. On the other hand, if f_B is calculate precisely from lattice QCD, the branching fraction would provide precise measurement of $|V_{ub}|$. The ratio between CMK parameters $|V_{ub}/V_{td}|$ can be obtained by comparing $\mathcal{B}(B^- \to l^-\bar{\nu})$ with the difference in heavy and light neutral B_d masses (Δm_d), known from B_d mixing measurements with considerable precision [16]. The mass difference Δm_d is given by:

$$\Delta m_d = \frac{G_F^2}{6\pi^2} \eta_B m_B m_W^2 f_B^2 B_B S_0(x_T) |V_{td}|^2 \tag{1.47}$$

where B_B is the "bag parameter" which arises from the vacuum insertion approximation, η_B is the QCD correction factor which depends on Λ_{QCD} and the masses m_b and m_t, and S_0 is the Inami-Lim function. In the comparison between Eq. 1.46 and Eq. 1.47, the dependence on the poorly known decay constant f_B drops out and we obtain

$$\frac{\mathcal{B}(B^- \to l^-\bar{\nu})}{\Delta m_d} = \frac{3\pi}{4} \frac{m_l^2 (1 - \frac{m_l^2}{m_B^2}) \tau_B |V_{ub}|^2}{\eta_B m_W^2 B_B S_o(t) |V_{td}|^2}, \tag{1.48}$$

which can be used to map out an allowed zone in the Wolfenstein ρ and η parameter [12]. In fig. 1.5 we report the constraints on the unitary triangle from the last measured values of Δm_d parameter.

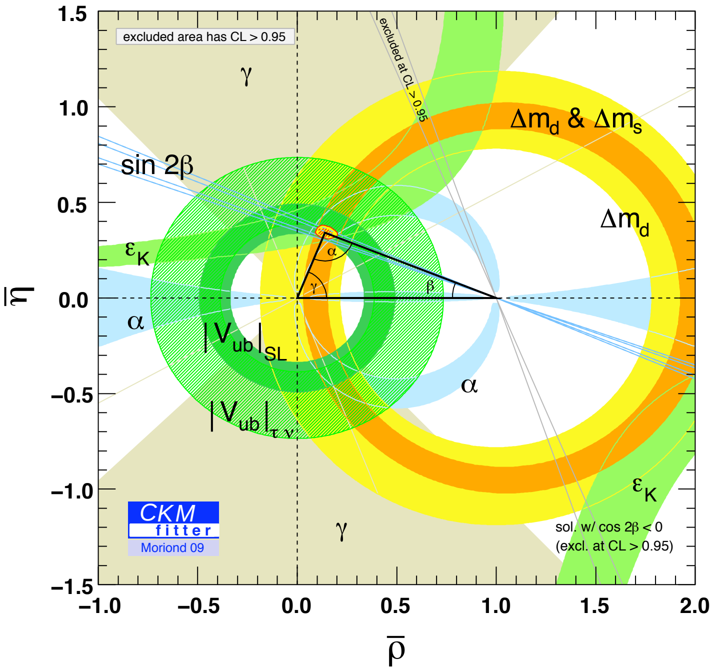

Figure 1.5: Constraints on unitary triangle from CKMFitter Collaboration [17]. The shaded green circle comes from the $|V_{ub}|$ calculation from $B \to \tau\nu$, assuming f_B from lattice QCD; the light yellow circle comes from Δm_d indirect measurement.

Exploiting the PDG 2009 [16] values for τ_B and for $|V_{ub}|$ and the HPQCD collaboration value for f_B [18], the Standard Model expectation in Eq. (1.46) for the τ channel branching fraction becomes [19]:

$$\mathcal{B}(B \to \tau\nu) = (1.29 \times 10^{-4}) \frac{\tau_B}{1.638\text{ps}} \left(\frac{f_B}{216\,\text{MeV}} \right)^2 \left| \frac{V_{ub}}{0.00395} \right|^2 \tag{1.49}$$

that clearly shows how this decay is sensitive to the CKM matrix element V_{ub} and the B meson decay constant f_B. Despite the theoretically clean dependence on relevant parameters, the experimental situation is more involved. The muon channel is experimentally simpler (a monochromatic muon in the B rest frame) but the helicity suppression makes the process quite rare ($\sim 4 \times 10^{-7}$). The τ channel is far more abundant but the necessity to reconstruct the τ lepton from its decay products and the presence of two or three undetectable neutrinos in the final state makes the background rejection an experimental challenge.

At the present moment BABAR has reported a combined result from two independent analysis [2, 1] of:

$$\mathcal{B}(B \to \tau\nu) = (1.7 \pm 0.6) \times 10^{-4} \tag{1.50}$$

while the Belle Collaboration reported [20]

$$\mathcal{B}(B \to \tau\nu) = (1.65^{+0.38}_{-0.37}(\text{stat})^{+0.35}_{-0.37}(\text{syst})) \times 10^{-4}. \tag{1.51}$$

Both results are consistent with the Standard model predictions.

1.4 The $B \to \tau\nu$ decay in New Physics models

The $B \to \tau\nu$ decay has a important impact in model beyond the Standar Model because it allows to constraint parameter of the New Physics. In the two Higgs doublet model the decay involves the contribution of a charged Higgs at tree level, as show in the diagram in fig.1.6. We shall consider the so-called model II of two higgs doublet models [3], where u-type quarks get mass from one doublet, while d-type quarks get mass from the other doublet. Charged Higgs Yukawa couplings are controlled by the parameter $tan\beta = v_2/v_1$, the ratio of vacuum expectation values of the two doublets. The $W^{\pm}$ and $H^{\pm}$ effectively induce the the four-Fermi interaction

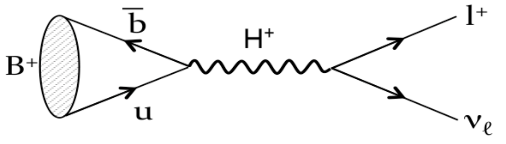

Figure 1.6: Tree level diagram of $B \to \tau\nu$ decay through a cherged Higgs

$$\frac{G_f}{\sqrt{2}}V_{ib}([\bar{u}_i\gamma_u(1-\gamma_5)b][\bar{l}\gamma_u(1-\gamma_5)\nu] - R_l[\bar{u}_i(1+\gamma_5)b][\bar{l}(1-\gamma_5)\nu]) \tag{1.52}$$

where

$$R_l = \tan^2\beta(m_b m_l/m^2_{H^-}). \tag{1.53}$$

The pseudoscalar coupling of the $H^{\pm}$ boson is given by:

$$< 0|\bar{u}\gamma_5 b|B^- >= -if_B(m^2_B/m_b), \tag{1.54}$$

where we have ignored m_u compared to m_B. One easily arrives at the amplitude

$$\mathcal{B}_{(B\to l\nu)} = -\frac{G_F}{\sqrt{2}}V_{ub}f_B(m_l - R_l(m^2_B/m_b)) \times \bar{l}(1-\gamma_5)\nu, \tag{1.55}$$

where the SM term is propotional to m_l, while the charged Higgs term is propotional to R_l. Using equation 1.53, m_l can be factored out while the explicit quark mass dependence in m_b cancels, and we find:

$$\mathcal{B}_{(B\to\tau\nu)} = \mathcal{B}_{SM} \times \left(1 - \tan^2\beta\frac{m^2_{B^{\pm}}}{m^2_{H^{\pm}}}\right). \tag{1.56}$$

Comparing the measured value of the branching fraction and the Standard Model prediction, we can exclude regions in the $(m_{H^{\pm}}, \tan\beta)$ plane, as shown in fig. 1.7.

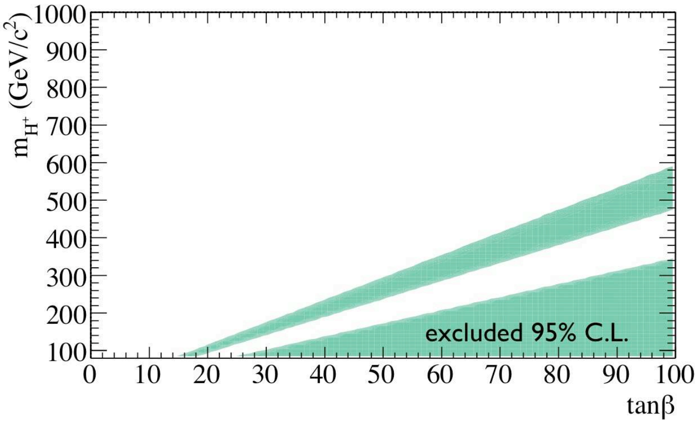

Figure 1.7: Exclusion plot of $(m_{H^\pm}, \tan\beta)$. The green regions are excluded at 95% C.L., while the lower limit on m_H is set by the LEP experiment at $97.3\,\mathrm{GeV}/c^2$ [21]

.

Chapter 2

BaBar Experiment at PEP-II

2.1 Introduction

The BaBar experiment takes place at the Stanford Linear Accelerator Center (SLAC). The acceleretor and the detector took data from October 1999 to April 2008. The primary goal of the BaBar experiment is the study of CP-violating asymmetries in the decay of neutral B meson. Secondary goals are precision measurement of decays of bottom and charm mesons and of τ leptons, and searches for rare processes accessible because of the high luminosity of PEP II B Factory.

The PEP-II B Factory is an e^+e^- asymmetric collider running at a center of mass energy of 10.58 GeV corresponding to the mass of the $\Upsilon(4S)$ resonance. The electron beam in the High Energy Ring (HER) has 9.0 GeV and the positron beam in the Low Energy Ring (LER) has 3.1 GeV. The $\Upsilon(4S)$ is therefore produced with a Lorentz boost of $\beta\gamma = 0.56$. This boost makes it possible to reconstruct the decay vertices of the two B mesons, to determine their relative decay times Δt, and thus to measure the time dependence of their decay rates, since, without boost, this distance would be too small ($\sim 30\ \mu$) to be measured by any vertex tracker.

The BaBar detector [22] has been optimized to reach the primary goal of the CP asymmetry measurement. This measurement needs the complete reconstruction of a B decay in a CP eigenstate, the flavour identification (tagging) of the non-CP B and a measure of the distance of the two decay vertices. To fulfill these needs, a very good vertex resolution, both transverse and parallel to the beam direction, excellent reconstruction efficiency for charged particles and a very good momentum resolution, efficient electron and muon identification, with low misidentification probabilities for hadrons, are required.

A longitudinal section of the BaBar detector is shown in Fig. 2.1.The detector innermost part is reserved for the silicon vertex tracker (SVT), then there is the drift chamber (DCH), the Cerenkovlight detector (DRC) and the CsI electromagnetic calorimeter (EMC). All those detector sub-systems are surrounded by a solenoidal superconductor magnetic field. The iron used for the return flux has been instrumented (IFR) for muons and neutral hadrons, like K_L and neutrons, detection.

The detector geometry is cylindrical in the inner zone and hexagonal in the outermost zone: the central part of the structure is called *barrel* and it's closed forward and backward by *end caps*. The covered polar angle ranges from 350 mrad, in the forward, to 400 mrad in the backward directions (defined with respect to the high energy beam

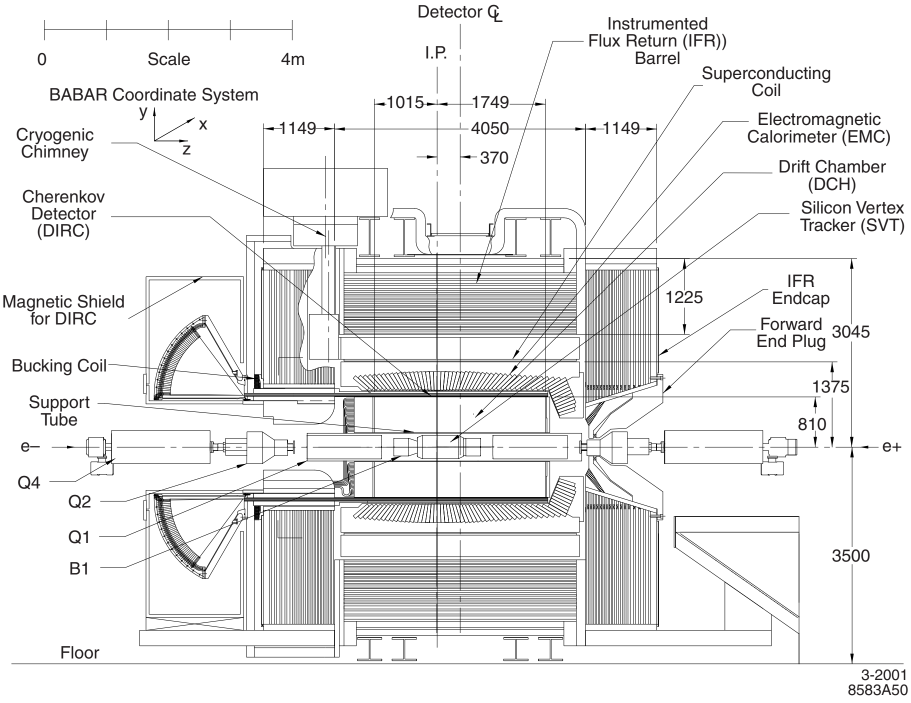

Figure 2.1: BABAR detector longitudinal section.

direction). The *BABAR* coordinate system has the z axis along the boost direction (or the beam direction): the y axis is vertical and the x axis is horizontal and goes toward the external part of the ring. In order to maximize the geometrical acceptance for $\Upsilon(4S)$ decays the whole detector is offset, with respect to the beam-beam interaction point (IP), by 0.37 m in the direction of the lower energy beam.

A trigger system is used to separate collisions producing interesting events from those that constitutes the noise, or the background, for instance, beam interactions with residual gas. The trigger system is divided in two consequent levels: the level one trigger ($L1$) is hardware based and is designed to have a maximum output rate of 2 kHz and a maximum time delay of 12 μs, while the other level ($L3$), software based, has a throughput rate limited to $120Hz$ in order to permit an easy storage and processing of collected data.

2.2 PEP-II B Factory

The clean experimental environment of an e^+e^- collider can be used to study the properties of B mesons by producing a large number of $\Upsilon(4S)$ mesons. The $\Upsilon(4S)$ whose mass is 10.58 GeV/c2, is the lightest bottomonium vector state which can decay to pairs of open beauty mesons: $B_u^+B_u^-$ and $B_d^0\bar{B}_d^0$ in roughly the same amount. Table 2.1 summarizes the cross sections for the various processes accessible by colliding two e^+e^- beams at the energy corresponding to the mass of the $\Upsilon(4S)$ in the center of mass (c.m.) reference frame [23]. Given that the mass of the $\Upsilon(4S)$ is slightly larger than twice the mass of a B meson, the BB pair is emitted with a momentum of

$e^+e^- \rightarrow$	Cross section (nb)
$b\bar{b}$	1.05
$c\bar{c}$	1.30
$s\bar{s}$	0.35
$u\bar{u}$	1.39
$d\bar{d}$	0.35
$\tau^+\tau^-$	0.94
$\mu^+\mu^-$	1.16
e^+e^-	~ 40

Table 2.1: Various processes cross sections at $\sqrt{s} = M_{\Upsilon(4S)}$. $Bhabha$ cross section is an effective cross section, within the experimental acceptance.

$\sim 335 MeV/c$ in the c.m. frame, and considering the lifetime of the B mesons being $\sim$ 1.5ps, the average distance of the two decay vertices would be roughly $60\mu m$. With the state of the art vertex detectors, this value is too small to allow time-dependent analyses of the $B^0 B^0$ system in a traditional symmetric e^+e^- collider. This motivated the proposal[24] for the construction of an asymmetric e^+e^- collider, where the B mesons are boosted in the laboratory frame, so that the average separation between the two B decay vertices is inflated to measurable values. The Conceptual Design Report for the construction of the PEP-II B-factory at the Stanford Linear Accelerator Center was submitted in 1993 [25] as a proposal of an upgrade of the existing PEP facility and first colliding beams were stored in 1999.

2.2.1 Design and machine parameters

At the PEP-II B-factory a 9.0 GeV electron beam collides head-on against a 3.1 GeV positron beam, resulting in a $\beta\gamma = 0.56$ boost of the c.m. frame with respect to the laboratory. The beams are stored in two different rings: the High Energy Rings (HER) for the electrons, while the Low Energy Ring (LER) for the positrons. The interaction region, placed inside the magnetic field of the BABAR solenoid, comprises a series of samarium-cobalt permanent magnets which separate the bunches along the horizontal plane outside the luminous region. The main machine parameters are collected in table 2.2; the design values are compared to the record running values reached in 2008 during the last year of data-taking. The design luminosity has been reached pretty quickly at the end of the first year of datataking and in the following few years the record values have superseded the design ones by a factor of four in terms of instan-

Parameters	Design	Ultimate(2008)
Energy HER/LER (GeV)	9.0/3.1	9.0/3.1
Current HER/LER (A)	0.75/2.15	1.875/2.900
Number of bunches	1658	1722
Luminosity (10^{33} $cm^{-2}s^{-1}$)	3.0	12.1
Daily average integrated luminosity (pb^{-1}/d)	135	840

Table 2.2: PEP-II beam parameters. Design and ultimate values are quoted.

taneous luminosity and a factor of seven for the integrated one. The instantaneous luminosity is monitored by the PEP-II operators by measuring the Bhabha scattering rates, while a more precise value is computed offline, by studying other QED processes (primarily e^+e^- and $\mu^+\mu^-$ production). The r.m.s. energy spreads for the LER and HER beams are 2.3 MeV and 5.5 MeV, while the systematic uncertainty in the absolute beam energies is of the order of 5-10 MeV. The beam directions, the position and size of the luminous region (which are critical in timedependent analyses) are continuously monitored on a run by run basis (a run is a data-taking period typically lasting one hour). These parameters are measured by using well reconstructed two-tracks events, like $e^+e^- \to e^+e-, \quad \mu^+\mu^-$. The uncertainties in the average beam position are of the order of a few μm in the transverse plane, and $\sim 100\mu m$ in the longitudinal direction. Variations of these parameters over two consecutive runs are typically of the same order of magnitude of their uncertainties.

2.2.2 Machine background

Several components contribute to the machine-related background [26]:

- Synchrotron Radiation in the proximity of the interaction region, caused by the bending of the beams in the proximity of the permanent magnets. Careful design of the interaction region has been studied in order to limit the effects of this source of background.

- Beam-Gas Scattering, caused by the interaction of the beams with residual gas in the beam pipe. Even though the quality of vacuum has superseded the expectations, this is the most severe source of radiation damage to the SVT and the dominant source of background for all the sub-systems, except the DIRC.

- Luminosity Background, caused by energy-degraded electrons produced in radiative Bhabha events which enter the BABAR detector causing electromagnetic showers. This source of background is directly proportional to the luminosity and is already the largest source of background for the DIRC.

Other sources of background include beam losses during injection, intense bursts of radiation caused by tiny dust particles which become trapped in the beams and non-Gaussian tails from beam-beam interactions. The last background sources are a concern especially for the radiation protection of the SVT.

2.2.3 Delivered luminosity

The data-taking operations begun in 1999 and ended in 2008. Figure 2.2 shows the progression of delivered luminosity; the data-taking has been subdivided into the following periods:

Run1 , which corresponds to data taken in the period: May 1999 through October 2000;

Run2 January 2001 through July 2002;

Run3 November 2002 through July 2003;

Run4 September 2003 through July 2004;

Run5 April 2005 through August 2006;

Run6 January 2007 through September 2007;

Run7 December 2007 through April 2008;

Run7 data scanned the $\Upsilon(3S)$ and $\Upsilon(2S)$ resonance, and have not been cosidered for this analysis. During the first years of PEP-II running, data-taking was held only with the beams in coasting mode, that is without injecting new bunches of electrons/positrons to compensate for the beam dispersions. Data-taking runs were interleaved by short periods during which the beam currents were restored to the desired values. Since the beginning of Run4, thanks to the improvements in the accelerator stability and the reduction in the injection backgrounds, data-taking can be conducted in trickle injection mode, that is injecting (with a frequency of a few Hz) fresh bunches to both the LER and the HER in order to keep the beam currents to a constant level. A system has been developed in order to skip the collisions (which are affected by a higher background level) of a bunch during its first orbits. Most of data are collected setting the c.m. collision energy to the mass of the $\Upsilon(4S)$ (we call them on-resonance data). In order to study the events which do not originate from the decay of a $\Upsilon(4S)$, the so called continuum events, about 10% of the data are collected lowering by 40 MeV the energy of the collisions, which is enough to avoid the production of the $\Upsilon(4S)$ (whose width is $\sim$ 20 MeV). It is particularly important to get a reliable estimate of the number of B mesons produced during a particular data-taking period. The procedure (called B counting), which computes this number compares the ratio of the number hadronic events over the number of $e^+e^- \to \mu^+\mu^-$ events produced in on-resonance and off-resonance data samples, assuming that the excess seen in the on-resonance is entirely due to $\Upsilon(4S)$ decays. The number of events passing the kinematical selection N_Υ is given by:

$$N_\Upsilon = N_{MH} N_{\mu\mu} \cdot R_{off} \cdot k \tag{2.1}$$

where N_{MH} is the number of events passing the selection in the on-resonance sample, $N_{\mu\mu}$ is the number of $\mu^+\mu^-$ events in the on-resonance sample, $R_{off} = N_{MH}^{off}/N_{\mu\mu}^{off}$ is the ratio of hadronic events to muon pairs in the off-resonance sample and k is a numerical factor close to 1, which accounts for the energy dependence of the $e^+e^- \to \mu^+\mu^-$ cross section and variations in the selection efficiencies. Monte Carlo simulations carefully validated on data are used to compute the selection efficiencies; the overall systematic error on the B counting procedure is estimated to be $\sim 1\%$.

2.3 Tracking system

The charged particle tracking system consists of two different components: the silicon vertex tracker (SVT) and the drift chamber (DCH): the main purpose of this tracking system is the efficient detection of charged particles and the measurement of their momentum and angles with high precision. These track measurements are important for the extrapolation to the DIRC, the EMC and the IFR: at lower momenta, the DCH measurements are more important while at higher momenta the SVT dominates.

2.3.1 The Silicon Vertex Tracker: SVT.

The vertex detector has a radius of $20\,cm$ from the primary interaction region: it is placed inside the support tube of the beam magnets and consists of five layers of

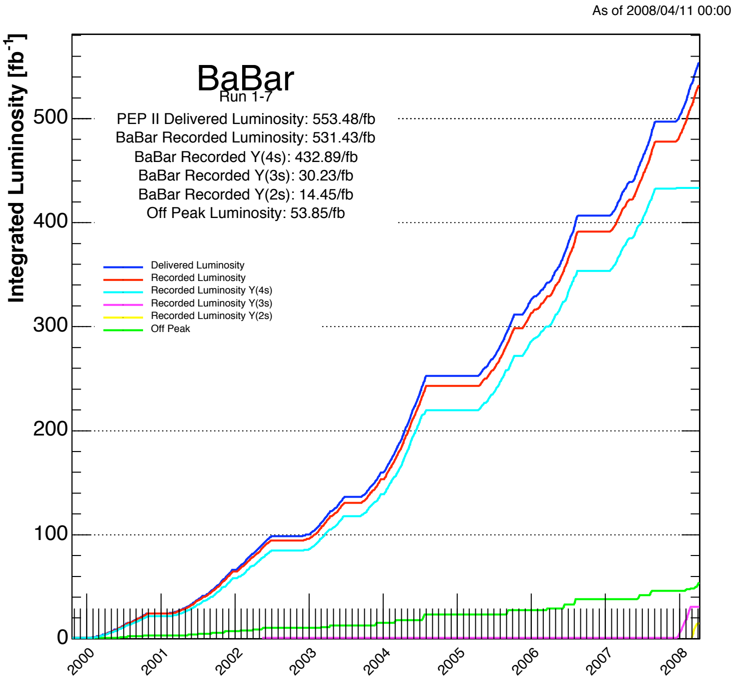

Figure 2.2: Integrated luminosity and obtained by PEP-II and collected by *BABAR* from 1999 to 2008.

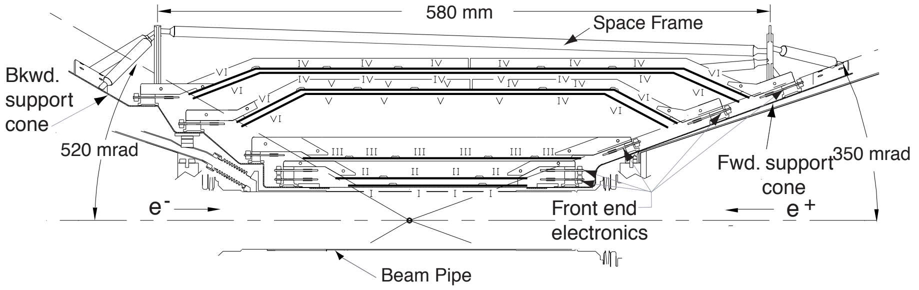

Figure 2.3: SVT schematic view: longitudinal section.

double-sided silicon strip sensors detectors to provide five measurements of the positions of all charged particles with polar angles in the region $20.1° < \theta < 150°$. Because of the presence of a $1.5\,T$ magnetic field, the charged particle tracks with transverse momenta lower than $\sim$ 100 MeV/c cannot reach the drift chamber active volume. So the SVT has to provide stand-alone tracking for particles with transverse momentum less than 120 MeV/c, the minimum that can be measured reliably in the DCH alone: this feature is essential for the identification of slow pions from D^*-meson decays. Because of these, the SVT has to provide redundant measurements.

Beyond the stand-alone tracking capability, the SVT provides the best measurement of track angles which is required to achieve design resolution for the Čerenkov angle for high momentum tracks. The SVT is very close to the production vertex in order to provide a very precise measure of points on the charged particles trajectories on both longitudinal (z) and transverse directions. The longitudinal coordinate information is necessary to measure the decay vertex distance, while the transverse information allows a better separation between secondary vertices coming from decay cascades.

More precisely, the design of the SVT was carried out according to some important guidelines:

- The number of impact points of a single charged particle has to be greater than 3 to make a stand-alone tracking possible, and to provide an independent momentum measure.

- The first three layers are placed as close as possible to the impact point to achieve the best resolution on the z position of the B meson decay vertices.

- The two outer layers are close to each other, but comparatively far from the inner layers, to allow a good measurement of the track angles.

- The SVT must withstand 2 MRad of ionizing radiation: the expected radiation dose is 1 Rad/day in the horizontal plane immediately outside the beam pipe and 0.1 Rad/day on average.

- Since the vertex detector is inaccessible during normal detector operations, it has to be reliable and robust.

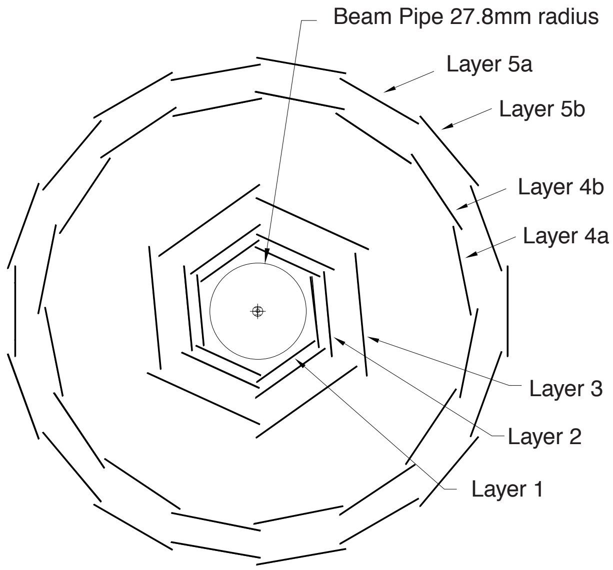

Figure 2.4: Cross-sectional view of the SVT in a plane perpendicular to the beam axis.

These guidelines have led to the choice of a SVT made of five layers of double-sided silicon strip sensors: the spatial resolution, for perpendicular tracks must be $10-15\,\mu m$ in the three inner layers and about $40\,\mu m$ in the two outer layers. The three inner layers perform the impact parameter measurement, while the outer layers are necessary for pattern recognition and low p_t tracking. The silicon detectors are double-sided (contain active strips on both sides) because this technology reduces the thickness of the materials the particles have to cross, thus reducing the energy loss and multiple scattering probability compared to single-sided detectors. The sensors are organized in modules (Fig. 2.3). The SVT five layers contain 340 silicon strip detectors with AC-coupled silicon strips.

Each detector is $300\,\mu m$-thick but sides range from $41\,mm$ to $71\,mm$ and there are 6 different detector types. Each of the three inner layers has a hexagonal transverse cross-section and it is made up of 6 detector modules, arrayed azimuthally around the beam pipe, while the outer two layers consist of 16 and 18 detector modules, respectively. The inner detector modules are barrel-style structures, while the outer detector modules employ the novel arch structure in which the detectors are electrically connected across an angle. This arch design was chosen to minimize the amount of silicon required to cover the solid angle while increasing the solid angle for particles near the edges of acceptance: having incidence angles on the detector closer to 90 degrees at small dip angles insures a better resolution on impact points. One of the main features of the SVT design is the mounting of the readout electronics entirely outside the active detector volume.

The strips on the two sides of the rectangular detectors in the barrel regions are oriented parallel (ϕ strips) or perpendicular (z strips) to the beam line: in other words, the inner sides of the detectors have strips oriented perpendicular to the beam direction to measure the z coordinate (z-size), whereas the outer sides, with longitudinal strips, allow the ϕ-coordinate measurement (ϕ-side). In the forward and backward regions of the two outer layers, the angle between the strips on the two sides of the trapezoidal detectors is approximately 90° and the ϕ strips are tapered.

The inner modules are tilted in ϕ by 5°, allowing an overlap region between adjacent modules: this provide full azimuthal coverage and is convenient for alignment. The outer modules are not tilted, but are divided into sub-layers and placed at slightly different radii (see Fig. 2.4).

The total silicon area in the SVT is $0.94\,m^2$ and the number of readout channels is about $150\,000$. The geometrical acceptance of SVT is 90% of the solid angle in the c.m. system and typically 80% are used in charged particle tracking.

The z-side strips are connected to the read-out electronics with flexible *Upilex* fanout circuits glued to the inner faces of half-modules: as a matter of fact, each module is divided into two electrically separated forward and backward half-modules. The fanout circuits consist of conductive traces on a thin flexible insulator (copper traces on Kapton): the traces are wire-bonded to the end of the strips.

In the two outer layers, in each module the number of z strips exceeds the number of read-out channels, so that a fraction of the strips is “ganged”, i.e., two strips are connected to the same read-out channel. The “ganging” is performed by the fanout circuits. The length of a z strip is about $50\,\mu m$ (case of no ganging) or $100\,\mu m$ (case of two strip connected): the ganging introduces an ambiguity on the z coordinate measurement, which must be resolved by the pattern recognition algorithms. The ϕ strips are daisy-chained between detectors, resulting in a total strip length of up to $26\,cm$. Also, for the ϕ-side, a short fanout extension is needed to connect the ends of the strips to the read-out electronics.

	1st layer	2nd layer	3rd layer	4th layer	5th layer
radius (mm)	32	40	54	91-127	114-144
modules/layer	6	6	6	16	18
wafers/module	4	4	6	7	8
read-out pitch (μm)					
ϕ	50-100	55-110	55-110	100	100
z	100	100	100	210	210

Table 2.3: Parameters of the SVT layout: these characteristics are shown for each layer.

The signals from the read-out strips are processed using a new technique, bringing in several advantages. After amplification and shaping, the signals are compared to a preset threshold and the time they exceed this threshold (time over threshold, or ToT) is measured. This time interval is related to the charge induced in the strip by the charged particle crossing it. Unlike the traditional peak-amplitude measurement in the shaper output, the ToT has the advantage of an approximately logarithmic relation of the time interval to the charge signal. This compresses the active dynamic range of the signal, ensuring a good sensitivity in the lower range. When a particle crosses a silicon detector a cluster of adjoining strips producing a signal is formed. The good signal resolution in the lower range ensures a good determination of the tails of the cluster thus improving the resolution on the impact point measurement.

The electronic noise measured is found to vary between 700 and 1500 electrons ENC (equivalent noise charge), depending on the layer and the readout view: this can be compared to the typical energy deposition for a minimum ionizing particle at normal incidence, which is equivalent to $\sim$ 24000 electrons.

During normal running conditions, the average occupancy of the SVT in a time window of $1\,\mu s$ is about 2% for the inner layers, where it is dominated by machine backgrounds, and less than 1% for the outer layers, where noise hits dominate.

The cluster reconstruction is based on a cluster finding algorithm: first the charge pulse height of a single pulse is calculated form the ToT value and clusters are formed grouping adjacent strips with consistent times. The position x of a cluster formed by n strips is evaluated with an algorithm called "head-to-tail" algorithm:

$$x = \frac{(x_1 + x_n)}{2} + \frac{p\,(Q_n - Q_1)}{2\,(Q_n + Q_1)}$$

where x_i and Q_i are the position and the collected charge of i-th strip and p is the read-out pitch. This formula always gives a cluster position within $p/2$ of the geometrical center of the cluster. The cluster pulse height is simply the sum of the strip charges, while the cluster time is the average of the signal times.

The SVT efficiency can be calculated for each half-module by comparing the number of associated hits to the number of tracks crossing the active area of the half-module. Excluding defective readout sections (9 over 208), the combined hardware and software efficiency is 97%.

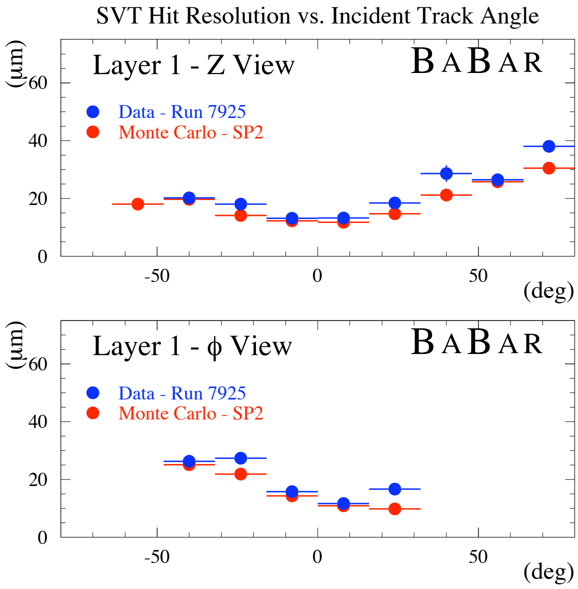

Figure 2.5: SVT hit resolution in the z and ϕ coordinate in microns, plotted as functions of the track incident angle in degrees.

The spatial resolution of SVT hits is calculated by measuring the distance (in the plane of the sensor) between the track trajectory and the hit, using high-momentum tracks in two prong events: the uncertainty due to the track trajectory is subtracted from the width of the residual distribution to obtain the hit resolution. The track hit residuals are defined as the distance between track and hit, projected onto the wafer plane and along either the ϕ or z direction. The width of this residual distribution is then the SVT hit resolution. Fig. 2.5 shows the SVT hit resolution for z and ϕ side hits as a function of the track incident angle: the measured resolutions are in very good agreement with the MonteCarlo expected ones. Over the whole SVT, resolutions are raging from $10-15\,\mu m$ (inner layers) to $30-40\,\mu m$ (outer layers) for normal tracks.

For low-momentum tracks ($p_t < 120$ MeV/c), the SVT provides the only particle identification information. The measure of the ToT value enables to obtain the pulse height and hence the ionization dE/dx: the value of ToT are converted to pulse height using a look-up table computed from the pulse shapes. The double-sided sensors provide up to ten measurements of dE/dx per track: with signals from at least four sensors, a 60% truncated mean dE/dx is calculated. For MIPs, the resolution on the truncated mean dE/dx is approximately 14%: a 2σ separation between kaons and pions can be achieved up to momentum of 500 MeV/c and between kaons and protons beyond 1 GeV/c.

2.3.2 The drift chamber: DCH.

The drift chamber is the second part of BABAR tracking system: its principal purpose is the efficient detection of charged particles and the measurement of their momenta and angles with high precision. The DCH complements the measurements of the impact parameter and the directions of charged tracks provided by the SVT near the impact point (IP). At lower momenta, the DCH measurements dominate the errors on the extrapolation of charged tracks to the DIRC, EMC and IFR. The reconstruction of decay and interaction vertices outside of the SVT volume, for instance the K^0_S decays, relies only on the DCH. For these reasons, the chamber should provide maximal solid angle coverage, good measurement of the transverse momenta and positions but also of the longitudinal positions of tracks with a resolution of $\sim 1\,mm$, efficient reconstruction of tracks at momenta as low as 100 MeV/c and it has to minimally degrade the performance of the calorimeter and particle identification devices (the most external detectors). The DCH also needs to supply information for the charged particle trigger. For low momentum particles, the DCH is required to provide particle identification by measuring the ionization loss (dE/dx). A resolution of about 7% allows π/K separation up to 700 MeV/c. This particle identification (PID) measurement is complementary to that of the DIRC in the barrel region, while in the extreme backward and forward region, the DCH is the only device providing some discrimination of particles of different mass. The DCH should also be able to operate in presence of large beam-generated backgrounds having expected rates of about $5\,kHz$/cell in the innermost layers.

To meet the above requirements, the DCH is a $280\,cm$-long cylinder (see left plot in Fig. 2.6), with an inner radius of $23.6\,cm$ and an outer radius of $80.9\,cm$: it is bounded by the support tube at its inner radius and the particle identification device at its outer radius. The flat end-plates are made of aluminum: since the BABAR events will be boosted in the forward direction, the design of the detector is optimized to reduce the material in the forward end. The forward end-plate is made thinner ($12\,mm$) in the acceptance region of the detector compared to the rear end-plate ($24\,mm$), and all the electronics is mounted on the rear end-plate. The device is asymmetrically located with respect to the IP: the forward length of 174.9 cm is chosen so that particles emitted at polar angles of 17.2° traverse at least half of the layers of the chamber before exiting through the front end-plate. In the backward direction, the length of 101.5 cm means that particles with polar angles down to 152.6° traverse at least half of the layers.

The inner cylinder is made of $1\,mm$ beryllium and the outer cylinder consists of

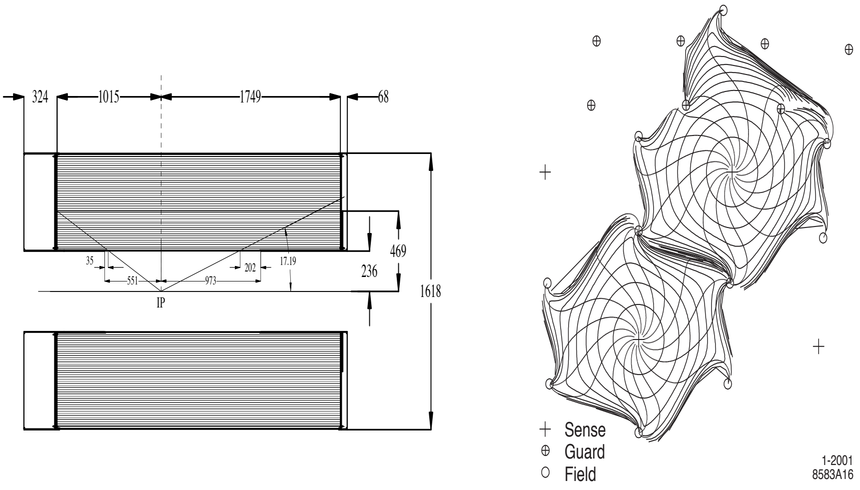

Figure 2.6: Side view of the *BABAR* drift chamber (the dimensions are in mm) and isochrones (i.e. contours of equal drift time of ions) in cells of layer 3 and 4 of an axial super-layer. The isochrones are spaced by $100\,ns$.

two layers of carbon fiber glued on a Nomex core: the inner cylindrical wall is kept thin to facilitate the matching of SVT and DCH tracks, to improve the track resolution for high momentum tracks and to minimize the background from photon conversions and interactions. Material in the outer wall and in the forward direction is also minimized in order not to degrade the performance of the DIRC and the EMC.

The region between the two cylinders is filled up by a gas mixture consisting of Helium-isobutane (80% : 20%): the chosen mixture has a radiation length that is five times larger than commonly used argon-based gases. 40 layers of wires fill the DCH volume and form 7104 hexagonal cells with typical dimensions of $1.2 \times 1.9\,cm^2$ along the radial and azimuthal directions, respectively (see right plot in Fig. 2.6). The hexagonal cell configuration has been chosen because approximate circular symmetry can be achieved over a large portion of the cell. Each cell consist of one sense wire surrounded by six field wires: the sense wires are $20\,\mu m$ gold-plated tungsten-rhenium, the field wires are $120\,\mu m$ and $80\,\mu m$ gold-plated aluminum. By using the low-mass aluminum field wires and the helium-based gas mixture, the multiple scattering inside the DCH is reduced to a minimum, representing less than $0.2\% X_0$ of material. The total thickness of the DCH at normal incidence is $1.08\% X_0$.

The drift cells are arranged in 10 super-layers of 4 cylindrical layers each: the super-layers contain wires oriented in the same direction: to measure the z coordinate, axial wire super-layers and super-layers with slightly rotated wires (*stereo*) are alternated. In the stereo super-layers a single wire corresponds to different ϕ angles and the z coordinate is determined by comparing the ϕ measurements from axial wires and the measurements from rotated wires. The stereo angles vary between ± 45 mrad and ± 76 mrad.

While the field wires are at ground potential, a positive high voltage is applied to the sense wires: an avalanche gain of approximately 5×10^4 is obtained at a typical operating voltage of $1960\,V$ and a $80\!:\!20$ helium:isobutane gas mixture.

In each cell, the track reconstruction is obtained by the electron time of flight: the precise relation between the measured drift time and drift distance is determined from sample of e^+e^- and $\mu^+\mu^-$ events. For each signal, the drift distance is estimated by computing the distance of closest approach between the track and the wire. To avoid bias, the fit does not include the hit of the wire under consideration. The estimated drift distances and the measured drift times are averaged over all wires in a layer.

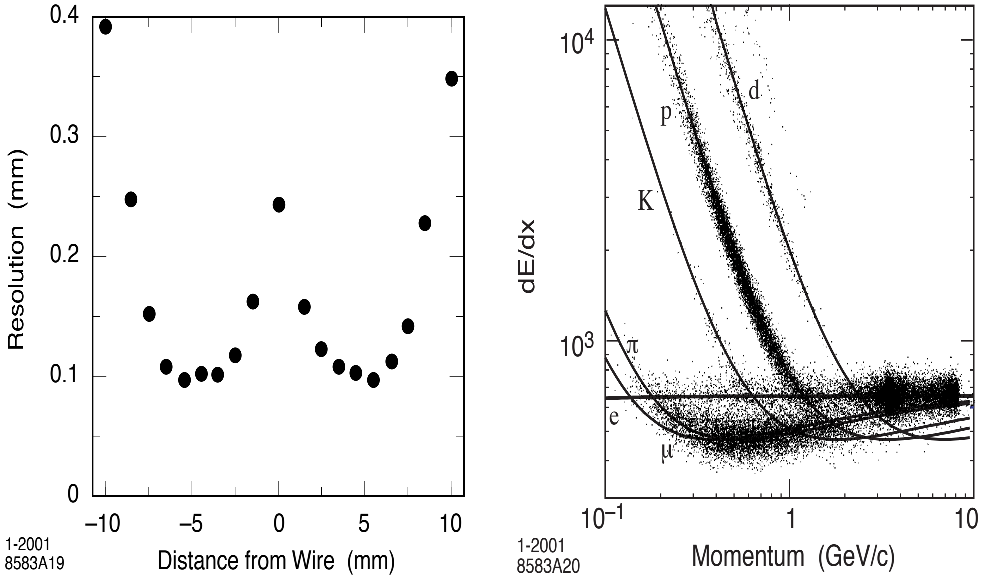

Figure 2.7: Left plot: *DCH* position resolution as a function of the drift chamber in layer 18, for tracks on the left and right side of the sense wire. The data are averaged over all cells in the layer. Right plot: measurement of dE/dx in the *DCH* as a function of the track momenta. The data include large samples of beam background triggers as evident from the high rate of protons. The curves show the Bethe-Bloch predictions derived from selected control samples of particles of different masses.

The *DCH* expected position resolution is lower than $100\,\mu m$ in the transverse plane, while it is about $1\,mm$ in the z direction. The minimum reconstruction and momentum measure threshold is about 100 MeV$/c$ and it is limited by the *DCH* inner radius. The design resolution on the single hit is about $140\,\mu m$ while the achieved weighted average resolution is about $125\,\mu m$. Left plot in Fig. 2.7 shows the position resolution as a function of the drift distance, separately for the left and the right side of the sense wire. The resolution is taken from Gaussian fits to the distributions of residuals obtained from unbiased track fits: the results are based on multi-hadron events for data averaged over all cells in layer 18.

The specific energy loss (dE/dx) for charged particles through the *DCH* is derived from the measurement of the total charge collected in each drift cell: the specific energy loss per track is computed as a truncated mean from the lowest 80% of the individual dE/dx measurements. Various corrections are applied to remove sources of bias: these corrections include changes in gas pressure and temperature ($\pm 9\%$ in dE/dx), differences in cell geometry and charge collection ($\pm 8\%$), signal saturation due to space charge buildup ($\pm 11\%$), non-linearities in the most probable energy loss at large dip angles ($\pm 2.5\%$) and variation of cell charge collection as a function of the entrance angle ($\pm 2.5\%$).

Right plot in Fig. 2.7 shows the distribution of the corrected dE/dx measurements as a function of track momenta: the superimposed Bethe-Bloch predictions have been determined from selected control samples of particles of different masses. The achieved dE/dx rms resolution for Bhabha events is typically 7.5%, limited by the number of samples and Landau fluctuations, and it is close to the expected resolution of 7%.

2.4 Cerenkovlight detector: *DIRC*

The need of a high efficiency in B flavor-tagging using charged kaons and the study of CP asymmetries in channels as $B^0 \to \pi^+\pi^-, \quad K^+\pi^-$ motivated the development of a high performance device, capable of performing clean K/pi separation in the momentum range $0.7 - 4.2\,\mathrm{GeV}/c$, The choice of the BaBar collaboration has been a newly developed ring-imaging Cerenkov detector, called the DIRC [27]. This device should be thin and uniform in order not to degrade the performance of the electromagnetic calorimeter and not to inflate its cost. Particle identification of a charged particle is achieved by combining the measurement of its Cerenkov angle θ_c performed by the DIRC with its momentum. Cerenkov photons are produced by the passage of the particle through 17 mm thick, 35 mm wide and 4.9m long fused synthetic silica bars, which have an index of refraction $n = 1.473$. The principle exploited by the DIRC is the fact that the magnitude of the angles of Cerenkov light are preserved during multiple reflections from flat surfaces. The quartz bars serve both as radiators and as light pipes to convey the photons into the standoff box, a water filled tank instrumented with 10752 photomultipliers, where the light is collected. The 144 bars are arranged in 12 sections, each one made up of a hermetically sealed bar box containing 12 quartz bars each. The non-instrumented (forward) end of the bars is terminated with a mirror, while the interface between quartz bars and water is provided by a fused silica wedge. The total radial thickness of DIRC radiators is 80 mm, corresponding to $17\% X_0$ at normal incidence; the solid angle subtended by the radiation bars corresponds to 94% of the azimuthal angle and 83% of the c.m. polar angle cosine. Given the geometrical and optical properties of the system, the overall angular resolution on a single photon corresponds to 10 mrad. The choice of the material for the radiator bars is due to the excellent properties of fused silica in terms of resistance to ionizing radiation, index of refraction, attenuation length, low chromatic dispersion and the possibility to get very accurate optical finish of surfaces (which is crucial to preserve the original information on θ). Figure 2.8 shows a schematic picture of the DIRC and its principle. The Cerenkov light pattern expected at the standoff box is a conic section; besides the position of the associated hits, also the timing is measured in order to get rid of potential ambiguities and reduce the background, as can be seen from figure 2.9. Background originate mostly from low energy photons coming from the PEP-II rings hitting the standoff box and is also reduced by lead shielding around the beam line. The calibration procedure involves two steps. The first one is performed online by means of a light pulser system which generates 1 ns duration light pulses to determine the mean time delay of each photomultiplier. The global time delay is determined at the second step, where real data tracks are used to fit Δt_γ, that is the difference between the uncalibrated time minus the expected arrival time of a Cerenkov photon. Figure 2.10 shows the K/π which is achievable using the DIRC alone.

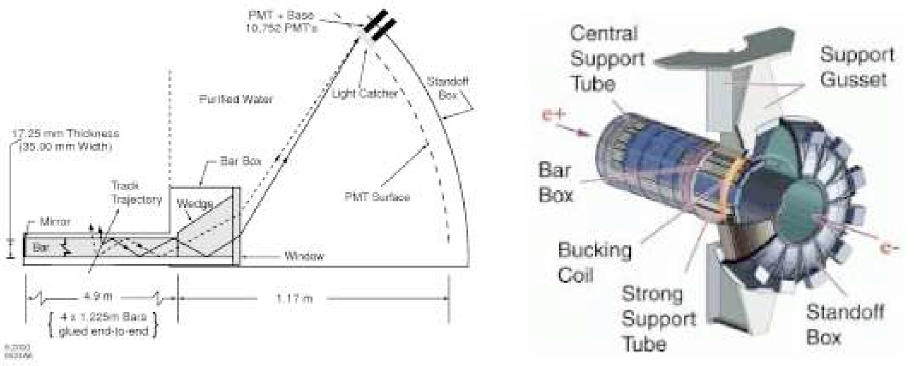

Figure 2.8: Scheme of a radiator bar (left picture) and exploded view of the DIRC.

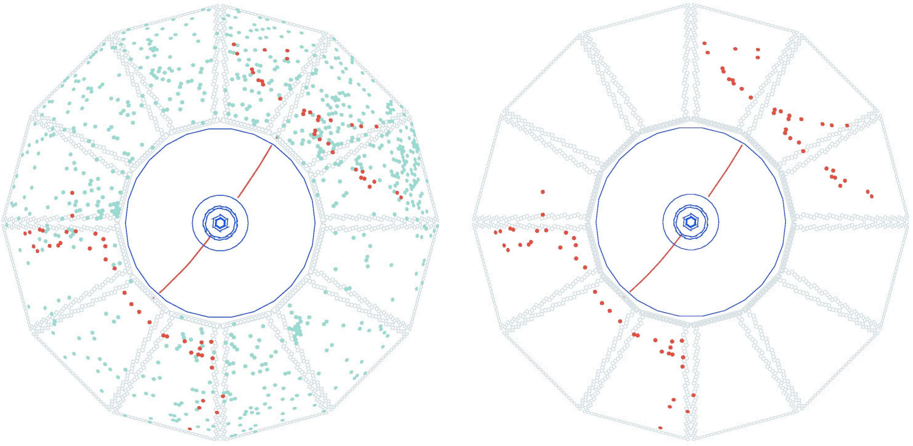

Figure 2.9: DIRC light pattern from a typical two-tracks event. On the left plot, all hits within th ±300 ns trigger window are shown, whileon the right only the signal within 8 ns of the expected photon arrival time are shown. The background reduction factor is of the order of 40.

More on its performance will be shown in section 2.7.

2.5 Electromagnetic calorimeter: *EMC*

The electromagnetic calorimeter (EMC) is designed to measure electromagnetic showers with excellent efficiency and energy and angular resolutions over the energy range from 20 MeV to 9 GeV. Figure 2.11 shows the layout of the EMC. It is constituted by two sections: a cylindrical barrel, containing 5760 crystals disposed in 48 rings, and a conical endcap, carrying 820 crystals, arranged in 8 rings. The material chosen for the crystals is the tallium-doped CsI, whose properties match the desired energy and angular resolution. Depending on the position, the crystal are 29.6 cm to 32.4 cm long and

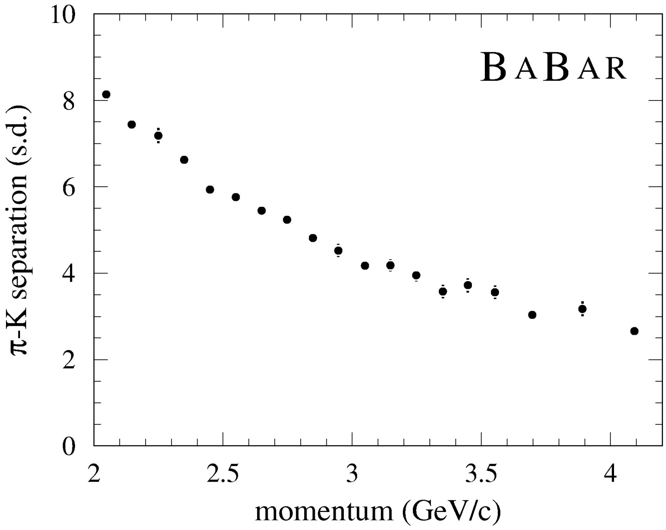

Figure 2.10: Number os standard deviations achievable in K/π separation with the DIRC as a function of the particle momentum.

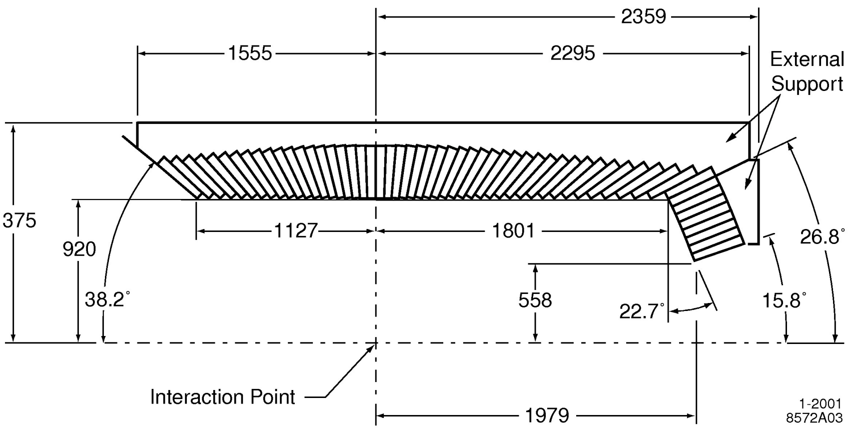

Figure 2.11: Longitudinal cross section of the EMC, showing the 56 crystal rings. The detector is axially symmetric around the z axis. All dimension are expressed in mm.

they have trapezoidal shape, with the front face having an area of $4.7 \times 4.7\text{cm}^2$ and the back face $6.1 \times 6.0\text{cm}^2$. The material in front of the calorimeter is $0.3 - 0.6X_0$ thick, for the barrel and the five outer rings of the endcap, while for the innermost rings of the endcap it reaches $3X_0$, mainly due to the SVT support structure and electronics and the permanent magnets. Each crystal is read by a $2 \times 1\text{cm}^2$ silicon PIN diode glued on the back face, connected to a low-noise preamplifier. Light pulses used for calibration issues are brought to each crystal through two optical fibers attached to the back face. Due to calibration stability and the need to avoid mechanical stress on the PIN diodes joints, it is crucial that the crystals be maintained at an accurately monitored constant temperature. This is achieved by two separated cooling systems for the barrel and the endcap sections of the calorimeter. The energy resolution, measured in a wide energy range through different physical processes (Bhabha scattering, $\chi_{c1} \to J/\psi\gamma$, photons from π^0 and η decays) is determined to be (see figure 2.12):

$$\frac{\sigma_E}{E} = \frac{(2.32 \pm 0.30)\%}{E^{1/4}(\,\mathrm{GeV}^{1/4})} \oplus (1.85 \pm 0.12)\%, \tag{2.2}$$

while the angular resolution, determined using π^0 and η decays to pair of photons with roughly equal energies, is:

$$\sigma_\theta = \sigma_\phi = \left(\frac{3.87 \pm 0.07)}{\sqrt{E(\,\mathrm{GeV})}} \pm 0.04 \right) \mathrm{mrad}. \tag{2.3}$$

Concerning the energy calibration of the EMC, it happens in two steps. First, the measured pulse height on each crystal has to be translated to the actual energy deposited. Second, the energy deposited in a shower spreading over several adjacent crystals has to be related to the energy of the incident particle by correcting for energy losses. The calibration of the single crystals is performed at two energies at the opposite ends of the spectrum. The calibration at low energy uses a $6.13\,\mathrm{MeV}$ radioactive photon source provided by a low-energy neutron generator activating the cooling liquid which circulates on through the EMC. At high energies, Bhabha scattering events are used to constrain the deposited energy to the value predicted by a GEANT-based simulation of the detector. These two types of calibration are performed monthly. As for the cluster energy correction, it is computed as a function of the incident energy and polar angle. At low energy it is performed by using π^0 decays in a mass constrained fit, while at higher energies, radiative Bhabha scattering events are utilized.

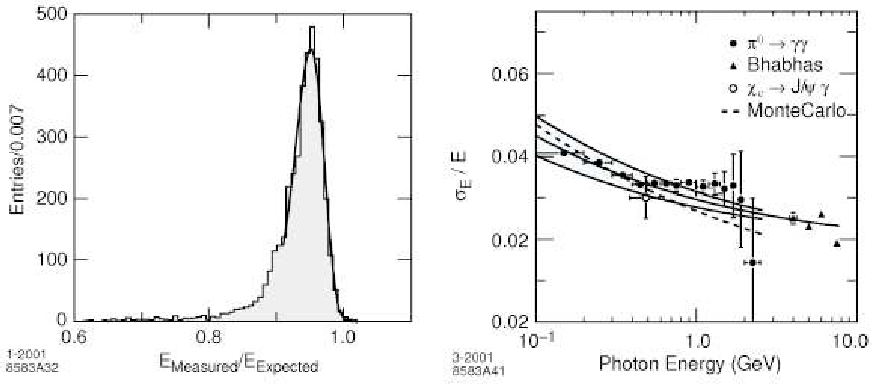

Figure 2.12: Performance of the EMC. Left: ratio of the measured energy to the expected one for Bhabha electrons of $7.5\,\mathrm{GeV}/c$. Right: the energy resolution for the EMC for electrons and photons from various physical processes. The solid line represents the fit result of equation 2.2, while the shaded area displays the rms error associated to the fit.

2.6 Instrumented Flux Return: IFR

IFR ($Instrumented\ Flux\ Return$) detector is dedicated to muon identification and neutral hadrons detection (mainly K_L^0) in a wide range of momentum and angles.

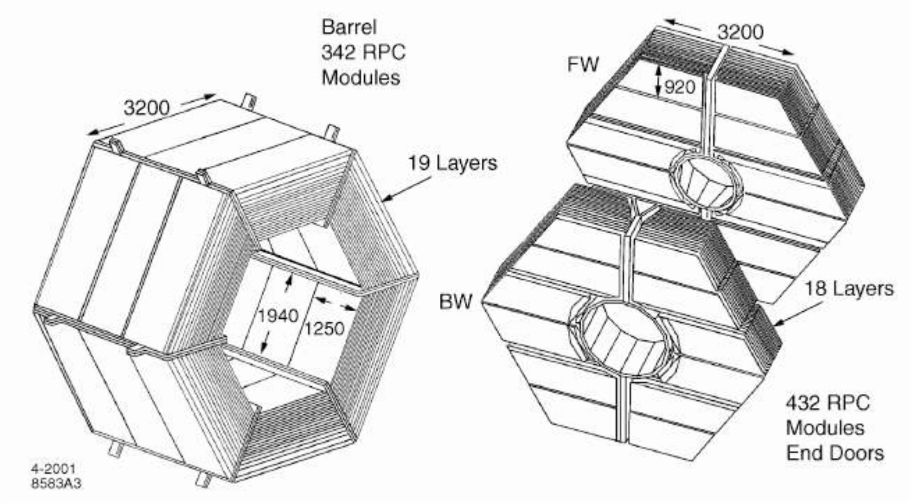

Figure 2.13: IFR view

The IFR, as all the other *BABAR* subsystems, has an asymmetric structure with a polar angle coverage that is $17° \leq \theta_{lab} \leq 150°$. The IFR (Fig. 2.13) is made of 19 layers of Resistive Plate Chambers (RPC) in the barrel region and 18 layers in forward and backward regions, that are placed inside the iron layers used for the solenoidal magnetic field return joke. The iron structure is subdivided in three main parts: the barrel one surrounding the solenoid, made of 6 sextants covering the radial distance between $1.820\ m$ and $3.045\ m$ with a length of $3.750\ m$ (along the z axis); the forward end-cap and backward end-cap covering the forward (positive z axis) and backward regions. Moreover, two cylindrical RPC layers have been installed between the calorimeter and the magnet cryostat in order to reveal particles exiting from the EMC. Those layers should cover the ϕ regions not covered by the barrel. Cylindrical layers are subdivided in four sections, each of them covering one fourth of the circumference: each of them has four RPC groups with orthogonal readout strips. $u - v$ helicoidal strips are placed inside along module's diagonals while ϕ and z parallel strips are placed outside. The summary of IFR readout segmentation is given in Tab. 2.4.

Each end-cap has an hexagonal shape and is vertically subdivided in two halves in order to allow internal subsystems access, if necessary: vacuum tube and PEP-II focusing elements are placed in the middle. Iron plates have a thickness ranging from 2 cm, for the inner ones placed nearest to the interaction region, to 10 cm for the outer ones; this means a total tickness of steel at normal incidence of $\sim$ 65 cm (nearly corresponding to $\sim$ 4 interaction lengths) in the barrel and $\sim$ 60 cm in the end-caps. Nominal distance between iron layers in the inner barrel region is 3.5 cm while is 3.2 cm everywhere else. The increased granularity of inner layers with respect to the outer ones is due to the fact that the largest part of particles detected inside the IFR are in-

section	# di sectors	coor.	readout # layer	# strip layer/sector	strip len. (cm)	strip larg. (mm)	total # channel
barrel	6	ϕ	19	96	350	19.7-32.8	$\approx$ 11k
		z	19	96	190-318	38.5	$\approx$ 11k
end-cap	4	y	18	6x32	124-262	28.3	13,824
		x	18	3x64	10-180	38.0	$\approx$ 15k
cyl.	4	ϕ	1	128	370	16.0	512
		z	1	128	211	29.0	512
		u	1	128	10-422	29.0	512
		v	1	128	10-423	29.0	512

Table 2.4: IFR readout segmentation. Total number of channels is $\sim$ 53k.

teracting in the very first material layers. Chosen segmentation is also the result of a compromise between the subsystem cost (proportional to the volume) and the need of a good efficiency for low momentum ($>$ 700 MeV) muon detection, minimizing, at the same time, fraction of K^0_L's that are not interacting inside the IFR. Result of this optimization is a not uniform segmentation with iron plates that have thickness increasing with distance from beam line. RPC section is shown in Fig. 2.14.

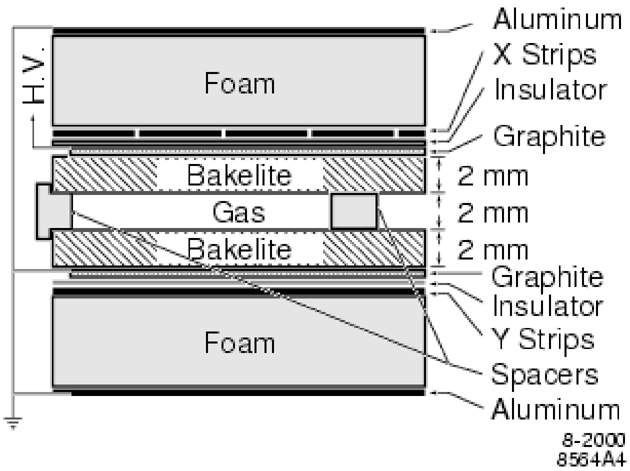

Figure 2.14: Planar RPC section with HV connection scheme.

In each barrel sextant layers are kept together by a structure that reduces the coverage of solid angle with active detectors of $\sim$ 7%. Active coverage of IFR detector is $\approx$ 2000 m^2, for a total RPC modules number that is $\sim$ 900. Signals produced by particles crossing the gas gap inside the RPCs are collected on both sides of the chamber by using thin strips (thickness $\sim$ 40 μm) with witdh of the order of a centimeter. Strips are applied in two orthogonal directions on insulating planes 200 μm thick, in order to have a bi-dimensional view. In each barrel sextant each gap is hosting a chamber. This consist of a set of 3 RPC modules of rectangular shape. Each module is $\sim$ 125 cm long along beams direction with variable width in order to completely fill the gap. Each chamber is equipped with 96 $\phi - strip$ placed along z axis that are measuring the ϕ angle inside the barrel and 96 $z - strip$ orthogonal to beams direction that are measuring z coordinate. $z - strips$ are subdivided into 3 panels of 32 strips with largeness, function of chamber radial position, ranging between 1.78 and 3.37 cm. This projective geometry allows a constant number of strips for all the various layers without decreasing detector resolution (each strip covers the same azimuthal angle). The used gas mixture is made of 56.7% Argon, 38.8% Freon-134a and 4.5% Isobutane. Working voltage for RPCs is $\sim 7.5\ kV$. Iron layers keeping apart RPC planes are chilled by a water system that keeps the temperature $\sim 20^oC$. RPC efficiencies have been measured by using cosmics taken on a weekly base.

2.6.1 IFR upgrade

Mean efficiency during 2000 run has been $\sim 78\%$ for the barrel and $\sim 87\%$ for the forward end-cap, less than that one measured in June 1999 ($\sim 92\%$). During the Summer 1999 the ambient temperature increased very much reaching about 32° to 38° inside the iron. During such period the IFR had problems to run the full detector because the dark current drawn by the chambers exceeded the total current limit provided by the power supply. All the chambers drawing more than $200\,\mu$A were disconnected. In October the chambers were re-connected but they didn't recover the full efficiency. The forward end-cap has been completely reconstructed and installed in the Summer 2002: 5 intermediate RPC layers were replaced by 2.54 cm of brass, 10 cm of steel were added after the last RPC layer, an RPC(layer 19) was added in front of the forward end-cap, an RPC belt was added in the barrel–end-cap overlap region. The accurate quality control on the new production and the close monitoring of the running conditions allowed the new generation of detectors to survive till the end of the runs with an overall good efficiency ($\sim 90\%$) and smooth data-taking. During Run5 and Run6, the operating mode of the inner middle chambers of the forward endcap has been switched from streamer to avalanche mode. This change was motivated by the fact that those chambers are heavily subject to beam-induced backgrounds, which causes higher rates, lower efficiencies and faster aging of the detectors. The gas mixture for avalanche running is typically: 22% Argon, 73% Freon and 5% isobutane and the high voltage is set to $\sim 9500V$, compared to $\sim 6700V$ for the new generation RPC's in streamer mode. The first experience of avalanche running showed a significant decrease of the charge produced by ionizing particles (thus a slower aging) and a recovery of the efficiency in the regions close to the beam line. For these reasons the forward endcap middle chambers of the seven innermost layers will continue running in avalanche mode till the end of data-taking. On the other side, the original cylindrical chambers have been switched off at the beginning of Run6, since their efficiencies dropped to insufficient values; they have been not replaced. A different strategy has been undertaken for recovering the efficiency in the barrel, adopting a different kind of detectors to replace the RPC's: the Limited Streamer Tubes (LST) [28]. Figure 2.15 shows a picture of a LST actually installed in BABAR . LST's are made from PVC extrusion having either 7 or 8 17×17mm^2 cells and covering the length of the barrel along the z axis. PVC surfaces are treated with a graphite paint, with a resistivity in the range 0.2 to 1.0 $M\Omega/$cm^2. A 100 μm diameter silver wire is strung along the z axis at the center of each cell and is sustained at intervals of 50 cm by plastic holders. The wires are kept at $\sim 5600V$, where the plateau conditions are met with the gas mixture being used: 89% CO_2, 8% Isobutane and 3% Argon. Signals are read directly on the wires for the φ coordinate, while the z coordinate is read through cathode strips glued outside the modules. The detection efficiency is close to the limit of 95% set by the presence of dead material on each layer of LST's. The capability of separating muons from charged hadrons has been improved by adding 4 brass layers.

Figure 2.15: Picture of a LST installed in the barrel of BABAR

The first two sextants of LST's have been installed during the shutdown between Run4 and Run5, and the remaining four between Run5 and Run6. The first experience of running of the LST's showed a completely restored efficiency of the barrel and no hints of degradations of its performance manifested.

2.7 Data taking and performances

2.7.1 Trigger

The basic requirement for the trigger system is the selection of events of interest with a high, stable and well-understood efficiency while rejecting background events and keeping the total event rate to manageable levels. The total trigger efficiency was required to exceed 99% for all BB events and at least 95% for continuum qq events. Less stringent requirements apply to other type of events, e.g. $\tau^+\tau$ events should have a $90-95\%$ trigger efficiency, depending on the specific $\tau^{\pm}$ decay channel. The trigger is implemented as a two-level hierarchy, the Level 1 (L1) in hardware followed by the Level 3 (L3) in software (a Level 2 trigger could have been developed in case L1 and L3 alone had not matched the requirements).
During normal operation at current luminosities, the L1 is configured to have an output rate of typically 1 kHz. Triggers are produced within a fixed latency window of 11-12 μs after the e^+e^- collision and delivered to the Fast Control and Timing System (FCTS). Data used to form the trigger decision are preserved with each event for efficiency studies. The L3 receives the output from L1, performs a second stage rate reduction for the main physics sources, and identifies and flags the special categories of events needed for luminosity determination, diagnostic and calibration purposes. The typical L3 output rate is 250 Hz.
The L1 trigger decision is based on charged tracks in the DCH above a preset transverse momentum, showers in the EMC, and tracks detected in the IFR. Trigger data are processed by three specialized hardware processors. The drift chamber trigger (DCT)

and electromagnetic calorimeter trigger (EMT) both satisfy all trigger requirements independently with high efficiency, and thereby provide a high degree of redundancy, which enables the measurement of trigger efficiency. The instrumented flux return trigger (IFT) is used for triggering $\mu^+\mu^-$ and cosmic rays, mostly for diagnostic purposes. The L3 trigger software comprises event reconstruction and classifications, a set of event selection filters, and monitoring. This software runs on the online computer farms within the Online Event Processing (OPE) framework. Many events which pass L1 but must be rejected by L3 are beam-induced charged particle background that are produced in material close to the IP. The Level 3 trigger combines DCT tracks and EMT clusters with the full DCH and EMC information. The L3 DCH algorithm performs fast pattern recognition and fits L1 tracks to helices and is able to determine the z coordinate of closest approach of tracks, which is important for rejecting the above mentioned background. The L3 EMC based trigger identifies energy clusters with a higher sensitivity than L1 and filters events with either high energy deposits of high cluster multiplicity. The output of both the DCH and EMC L3 filters is dominated by Bhabha events which are mostly rejected, but also prescaled in L3 for calibration and luminosity online monitoring and offline measurements.

2.7.2 Tracking

As already said, the *BABAR* tracking system is based on *SVT* and *DCH* detectors: charged particle tracking has been studied with large samples of cosmic ray muons, e^+e^-, $\mu^+\mu^-$ and $\tau^+\tau^-$ events, as well as multi-hadrons.

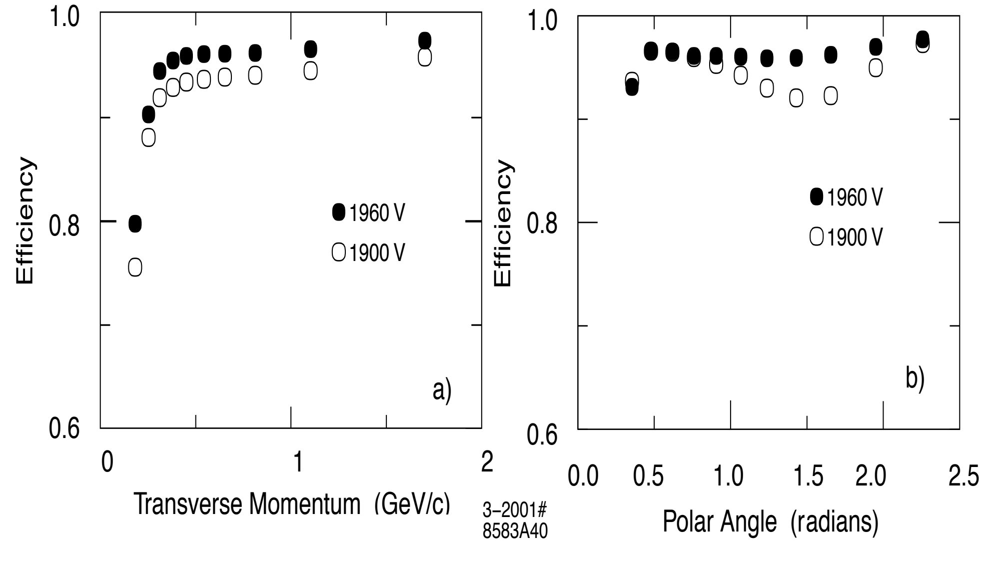

Figure 2.16: Track reconstruction efficiency in the *DCH* at operating voltages of $1960\,V$ and $1900\,V$ as a function of transverse momentum (left plot) and of polar angle (right plot). The efficiency is measured in multi-hadron events.

Charged tracks are defined by five parameters (d_0, ϕ_0, ω, z_0 and $\tan\lambda$) and their associated error matrix: these parameters are measured at the point of closest approach to the z-axis and d_0 and z_0 are the distances of this point from the origin of the coordinate system (in the $x - y$ plane and on the z axix, respectively). The angle ϕ_0 is the azimuth of the track, λ is the dip angle relative to the transverse plane and ω is the curvature. d_0 and ω have signs that depend on the particle charge.

The track finding and the fitting procedure make use of the Kalman filter algorithm that takes into account the detailed description of material in the detector and the full map of the magnetic field. First of all, tracks are reconstructed with *DCH* hits through a stand-alone *DCH* algorithm: the resulting tracks are then extrapolated into the *SVT* and *SVT* track segments are added and a Kalman fit is performed to the full set of *DCH* and *SVT* hits. Any remaining *SVT* hits are then passed to the *SVT* stand-alone track finding algorithms. Finally, an attempt is made to combine tracks that are only found by one of the two tracking systems and thus recover tracks scattered in the material of the support tube.

The efficiency for track reconstruction in the *DCH* has been measured as a function of transverse momentum, polar and azimuthal angles in multi-track events. These measurement rely on specific final states and exploit the fact that the track reconstruction can be performed independently in the *SVT* and the *DCH*. The absolute *DCH* tracking efficiency is determined as the ratio of the number of reconstructed *DCH* tracks to the number of tracks detected in the *SVT* with the requirement that they fall within the acceptance of the *DCH*. Left plot in Fig. 2.16 shows the efficiency in the *DCH* as a function of transverse momentum in multi-hadron events.

At design voltage of $1960\,V$, the efficiency averages $98 \pm 1\%$ per track above 200 MeV$/c$: the data recorded at $1900\,V$ show a reduction in efficiency by about 5% for tracks almost at normal incidence, indicating that the cells are not fully efficient at this voltage (see right plot in Fig. 2.16).

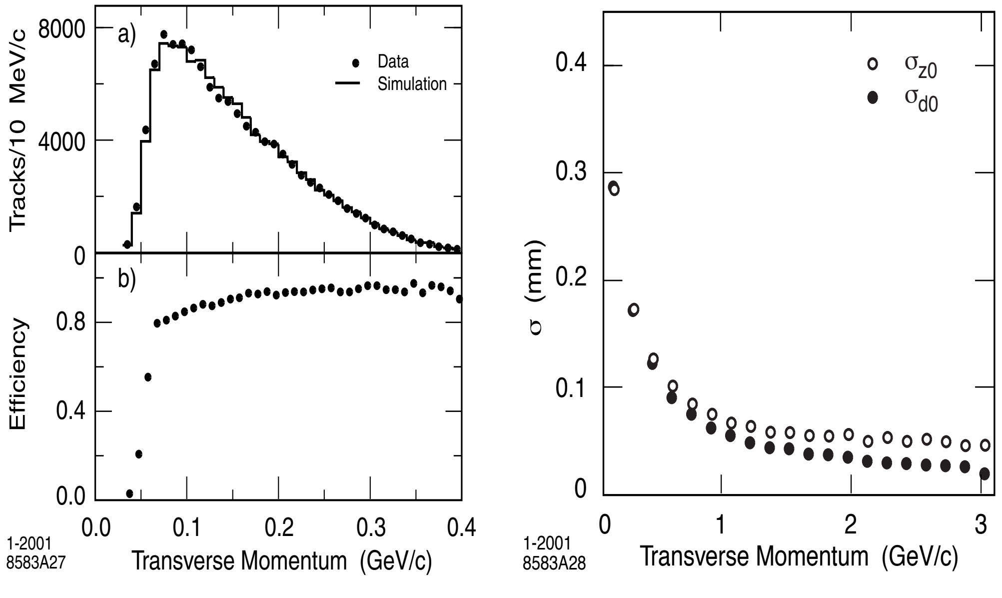

Figure 2.17: Left plot: MonteCarlo studies of low momentum tracks in the *SVT* on $D^{*+} \rightarrow D^0\pi^+$ events. a) comparison with data in $B\bar{B}$ events and b) efficiency for slow pion detection derived from simulated events. Right plot: resolution in the parameters d_0 and z_0 for tracks in multi-hadron events as a function of the transverse momentum.

The stand-alone SVT tracking algorithms have a high efficiency for tracks with low transverse momentum: to estimate the tracking efficiency for these low momentum tracks, a detailed MonteCarlo study was performed. The pion spectrum was derived from simulation of the inclusive D^* production in $B\bar{B}$ events and MonteCarlo events were selected in the same way as the data: since the agreement with MonteCarlo is very good, the detection efficiency has been derived from MonteCarlo simulation. The SVT extends the capability of the charge particle reconstruction down to transverse momenta of ~ 50 MeV$/c$ (see left plot in Fig. 2.17).

The resolution in the five track parameters is monitored using e^+e^- and $\mu^+\mu^-$ pair events: the resolution is derived from the difference of the measured parameters for the upper and lower halves of the cosmic ray tracks traversing the DCH and the SVT. On this sample with transverse momenta above 3 GeV$/c$, the resolution for single tracks is $23\,\mu m$ in d_0 and $29\,\mu m$ in z_0. To study the dependence of resolution from transverse momentum, a sample of multi-hadron events is used: the resolution is determined from the width of the distribution of the difference between the measured parameters (d_0 and z_0) and the coordinates of the vertex reconstructed from the remaining tracks in the event: right plot in Fig. 2.17 shows the dependence of the resolution in d_0 and z_0 as a function of p_t. The measured resolutions are about $25\,\mu m$ in d_0 and $40\,\mu m$ in z_0 for p_t of 3 GeV$/c$: these values are in good agreement with the MonteCarlo studies and in reasonable agreement also with the results from cosmic rays.

2.7.3 Particle Identification

Each of the five sub-detectors of BABAR can contribute to the determination of the particle specie of a given track. In this section we will not treat extensively the general topic of Particle Identification (PID), rather we will focus on the information used by the PID selectors relevant for our analysis.

2.7.3.1 Electrons

The PID selector used in our analysis for the selection of electrons, named `PIDLHElectrons`, uses the information from DCH (dE/dx), DIRC (number of detected photons and Cerenkov angle) and EMC (deposited energy, lateral and longitudinal shower shape) [29]. For each discriminating variable, probability density functions are constructed and, under the assumption of independent measurements from the individual subdetectors, they are combined to compute the likelihood $L(\xi)$ for each particle hypothesis $\xi \in e; \pi; K; p$:

$$L(\xi) = P(x_{EMC}, x_{DCH}, x_{DIRC}; \xi) = P(x_{EMC}; \xi)P(x_{DCH}; \xi)P(x_{DIRC}; \xi), \tag{2.4}$$

where x_{EMC}, x_{DCH} and x_{DIRC} represent vectors of discriminating variables from each subsystem.

Weighting the individual likelihoods with a priori probabilities p_ξ, the likelihood fraction f_L is computed:

$$f_L = \frac{p_e L(e)}{p_e L(e) + p_\pi L(\pi) + p_K L(K) + p_p L(p)}. \tag{2.5}$$

Using $p_e : p_\pi : p_K : p_p = 1 : 5 : 1 : 0.1$, a track is selected as electron if it passes some preselection cuts and a given cut on f_L, which may vary between 0 and 1. Figure 2.18 shows the typical performance of the `PIDLHElectrons` selector. The selection

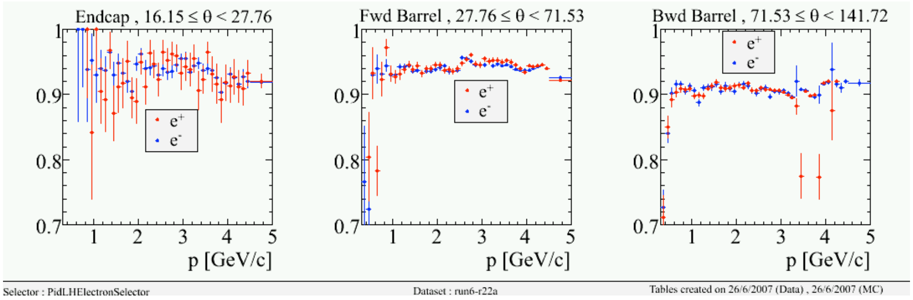

Figure 2.18: Performance of the `PIDLHElectrons` selector. The selection efficiency, as a function of momentum, in three different bins of the polar angle, is shown separately for e^- (blue dots) and e^+ (red).

efficiency is typically above 90% and there are no large charge asymmetries, excluding the forward region, severely affected by backgrounds.

2.7.3.2 Muons

The identification of muons relies mostly on the performance of the IFR. A set of simple cut based selectors has been developed for the selection of muon tracks at the beginning of the experiment. However, due to the non-optimal quantity of iron affecting the original design of the IFR and the fast degradation of the performance of RPCs, the development of more sophisticated algorithms proved to be necessary. In our analysis, muons are selected by using the `NNLooseMuonSelection` selector, which is based on the use of the Neural Network (NN) technique [30]. The variables used in the selection are (in the order as they appear on the input layer of the NN):

- $\Delta\lambda = \lambda_{exp}\lambda_{meas}$: the difference between the expected and the measured number of interaction length traversed by the track in the muon hypothesis;
- $\chi^2_{mat} = \chi^2/d.o.f.$ of the IFR hit strips in the cluster with respect to the track extrapolation;
- σ_m: the standard deviation of the average multiplicity of hit strips per layer;
- T_C: the continuity of the track in the IFR;
- E_{cal}: the energy deposited in the EMC;
- λ_{meas}: the number of interaction length traversed by the track;
- $\chi^2_{fit} = \chi^2/d.o.f.$ of the IFR hit strips with respect to a third order polynomial fit of the cluster;
- $\bar{m}$: the average multiplicity of hit strips per layer.

The NN implemented uses one input layer accepting the 8 variables listed above, one hidden layer with 16 nodes and one output layer with one node. Due to the different performance of the chambers in the different sections of the IFR (old and new RPC's, LST's) and the decrease with time of RPC's' performance, the training sample for the Neural Network has been split into several subsamples. Figures 2.19 and 2.20 show

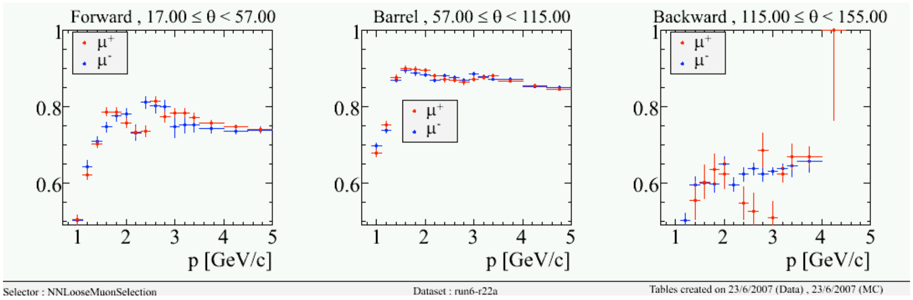

Figure 2.19: Performance of the `NNLooseMuonSelection`: the selection efficiency for separately μ^+ and μ^- as a function of momentum is shown in three different ranges of the polar angle.

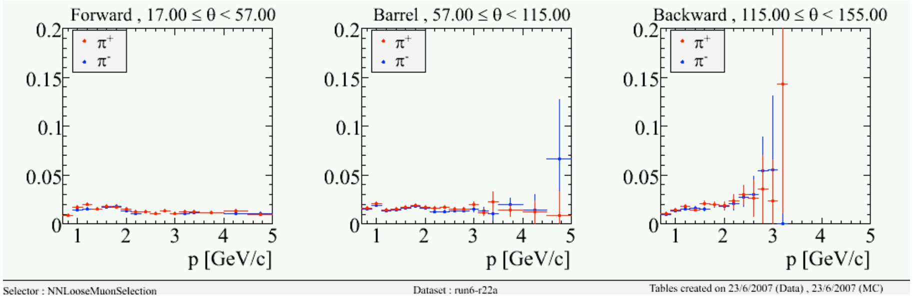

Figure 2.20: Performance of the `NNLooseMuonSelection`: the probability of π^+ and π^- to pass the selection as a function of momentum is shown in three different ranges of the polar angle.

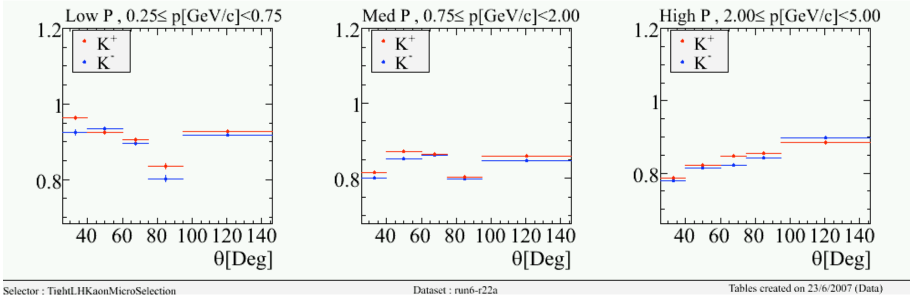

Figure 2.21: Performance of the `TightLHKaonMicroSelection`: the selection efficiency for separately K^+ and K^- as a function of the polar angle is shown in three different ranges of momentum. Charge asymmetries can be clearly seen.

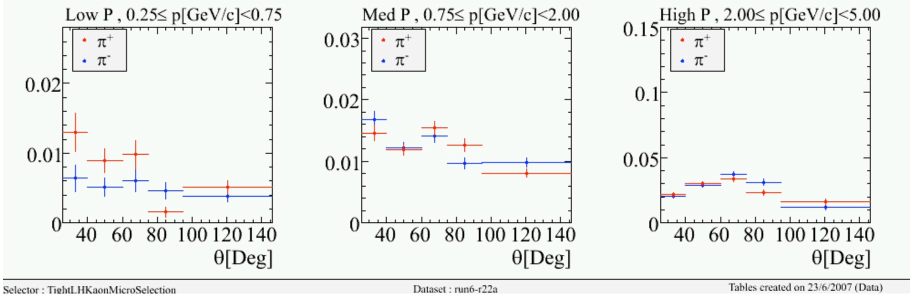

Figure 2.22: Performance of the `TightLHKaonMicroSelection`: the probability of π^+ and π^- to pass the selection as a function of the polar angle is shown in three different ranges of momentum. Charge asymmetries can be clearly seen.

the efficiency and the pion mis-identification rate for the selector we use in our analysis, averaged over Run1-Run6 data-taking periods.

2.7.3.3 Kaons

The signature of charged kaons in different detectors is complicated because they can decay or interact with the material of the detector. Furthermore, the hadronic interactions have different rates for the two charged modes. About 20% of the kaons decay before they reach the DIRC, and they mostly decay to a final state where there is only one charged track, which may be not distinguishable from the original one. We use the `TightLHKaonMicroSelection` selector, which combines the dE/dx measurements from SVT and DCH and the information from the DIRC [31]. The idea of the selector is to calculate a Likelihood for each particle hypothesis i: $L_i = L_{i,DIRC} \cdot L_{i,DCH} \cdot L_{i,SVT}$, where the measured dE/dx is compared against the expected dE/dx from the Bethe-Bloch parameterization.

Figures 2.21 and 2.22 show respectively the selection efficiency and pion mis-identification probability for different ranges of the polar angle and momentum. It can be clearly seen that a pretty large charge asymmetry exists in both the efficiency and the pion-fake rate, arising mainly from the different cross sections for K^+ hadronic interactions in the detector material with respect to K^-.

Chapter 3

B tagging and signal selection

In this chapter we describe the experimental and the Monte Carlo sample, the procedure of the B_{tag} reconstruction and the identification and calculation of the discriminators we use in the event selection.The analysis can be divided in three main conceptual parts:

- For each event we reconstruct a B meson through its main hadronic decays (B_{tag}). Different combinations of charged tracks and neutral candidates make possible multiple B reconstructed candidates. We require a single candidate per event selecting the one with the minimum difference between the energy of the reconstructed particle and half of the beam energy. Then we look for a signal consistent with the $B \to \tau\nu$ decay in the rest of the event, through the main τ decays: $\tau^- \to e^-\nu\bar{\nu}$, $\tau^- \to \mu^-\nu\bar{\nu}$, $\tau^- \to \pi^-\nu$, $\tau^- \to \rho^-\nu$.
- We identify criteria to enhance signal events ($B \to \tau\nu$) with respect to backgrounds. We optimize the selection criteria minimizing the expected uncertainty on the measurement. This part of the analysis and the following is the argument of the next chapter.
- The *Branching Fraction extraction*, by means of a maximum likelihood fit on the experimental data selected using the optimized criteria and the expected signal and background PDFs.

3.1 Data samples

3.1.1 Monte Carlo samples

The generation of the BABAR Monte Carlo simulation proceeds through the following steps:

1. **Generation of physical events**
   Creation of the e^+e^- collision products from theoretical models. The quark fragmentation in $e^+e^- \to q\bar{q}$, $q = (u, d, s, c)$ is taken into account and . $e^+e^- \to \Upsilon(4S) \to B^+B^-, \quad B^0\bar{B}^0$ and subsequent B decays are generated using the most recent experimental measurements on branching fractions and B physics models parameters [32].

2. **Particles interactions with the detector**
   A simulation software, based on *Geant4* [33], propagates the physics particles through the detector volume, simulating the interactions of the particles with the material of the detector. Multiple scattering, energy loss, particles creation and decays are taken into account. Moreover, the interaction with the active BABAR detector and the digitization of the response is simulated. Time dependent consitions of the detector subsystems are taken into account in the appropriate statistical way. In order to study the performances of the reconstruction algorithms the simulated physics event is saved (*Monte Carlo Truth*).

3. **Machine background simulation**
   The machine background is not simulated but taken from real data. An external random trigger records real events with a 1 Hz fixed rate. Those events are overlaid to the simulated events.

4. **Event reconstruction** The same reconstruction procedure is applied to both simulated and experimental data sample.

The different types of simulated events used in the analysis are

- $e^+e^- \to B^+B^-$, generic decays of both B mesons
- $e^+e^- \to B^0\bar{B}^0$, generic decays of both B mesons
- $e^+e^- \to q\bar{q}$ and hadronization, $q = (u, d, s, c)$.
- $e^+e^- \to \tau^+\tau^-$
- $e^+e^- \to B^+B^-$, $B^+ \to$ generic, $B^- \to \tau^-\bar{\nu}_\tau$, *signal Monte Carlo*.

We use the signal Monte Carlo to study the distribution of observables of the $B \to \tau\nu$ events and to evaluate selection efficiency. The signal Monte Carlo sample consists in roughly 23×10^6 events. The τ branching fraction used in the $B \to \tau\nu$ events generation is reported in table 3.1.

τ decay channel	Branching Fraction $(\%)$
$\tau^- \to e^-\nu\bar{\nu}$	18.00
$\tau^- \to \mu^-\nu\bar{\nu}$	17.51
$\tau^- \to \pi^-\nu$	11.04
$\tau^- \to \rho^-\nu$	25.15
other	28.30

Table 3.1: Branching fractions of the the different τ decays used in generation of signal Monte Carlo

3.1.2 Experimental data sample

We use the full BaBar dataset at $\Upsilon(4S)$ energy, collected from October 1999 to September 2007, corresponding to a number of B pairs $n_{B\bar{B}} = (467.8 \pm 5.1) \times 10^6$.

3.2 B tagging

3.2.1 B_{tag} reconstruction

We reconstruct the B_{tag} candidates through the following decay modes:

- $B^{\pm} \rightarrow D^{(*)0} X^{\pm}$
- $B^{0} \rightarrow D^{(*)\pm} X^{\mp}$
- $B^{0} \rightarrow D_s^{(*)\pm} X^{\mp}$
- $B^{\pm} \rightarrow J/\Psi X^{\pm}$

The $X^{\pm}$ system is a combination of neutral and charged hadrons made by $n_1\pi^{\pm} + n_2K^{\pm} + n_3\pi^0 + n_4K_S^0$ $(n_1 = 1\ldots5, n_2 = 0\ldots2, n_3 = 0\ldots2$ and $n_4 = 0, 1)$ with a total charge of ±1. The $D^{(*)0,\pm}$ candidates are reconstructed through a $D^{0,\pm}$ candidate and both a γ or a π^0 candidate. As γ candidates, we select reconstructed EMC clusters satisfying the following requirements:

- Cluster energy $E > 100$ MeV
- LAT < 0.8. LAT is the lateral moment of the cluster defined as

$$\frac{\sum_{i=2,n} E_i \cdot r_i^2}{(\sum_{i=2,n} E_i \cdot r_i^2) + R^2(E_0 + E_1)}; \tag{3.1}$$

  where the index i runs on each crystal hit, E_i is the energy of the i-th crystal, r_i is the distance of the i-th crystal from the cluster centroid and E_0 and E_1 are the highest and second highest energy clusters and R is the average lenght scale of a calotimeter cluster (5 cm) [34]. By definition, $0 <$ LAT < 1.

The π^0 candidate from $D^* \rightarrow D\pi^0$ transition consists of two photons with invariant mass in the range $[0.135\ldots0.155]$ GeV. A D^0 candidate is reconstructed from the following decays:

- $D^0 \rightarrow K^-\pi^+$
- $D^0 \rightarrow K^-\pi^+\pi^+\pi^-$
- $D^0 \rightarrow K^-\pi^+\pi^0$
- $D^0 \rightarrow K_S^0\pi^+\pi^-$
- $D^0 \rightarrow K_S^0\pi^+\pi^-\pi^0$

The candidates four-momenta are fitted, requiring a common vertex and a mode-dependent mass window around the PDG D^0 mass, 1.865 GeV [16](reported in table 3.2). In case of multiple candidates, we choose the one whose decay products have the highest probability from the fitting calculation of having a common vertex. The $D^{\pm}$ candidate is reconstructed through its decays:

- $D^{\pm} \rightarrow K_S^0\pi^{\pm}$
- $D^{\pm} \rightarrow K^{\pm}\pi^0\pi^0$

Decay Mode	Mass Windows in GeV
$D^0 \rightarrow K^-\pi^+$	± 0.09
$D^0 \rightarrow K^-\pi^+\ \pi^+\ \pi^-$	± 0.09
$D^0 \rightarrow K^-\pi^+\ \pi^0$	± 0.160
$D^0 \rightarrow \bar{K_s}^0\pi^+\ \pi^-$	± 0.09
$D^0 \rightarrow \bar{K_s}^0\pi^+\ \pi^-\ \pi^0$	± 0.070

Table 3.2: Mass-windows for the D^0 reconstruction around the PDG D^0 mass (1.865 GeV).

- $D^\pm \rightarrow K^0_S\pi^\pm\pi^0$
- $D^\pm \rightarrow K^\pm\pi^+\pi^-\pi^0$
- $D^\pm \rightarrow K^0_S\pi^+\pi^-\pi^\pm$

The J/Ψ candidate is reconstructed through its decays $J/\Psi \rightarrow e^+e^-$ and $J/\Psi \rightarrow \mu^+\mu^-$, fitting the lepton four-momenta to a common vertex and requiring contraints on the invariant mass. For each reconstructed B_{tag} we determine two kinematical and one topological observables:

- The difference between the energy of the B and half of the beam energy in the center mass frame

  $$\Delta E = E^*_B - \sqrt{s}/2, \tag{3.2}$$

  where E^*_B is the energy of the reconstructed B meson and $\sqrt{s}/2$ is half of the beam energy, both in the $\Upsilon(4S)$ centrer mass system. The expected value of ΔE for correctly reconstructed B is $\Delta E = 0$. In figure 3.1 we show the distribution of ΔE for the signal Monte Carlo sample and the data sample.

- *Energy Substituted Mass* defined as

  $$m_{ES} = \sqrt{[(s/2 + \mathbf{p}_i \cdot \mathbf{p}_B)^2/E_i^2] - |\mathbf{p}_B|^2}, \tag{3.3}$$

  where $(E_i, \mathbf{p}_i)$ and $(E_B, \mathbf{p}_B)$ are respectively the e^+e^- four-momentum and the B candidate four-momentum, both in the laboratory frame. The distribution of correctly reconstructed B is expected to be approximatively gaussian with average m_B and standar deviation ~ 3 MeV. In fig. 3.2 we report the distribution of m_{ES} for signal Monte Carlo sample and for data sample.

- $|\cos\theta_T|$, the cosine of the angle θ between the B_{tag} thrust axis $\mathcal{T}_{tag}$ and the thrust axis of the rest of the event $\mathcal{T}_{ROE}$, with thrust axis defined as:

  $$\mathcal{T} = \text{max}_n \mathcal{T}(\mathbf{n}) = \text{max}_n \frac{\sum_i |p^*_{i||}|}{\sum_i |\mathbf{p}^*_i|} \tag{3.4}$$

  where $p^*_{i||}$ is the projection of the i-th particle momentum on the direction defined by the $\mathbf{n}$ versor. All the quantities are calculated in the center mass system. In fig. 3.3 we report the signal Monte Carlo sample and the data sample distribution for this quantity.

The different combinations of tracks and neutral candidates can give multiple B_{tag} candidate per event. In order to have one B_{tag} candidate per event we select the one with the smallest $|\Delta E|$.

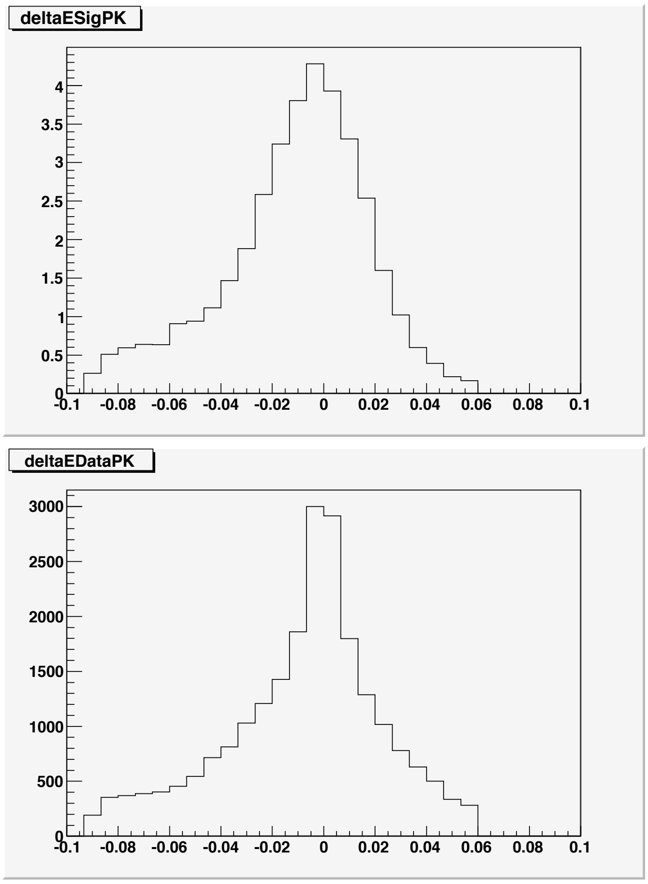

Figure 3.1: Distribution of ΔE for the signal Monte Carlo sample (top) and data sample (bottom). The recoil B is reconstructed as $B \rightarrow \tau\nu$, $\tau^- \rightarrow e^-\nu\bar{\nu}$.

3.2.2 Recoil B reconstruction

After the assignment of tracks and neutral objects to the B_{tag}, the remainder of the event is examined for evidence of:

1. additional hadronic B decay (*Hadronic double tag*)
2. $B^{\pm} \rightarrow D^{(*)0} l^{\pm} \nu X$ decay (*Hybrid double tag*)
3. τ decay in one of the following modes, in the order reported below (*signal*):
    (a) $\tau^- \rightarrow \mu^-\nu\bar{\nu}$
    (b) $\tau^- \rightarrow e^-\nu\bar{\nu}$
    (c) $\tau^- \rightarrow \rho^-\nu$
    (d) $\tau^- \rightarrow \pi^-\nu$.

They represent the 71.6 % of all τ decay modes.

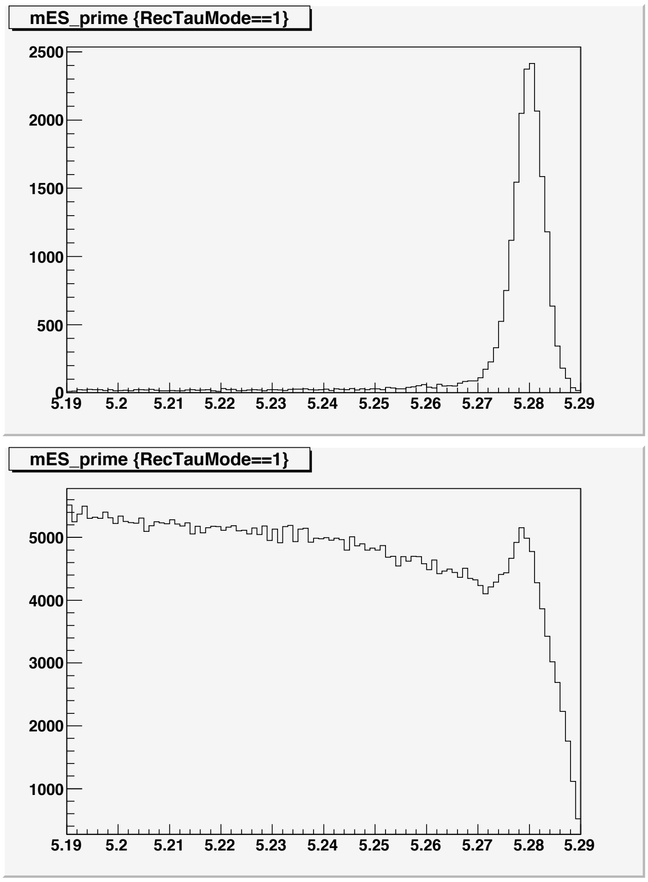

Figure 3.2: Distribution of m_{ES} for the signal Monte Carlo sample (top) and data sample (bottom). The recoil B is reconstructed as $B \to \tau\nu$, $\tau^- \to e^-\nu\bar{\nu}$.

To select an event in the hadronic double tag category, we apply the same reconstruction of the first tag to the rest of the event (two non-overlapping B_{tag} candidates) and require for both B candidates $5.23\,\text{GeV}/c^2 \leq m_{ES} \leq 5.30\,\text{GeV}/c^2$.
To select an event as $B^\pm \to D^{(*)0} l^\pm \nu X$, we reconstruct a $D^{(*)0}$ candidate and a lepton. The $D^{(*)0}$ is reconstructed following the procedure described in sec. 3.2.1. The charged track identified as lepton is required to pass the electron or muon selection criteria described in sec. 2.7.3. It is also required to have a momentum $p > 0.9\,\text{GeV}$ in the CM system.
In the events where no double tags are found, the consistency with one of the four main τ decays modes is tested. To identify the τ decay we apply the following requirements to the charged tracks:

- Maximum momentum lower than 10 GeV
- Maximum DOCA in the XY plane 1.5 cm
- Minimum Z DOCA -2 cm
- Maximum Z DOCA 2 cm

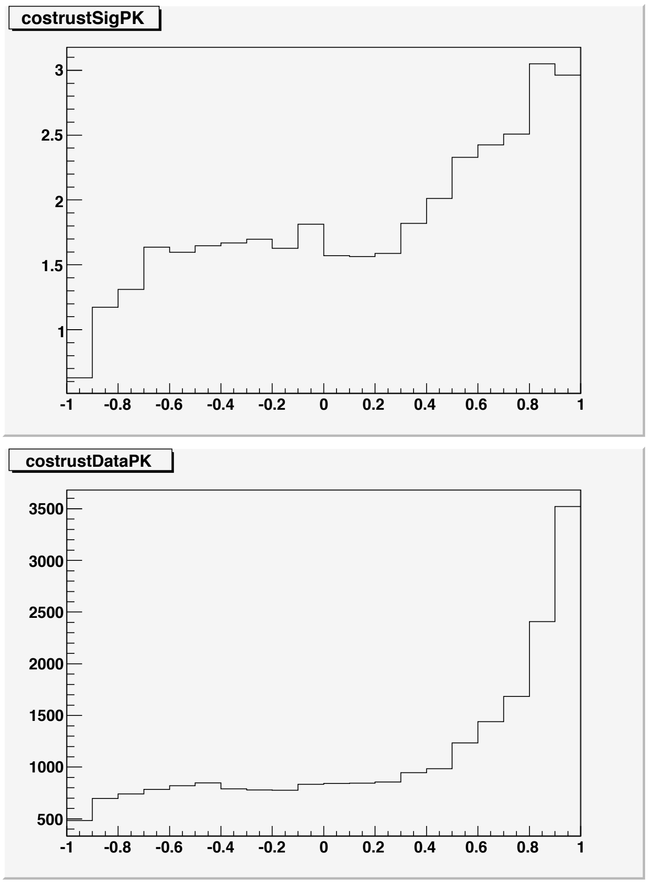

Figure 3.3: Distribution of $|\cos\theta_T|$ for the signal Monte Carlo sample (top) and data sample (bottom). The recoil B is reconstructed as $B \to \tau\nu$, $\tau^- \to e^-\nu\bar{\nu}$.

where DOCA is the *"Distance of closest approach"* of the track with respect to the interaction point in the XY plane or in Z plane. We select events with only one track satisfying the above requirements. We then require the track to pass the muon ID criteria (see sec. 2.7.3). If those criteria are satisfied, the event is classified as $\tau^- \to \mu^-\nu\bar{\nu}$ candidate. If the moun requirements are not satisfied, the track is tested for electron identification to be classified as $\tau^- \to e^-\nu\bar{\nu}$ candidate. In events in which the track does not pass either of these selectors, we look for a $\rho^\pm$ candidate by combining the track with a π^0 candidate. The $\rho^\pm$ candidate's momenta are fitted to a single point of origin and the invariant mass of the candidate before and after the fit has to be between 0.4 and 1.2 GeV. If multiple ρ's are possible, we select the one with the unconsrained mass closest to the PDG value ($0.775\,\mathrm{GeV}/c^2$). The remaining events are assigned to the $\tau^- \to \pi^-\nu$ category.

3.2.3 Decay mode purity

Before choosing the unique B_{tag} we calculate the purity associated to each decay mode. The procedure for the purity calculation is:

- select as best B_{tag} the one with the lowest value of $|\Delta E|$
- split the sample by decay mode of the B_{tag} and require the events to have $|\cos\theta_T| < 0.5$ to enhance m_{ES} peaking events
- fit the m_{ES} distributions of each subsample using an Argus function [35] to model the non-peaking component and a Crystal Ball function [36] to model the peaking component. We evaluate the number of peaking events and non-peaking events in the region $m_{ES} > 5.27\,\text{GeV}/c^2$, as the integral of the Crystal Ball and the Argus in the selected region (respectively n_p and n_{np})
- define purity as $n_p/(n_p + n_{np})$, in order to have a purity value for each reconstructed decay mode.

We repeat the whole procedure to re-calculate purity, but selecting the best B_{tag} as the one with the lowest purity. Finally we do a third iteration of the procedure. The purity values obtained from the third iteration are very similar to previous results, so we stop and assign as purity of the reconstruction mode what we obtain from the last calculation. We perform the analysis using different minimum purity requirements (0%, 5%, 7.5%, 10%, 12.5% and 15%).

3.3 Tag selection efficiency

The branching fraction can be extracted from:

$$BF = \frac{N_{sel} - N_{bkg}}{N_{B^\pm,true} \cdot \epsilon_{reco-sel,giventag} \cdot \epsilon_{tag,insignal,Data}} \tag{3.5}$$

where N_{sel} is the number of events passing the selection, N_{bkg} is the number of expected background events, $N_{B^\pm,true}$ is the true number of charged B mesons. The selection efficiency is conventionally broken into two contributions: $\epsilon_{tag,insignal,Data}$, the efficiency for a signal event to pass the tag reconstruction, and $\epsilon_{reco-sel,giventag}$, the efficiency for a tagged signal event to pass the final selection criteria. The former is estimated with the signal Monte Carlo, as the ratio between the number of generated events and the number of events passing the B tagging. The efficiency is different for the different τ decay channels. Table 3.3 reports composition in τ decay of the signal sample after the B tagging at different purities, evaluated from the *Monte Carlo truth* informations.

τ decay channel	frac. (%) No cut	frac. (%) Pur 5%	frac. (%) Pur 7.5%	frac. (%) Pur 10%	frac. (%) Pur 12.5%	frac. (%) Pur 15%
$e\nu\bar{\nu}$	13.5	15.3	17.7	18.5	18.8	19.3
$\mu\nu\bar{\nu}$	14.5	15.7	17.4	18.3	18.5	18.8
$\pi\nu$	10.0	10.8	11.8	12.3	12.4	12.7
$\rho\nu$	27.0	27.2	26.9	27.0	27.1	26.8
other	35.0	30.9	26.2	24.0	23.1	22.5

Table 3.3: Different contributions from τ decay channels in signal sample, after B tagging plus Best B, at different minimum purity requirements.

3.3.1 Tagging efficiency systematics

The difference between tag efficiency in signal $B \rightarrow \tau\nu$ events and generic B decays events can be as large as 20%. Moreover, the efficiencies estimated from Monte Carlo simulation may be significantly different from the efficiency found in data, due to data/Monte Carlo disagreements in B decay modes branching fractions, and reconstruction efficiencies. Another distorsion in B decay mode composition, when comparing the signal and background, come from different multiplicity in the signal states that increases the probability of reconstructing a combinatoric B as B_{tag}. Assuming that data/Monte Carlo disagreement is the same for generic vs signal decays we can use this relation:

$$\epsilon_{tag,insignal,Data} = \epsilon_{tag,insignal,MC} \frac{\epsilon_{tag,generic,Data}}{\epsilon_{tag,generic,MC}} \tag{3.6}$$

We evaluate $\epsilon_{tag,insignal,MC}$ from signal Monte Carlo and the ratio $\epsilon_{tag,generic,Data}/\epsilon_{tag,generic,MC}$ in a control sample made of double tagged events.

3.3.2 Data/Monte Carlo corrections

We perform the study of tag B correction using "hybrid" double tag events in which the second ("signal") B contains a $D^{*}l\nu$ candidate. We determine the number of m_{ES} peaking events by means of a maximum likelihood fit with two Argus to model the non-peaking component and a Crystal ball function to model the peaking component. We require $|\text{cos}\theta_T| < 0.5$ to enhance the peaking component. In order to verify that the composition of the decay modes does not change when we apply the $|\cos\theta_T|$ cut, biasing the results, we look at the *Monte Carlo truth* information.
Figure 3.4 shows the purity distribution for generic B-event with and without a *truth matching* requirement, with $|\cos\theta_T| > 0.5$ or $|\cos\theta_T| < 0.5$. We find that the $|\cos\theta_T|$ does not distort the purity distribution.

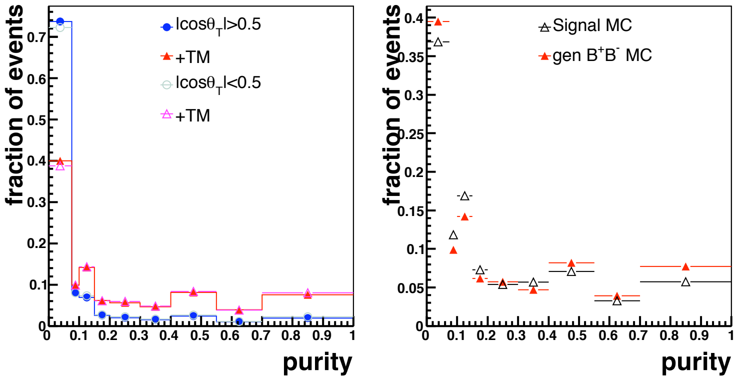

Figure 3.4: Purity composition of signal and generic Monte Carlo events. The left hand side compares the purity compositions of events with $|\text{cos}\theta_T|$ smaller and greater than 0.5. It also shown this distributions for all generic B decays events and the ones that pass a truth-matching requirement. The right hand side compares this distributions for generic and signal MC events.

We perform the fits to evaluate the corrections with the following procedure:

- normalize the Monte Carlo to data using luminosity scale factors and the branching fractions reported in table 2.1
- fit the continuum Monte Carlo ($\tau^+\tau^-$, uds and $c\bar{c}$), with an Argus function
- fit the "combinatoric" Monte Carlo (continuum + $B^0\overline{B^0} \times 2$) with 2 Argus, setting the starting parameters of the first to the parameter obtained by the continuum fit
- fit the MC with 2 Argus functions and a Crystal Ball (using the starting Argus parameter from the previous fit)
- fit the Data with 2 Argus functions and a Crystal Ball (using the parameters from the MC fit as starting parameters)

We assume that the combinaric component of the B^+B^- Monte Carlo sample is similar to the $B^0\bar{B}^0$, so we add twice the $B^0\overline{B^0}$ to the continuum MC. The correction is the ratio between peaking events in data and peaking events in Monte Carlo. We include the purity requirement in the correction evaluation. In figure 3.5 we report examples of m_{ES} fits to the “Hybrid” double tag sample, while in table 3.4 we report the computed values of tagging efficiency, the correction and the corrected efficiency.

Purity min	No cut	5%	7.5%	10%	12.5%	15%
Tag Eff (%)	0.79	0.53	0.32	0.24	0.20	0.15
Corr	0.88	0.86	0.88	0.91	0.93	0.93
Corr Eff (%)	0.70	0.46	0.29	0.22	0.19	0.14

Table 3.4: B tagging plus Best B selection efficiency at different minimum purity requirements, correction factors calculated from “Hybrid” double tag events and corrected efficiency.

3.4 Signal selection

3.4.1 Background classification

We classify the background events in two categories:

- *peaking background*: events with a correctly reconstructed B_{tag}. The m_{ES} shape of this background is modelled by a Crystal Ball function centered at the nominal B mass ($5.28\,\mathrm{GeV}/c^2$). We determine the Crystal Ball parameters by means of maximum likelihood fits.
- *non-peaking background*: events with misreconstructed charged B. This backround has two sources:
    - continuum component, from $e^+e^- \to c\bar{c}$ decays or $e^+e^- \to u\bar{u}, d\bar{d}, s\bar{s}$
    - combinatorial component, from $\Upsilon(4S) \to B^+B^-$ events in which the B_{tag} has not been well reconstructed. Note that also the $\Upsilon(4S) \to B^0\bar{B}^0$ events contribute to this background.

Looking at a generic m_{ES} distribution we define two regions:

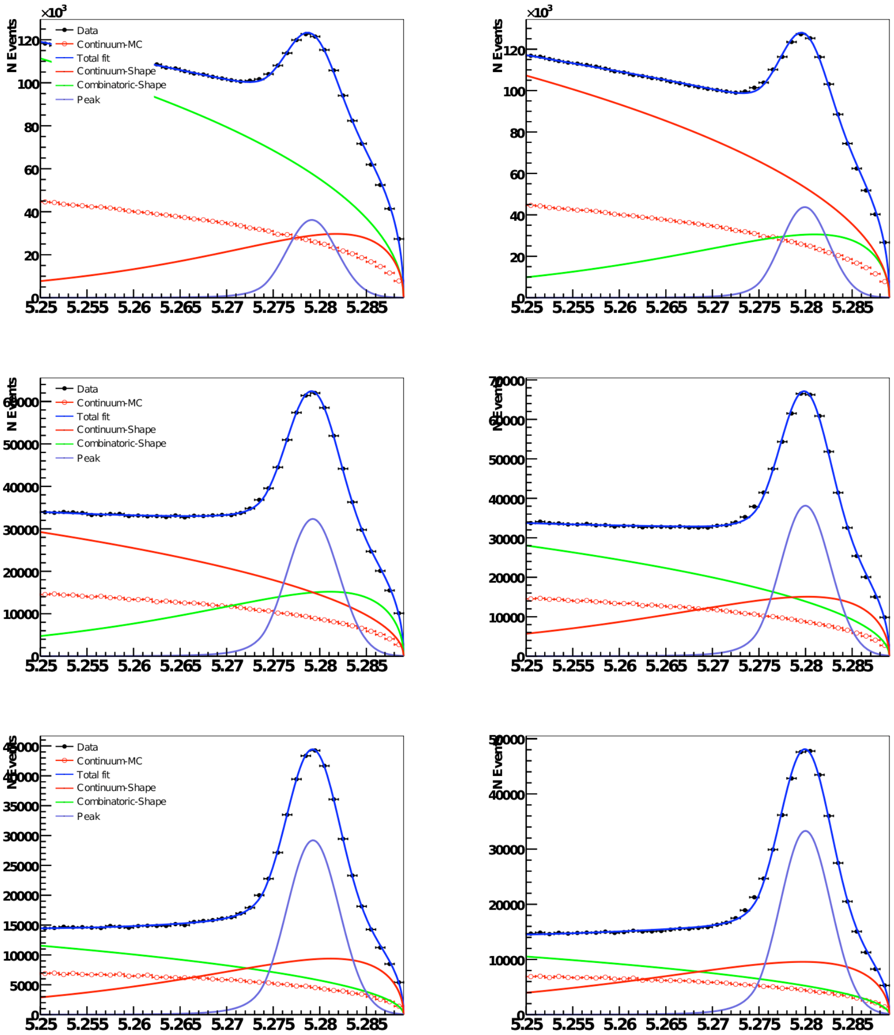

Figure 3.5: m_{ES} fit for the “Hybrid” double tag using two Argus and a Crystal Ball. First raw is for 5% minimum purity requirement, second one is for 7.5% and third one for 10%. Left column represents data and right column represents the Monte Carlo of the different data sample component

- m_{ES} *sideband*, with $5.209\,\mathrm{GeV}/c^2 < m_{ES} < 5.26\,\mathrm{GeV}/c^2$
- m_{ES} *peaking*, with $5.27\,\mathrm{GeV}/c^2 < m_{ES} < 5.289\,\mathrm{GeV}/c^2$

Figure 3.6 shows the two regions in a m_{ES} distribution of a preselected sample with an electron in the recoil. We evaluate the distributions of the observables for the non-peaking background from the sideband region of the data sample, assuming that there is no correlation between the observables and the m_{ES} value. The distributions of the kinematics and topological observables for the peaking background are taken from the m_{ES} peaking region of the B^+B^- Monte Carlo sample. The B^+B^- events have a

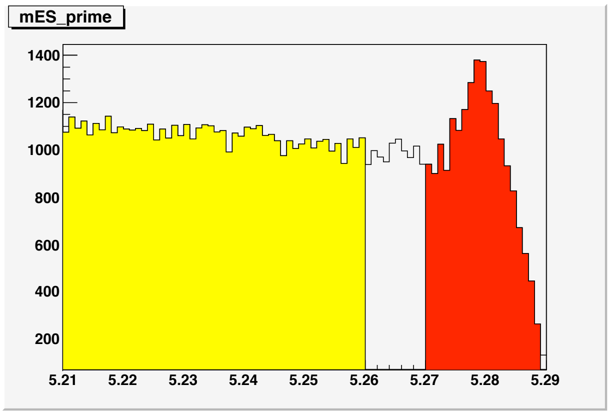

Figure 3.6: An m_{ES} distribution (data sample, electron channel). The sideband region is coloured in yellow, the peaking region in red.

non-negligible amount of non-peaking background, so we extract the distribution of this component from the m_{ES} sideband and subtract it from the m_{ES} peaking region, as discussed later.

3.4.2 Preliminary requirements

3.4.3 Purity requirement

A minimum requirement on purity (see section 3.2.3) reduce the combinatoric background at the price of reducing the statistics available. We perform the selection using different values for the minimum purity requirement to find an optimal configuration. We choose the optimized level in a later step, when we will calculate the expected error on the branching fraction extraction. This choice corresponds to 12.5% of minimum purity and it will be justified in section 4.4. So, except where explicitely stated, every plot or table in the following is referred to a 12.5% of minimum purity requirement.

3.4.3.1 Extra charged track requirement

We require exactly one well reconstructed charged track not assigned to $B_{\rm tag}$ satisfying the selection criteria described in section 3.2.2, but we accept extra soft charged tracks that fail the quality requirements (*extra charged tracks*). Figure 3.7 we show the distribution of extra charged tracks for the different Monte Carlo samples: the signal sample shows a negligible part of events with more than 1 charged track, while we have an higher fraction of those events in the background. We require no more than 1 extra charged track per event.

3.4.3.2 $e^+e^- \to \tau^+\tau^-$ rejection

We expect few $e^+e^- \to \tau^+\tau^-$ events, but this background is particulary "dangerous" because the physics of the event is similar to the one of $B \to \tau\nu$. Therefore we reject $e^+e^- \to \tau^+\tau^-$ events using the *R2All* variable, defined as the 2nd Fox-Wolfram Moment divided by the 0th Fox-Wolfram Moment including all the charged tracks and

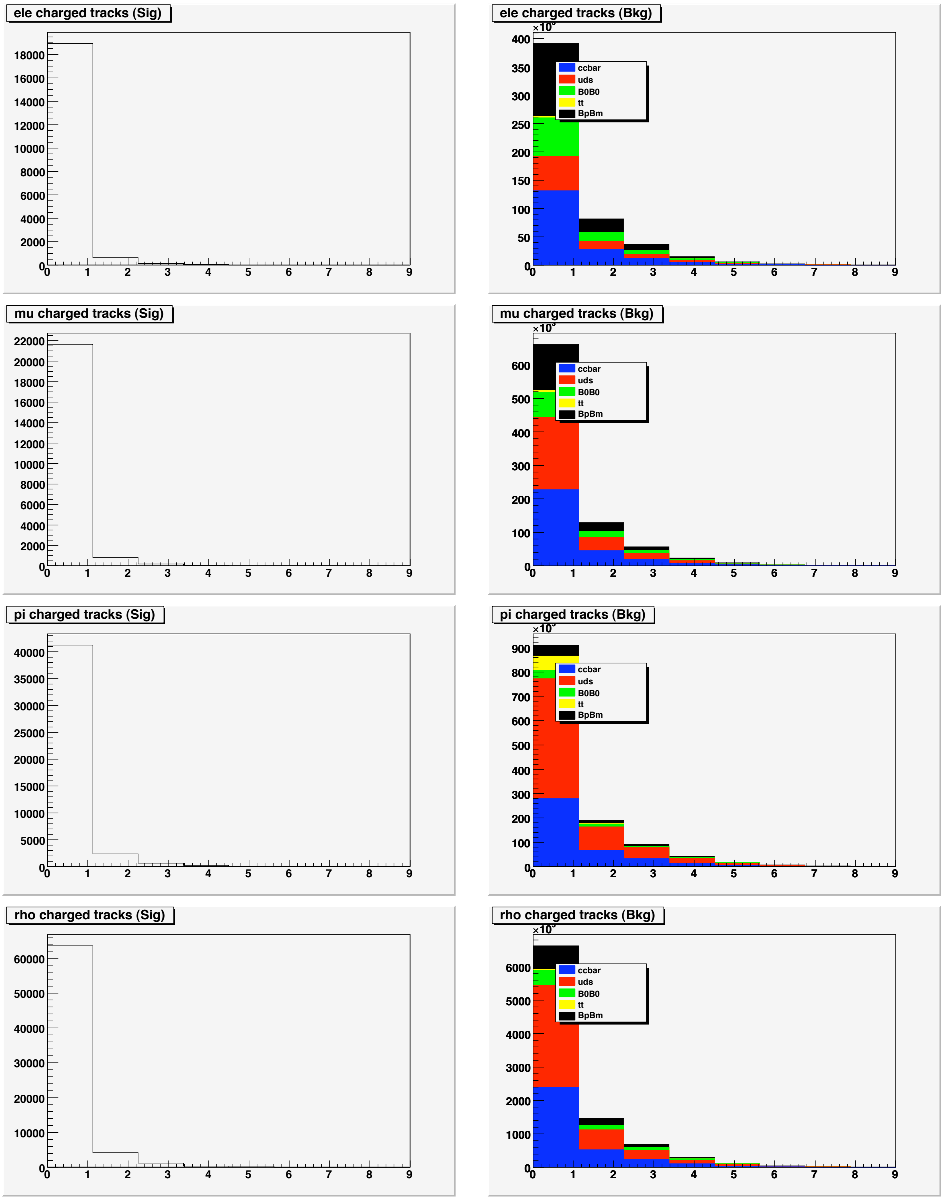

Figure 3.7: Distributions of extra charged tracks for signal (left column) and all background components (right column). First row refers to electron channel, second to muon channel, third to pion channel and fourth to rho channel.

the neutral cluster in the event. The Fox-Wolfram Moments $H_l, \quad l = 0, 1, 2, \ldots$ are defined by[37]:

$$H_l = \sum_{i,j} \frac{|\mathbf{p}_i||\mathbf{p}_j|}{E^2_{\text{vis}}} P_l(\cos\theta_{ij}), \tag{3.7}$$

where θ_{ij} is the opening angle between charged tracks or neutral cluster centroid i and j and E_{vis} the total visible energy of the event. The $P_l(x)$ are the Legendre polynomials.

In fig. 3.8 we can see the distribution of the *R2All* variable for signal events and $e^+e^- \to \tau^+\tau^-$ events (taken from $e^+e^- \to \tau^+\tau^-$ Monte Carlo). The *R2All* value is higher for background events, so we set a cut to preserve 90% of *Monte Carlo Truth Matched* signal, in the m_{ES} peaking region ($m_{ES} > 5.27\,\text{GeV}/c^2$), with the charged track requirement applied. The *Monte Carlo Truth Matched* is a sub-sample of the signal Monte Carlo where we require:

- τ decay mode in the reconstruction equal to the τ decay channel of the Monte Carlo generation
- number of reconstructed charged tracks associated to the B_{tag} equal to the number of generated charged tracks of one of the two B mesons.

In table 3.5 we show the value of the *R2All* cut for each τ mode and the fraction of accepted signal and rejected background.

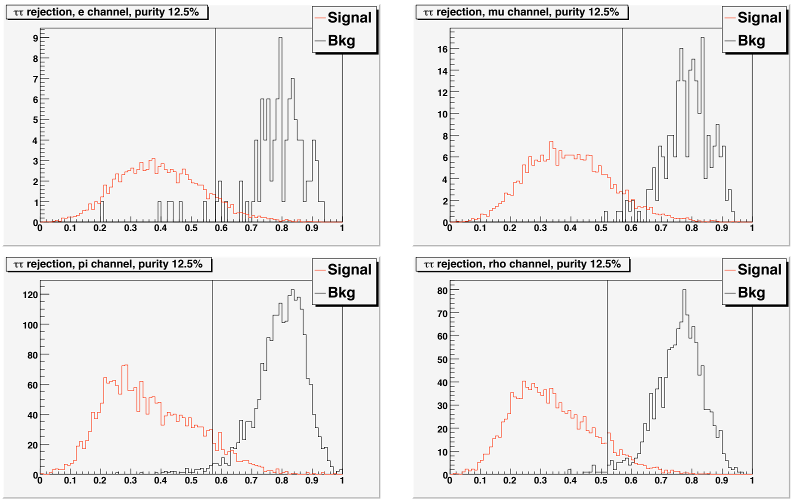

Figure 3.8: Distribution of *R2All* for $B \to \tau\nu$ *Monte Carlo Truth associated* signal (red) and $e^+e^- \to \tau^+\tau^-$ background (black) in the m_{ES} peaking region, with no extra charged tracks required for $\tau^- \to e^-\nu\bar{\nu}$ (top-left), $\tau^- \to \mu^-\nu\bar{\nu}$ (top-right), $\tau^- \to \pi^-\nu$ (bottom-left) and $\tau^- \to \rho^-\nu$ (bottom-right). Signal distributions are normalized to background distributions. Minimum purity requirement is 12.5%.

3.5 Background estimation and Data-Monte Carlo agreement

We fit the m_{ES} distributions in the B^+B^- Monte Carlo and in data sample with an Argus function plus a Crystal Ball function determining the signal and background yields and the parameters of the signal and background shapes. From the fitted parameters we extract:

Purity min	R2All max.	Signal eff (%)	$\tau\tau$ rej. (%)
Electron			
0%	0.53	89.4	95.0
5%	0.54	89.5	93.8
7.5%	0.56	89.6	93.7
10%	0.57	89.4	93.4
12.5%	0.58	89.4	94.1
15%	0.58	88.7	95.8
Muon			
0%	0.53	90.0	97.7
5%	0.54	89.8	97.0
7.5%	0.55	89.3	98.2
10%	0.56	89.1	99.1
12.5%	0.57	89.1	98.7
15%	0.58	89.6	99.4
Pion			
0%	0.52	89.6	98.5
5%	0.53	89.7	98.3
7.5%	0.55	89.7	98.2
10%	0.56	89.5	98.3
12.5%	0.57	89.8	98.1
15%	0.57	89.1	98.6
Rho			
0%	0.47	89.0	98.9
5%	0.48	89.0	98.6
7.5%	0.50	89.4	98.9
10%	0.51	89.1	99.0
12.5%	0.52	89.1	98.9
15%	0.53	89.5	98.4

Table 3.5: Signal efficiency and $e^+e^- \to \tau^+\tau^-$ rejection after the *R2All* cut for each τ decay channel and for the different used minimum purity requirements.

- the peaking yield in B^+B^- Monte Carlo X_{pk}^{mc}
- the peaking yield in data X_{pk}^{data}
- the area of the non-peaking backgrounds distribution under the signal peak in B^+B^- Monte Carlo A_{pk}^{mc}
- the area of the non-peaking backgrounds distribution in the m_{ES} sideband in B^+B^- Monte Carlo A_{sb}^{mc}
- the area of the non-peaking backgrounds distribution under the signal peak in data A_{pk}^{data}
- the area of the non-peaking backgrounds distribution in the m_{ES} sideband in data A_{sb}^{data}

The distribution of a generic variable for the non-peaking background events in the m_{ES} signal region is determined scaling the distribution of the variable in the m_{ES}

data sideband by the ratio $A_{pk}^{data}/A_{sb}^{data}$. The m_{ES} peaking background events are taken from the B^+B^- Monte Carlo. We subtract the non-peaking component in the m_{ES} signal region to avoid double counting. This sideband subtraction is performed in the same way as in data, using the appropriate ratio A_{pk}^{mc}/A_{sb}^{mc}. We scale the sideband subtracted distribution by the $X_{pk}^{mc}/X_{pk}^{data}$ ratio to normalize the Monte Carlo to data. In other words,

- the non-peaking background is taken from the m_{ES} data sidebands
- the peaking component shape is evaluated from B^+B^-Monte Carlo (with the simulated combinatorial component removed)
- the scaling factor for normalizing B^+B^- Monte Carlo to data is taken from the ratio of peaking B yields

We use this procedure to show Data-Monte Carlo agreement and compare the signal and background distributions. Moreover, we determine the amount of non-peaking background (n_{np}) from data sideband and peaking background (n_{pk}) from B^+B^- Monte Carlo at a given selection level as follows:

$$n_{np} = n_{sb}^{data} \frac{A_{pk}^{data}}{A_{sb}^{data}} \tag{3.8}$$

$$n_{pk} = \left(n_{pk}^{mc} - n_{sb}^{mc} \frac{A_{pk}^{mc}}{A_{sb}^{mc}} \right) \frac{X_{pk}^{data}}{X_{mc}^{data}} \tag{3.9}$$

We perform the fits in an E_{extra} sideband region ($E_{extra60} > 500 MeV$), where the contribution of $B \to \tau\nu$ signal in the peaking region is negligible. The factor $X_{pk}^{data}/X_{mc}^{data}$ normalizes the B^+B^- Monte Carlo distributions to data, in the hypotesis of no $B \to \tau\nu$ signal events, then we can compare the data in the m_{ES} peaking region with the background prediction coming from m_{ES} sideband and B^+B^- Monte Carlo. The amount of $B \to \tau\nu$ signal events in real data does not affect the variable's data/Monte Carlo agreement, except for E_{extra} (see next section), where the signal accumulates in a small region of the distribution (strongly peaks at 0). The m_{ES} distributions with the fit projection overlaid, for data and B^+B^- Monte Carlo, are reported in fig.3.9 and fig.3.10, and the results are in tables 3.6 and 3.7. Figg. from 3.11 to 3.15 show the data-Monte Carlo agreement at preselection level for discriminating variables, and figg. 3.16-3.19 show the agreement of the peaking component only.

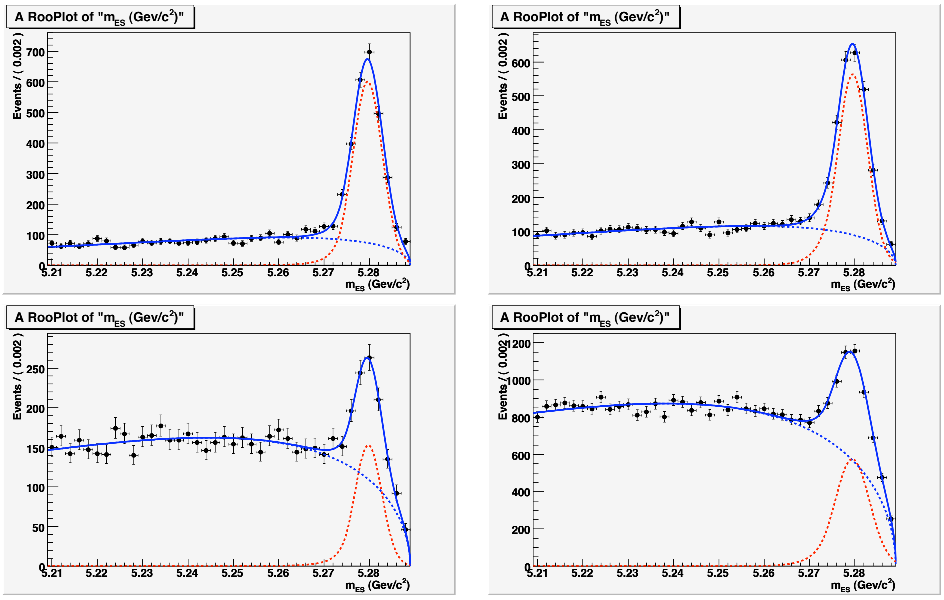

Figure 3.9: Data sample: m_{ES} fitted distributions at preselection level; electron channel (top-left), muon channel (top-right), pion channel(bottom-left) and rho channel (bottom-right).

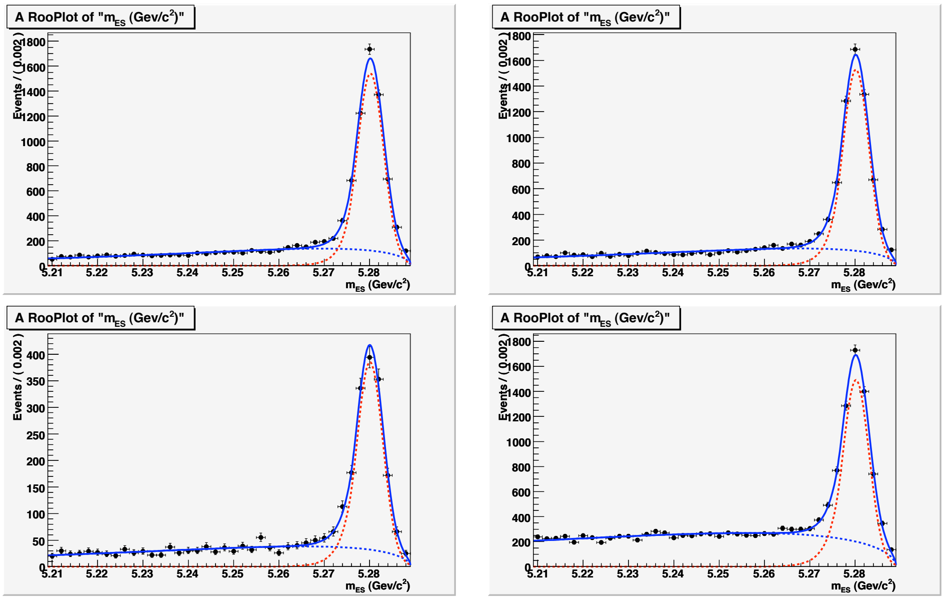

Figure 3.10: B^+B^- Monte Carlo sample: m_{ES} fitted distributions at preselection level; electron channel (top-left), muon channel (top-right), pion channel(bottom-left) and rho channel (bottom-right).

Channel	e	μ
n_{sb}	1978 ± 46	2678 ± 53
n_{pk}^{Ar}	643 ± 15	786 ± 16
n_{pk}^{CB}	2472 ± 67	2354 ± 68
<CB>(GeV)	5.27961 ± 0.00005	5.27952 ± 0.00009
CB σ (MeV)	3.27 ± 0.09	3.28 ± 0.09
Argus ξ	-47.6 ± 3.3	-41.1 ± 2.8
Channel	π	ρ
n_{sb}	4015 ± 62	21824 ± 151
n_{pk}^{Ar}	975 ± 15	5005 ± 34
n_{pk}^{CB}	579 ± 51	2742 ± 127
<CB>(GeV)	5.2798 ± 0.0008	5.27942 ± 0.00015
CB σ (MeV)	2.98 ± 0.26	3.81 ± 0.16
Argus ξ	-29.2 ± 2.2	-25.7 ± 1.0

Table 3.6: m_{ES} fit results for the 4 τ decay channels in data sample. The quantities reported are: n_{sb}, the argus area in the sideband region; n_{pk}^{Ar} the argus area in the peaking region; n_{pk}^{CB}, the Crystal Ball area in the peaking region; the Crystal Ball mean value; the value of the Crystal Ball σ; the value of the Argus ξ parameter.

Channel	e	μ
n_{sb}	2374 ± 51	2485 ± 52
n_{pk}^{Ar}	1068 ± 23	1025 ± 22
n_{pk}^{CB}	5746 ± 96	5700 ± 95
<CB>(GeV)	5.28018 ± 0.00005	5.28016 ± 0.00005
CB σ (MeV)	2.91 ± 0.05	2.89 ± 0.05
Argus ξ	-68.6 ± 3.0	-63.0 ± 3.0
Channel	π	ρ
n_{sb}	766 ± 29	6282 ± 80
n_{pk}^{Ar}	283 ± 11	1801 ± 23
n_{pk}^{CB}	1445 ± 48	5612 ± 102
<CB>(GeV)	5.28007 ± 0.00010	5.28018 ± 0.00005
CB σ (MeV)	2.88 ± 0.09	2.89 ± 0.05
Argus ξ	-55.8 ± 5.2	-39.6 ± 1.8

Table 3.7: m_{ES} fit results for the 4 τ decay channels in B^+B^- Monte Carlo sample. The quantities reported are: n_{sb}, the argus area in the sideband region; n_{pk}^{Ar} the argus area in the peaking region; n_{pk}^{CB}, the Crystal Ball are in the peaking region; the Crystal Ball mean value; the value of the Crystal Ball σ; the value of the Argus ξ parameter.

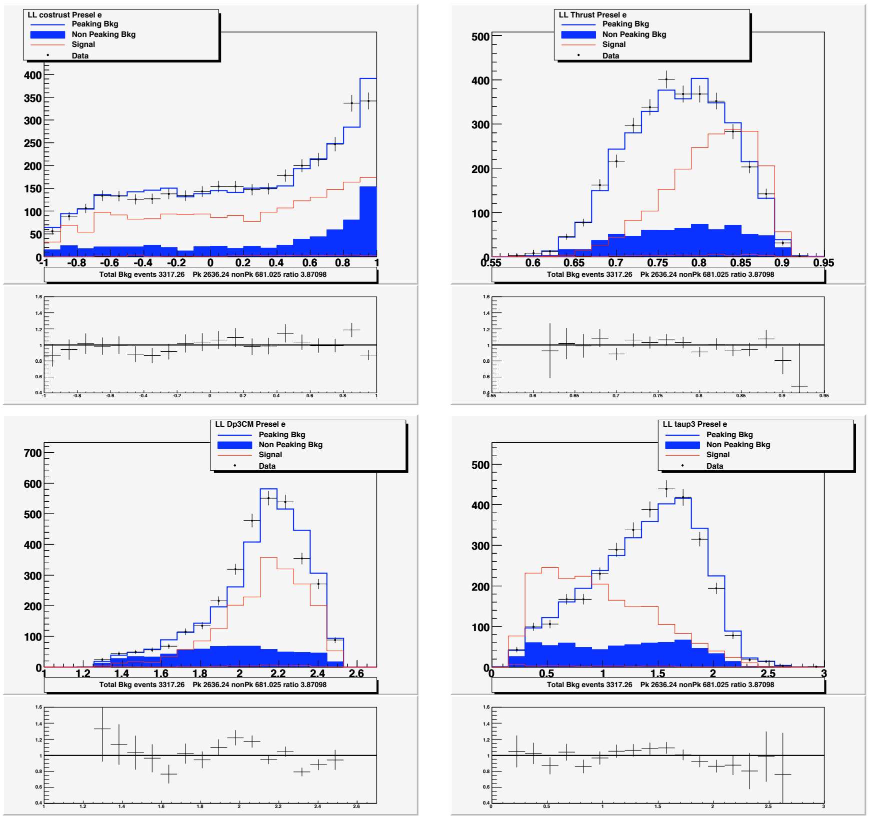

Figure 3.11: Data Monte Carlo agreement at preselection stage for electron channel. From top-left: $\cos\theta_T$, Thrust magnitude, p^*_D and electron momentum. The solid blue histogram is the non-peaking background; the white histogram is the peaking background, the points are data and the red histogram is the signal Monte Carlo in arbitrary scale; the lower red histogram is the crossfeed component of the signal. The plot at bottom of each histogram is the data/Monte Carlo ratio bin by bin.

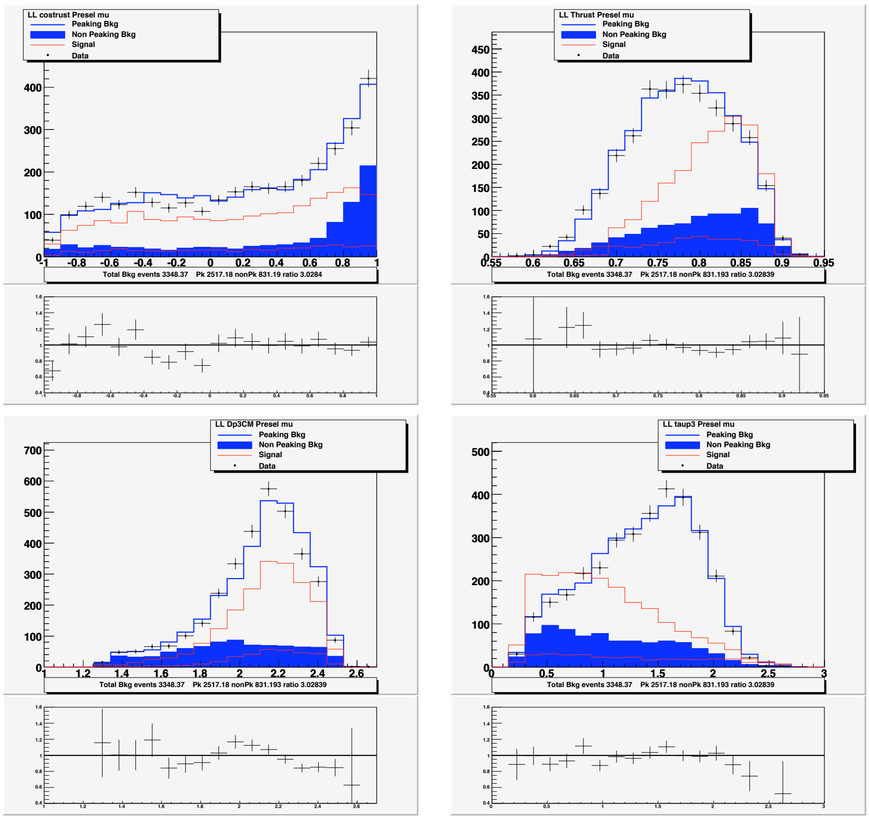

Figure 3.12: Data Monte Carlo agreement at preselection stage for muon channel. From top-left: $\cos\theta_T$, Thrust magnitude, p^*_D and muon momentum. The solid blue histogram is the non-peaking background; the white histogram is the peaking background, the points are data and the red histogram is the signal Monte Carlo in arbitrary scale; the lower red histogram is the crossfeed component of the signal. The plot at bottom of each histogram is the data/Monte Carlo ratio bin by bin.

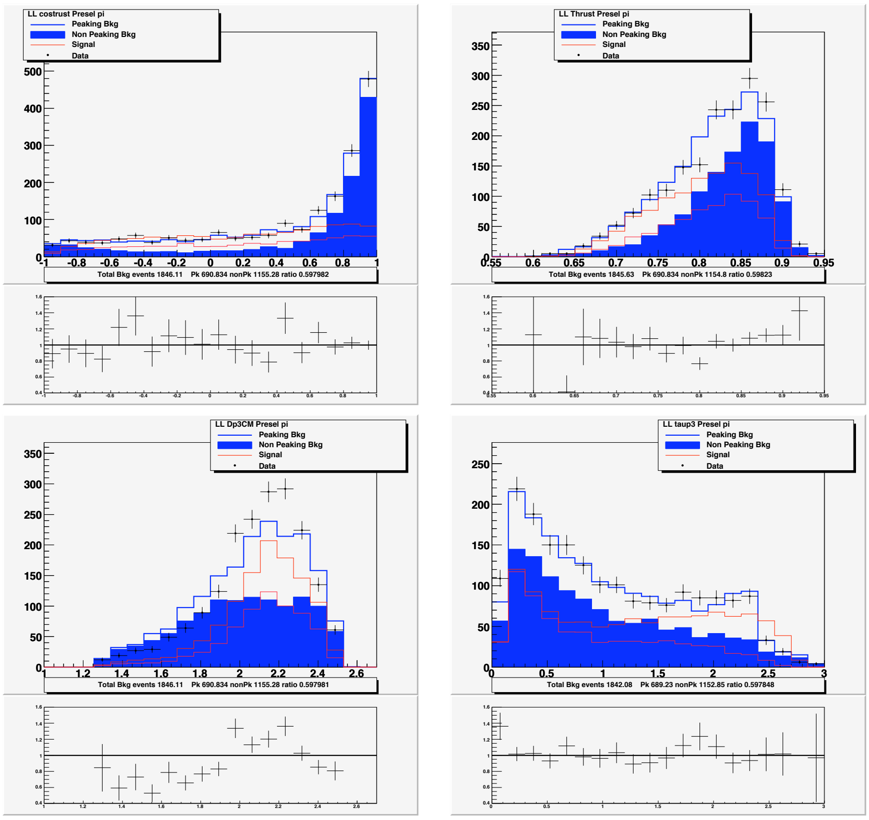

Figure 3.13: Data Monte Carlo agreement at preselection stage for pion channel. From top-left: $\cos\theta_T$, Thrust magnitude, p^*_D and pion momentum. The solid blue histogram is the non-peaking background; the white histogram is the peaking background, the points are data and the red histogram is the signal Monte Carlo in arbitrary scale; the lower red histogram is the crossfeed component of the signal. The plot at bottom of each histogram is the data/Monte Carlo ratio bin by bin.

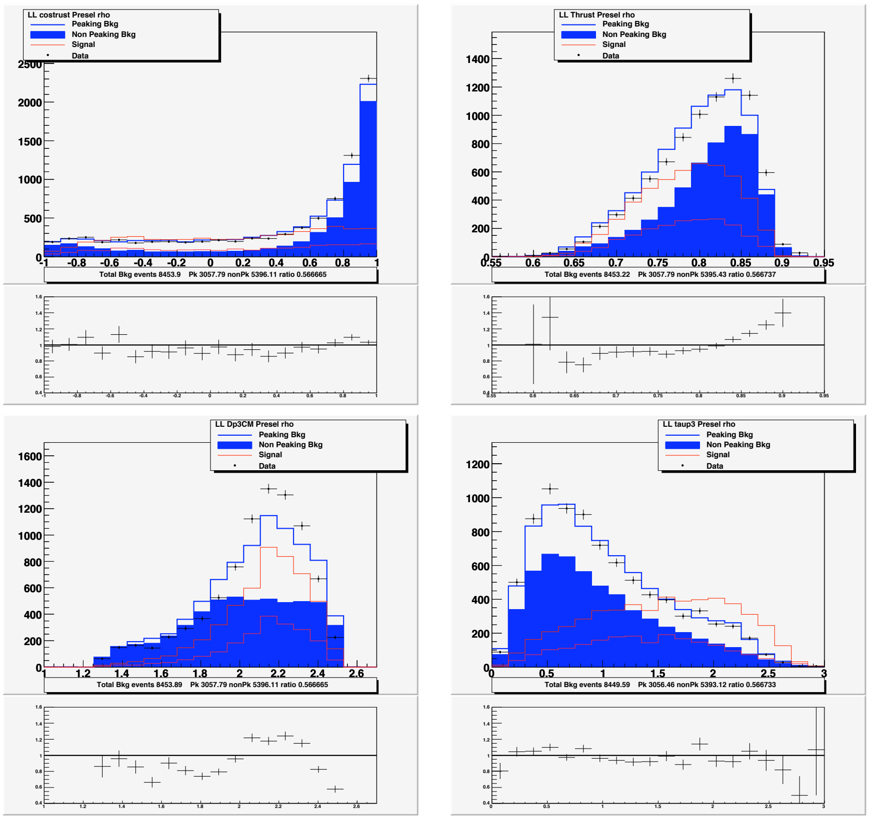

Figure 3.14: Data Monte Carlo agreement at preselection stage for rho channel. From top-left: $\cos\theta_T$, Thrust magnitude, p^*_D and rho momentum. The solid blue histogram is the non-peaking background; the white histogram is the peaking background, the points are data and the red histogram is the signal Monte Carlo in arbitrary scale; the lower red histogram is the crossfeed component of the signal. The plot at bottom of each histogram is the data/Monte Carlo ratio bin by bin.

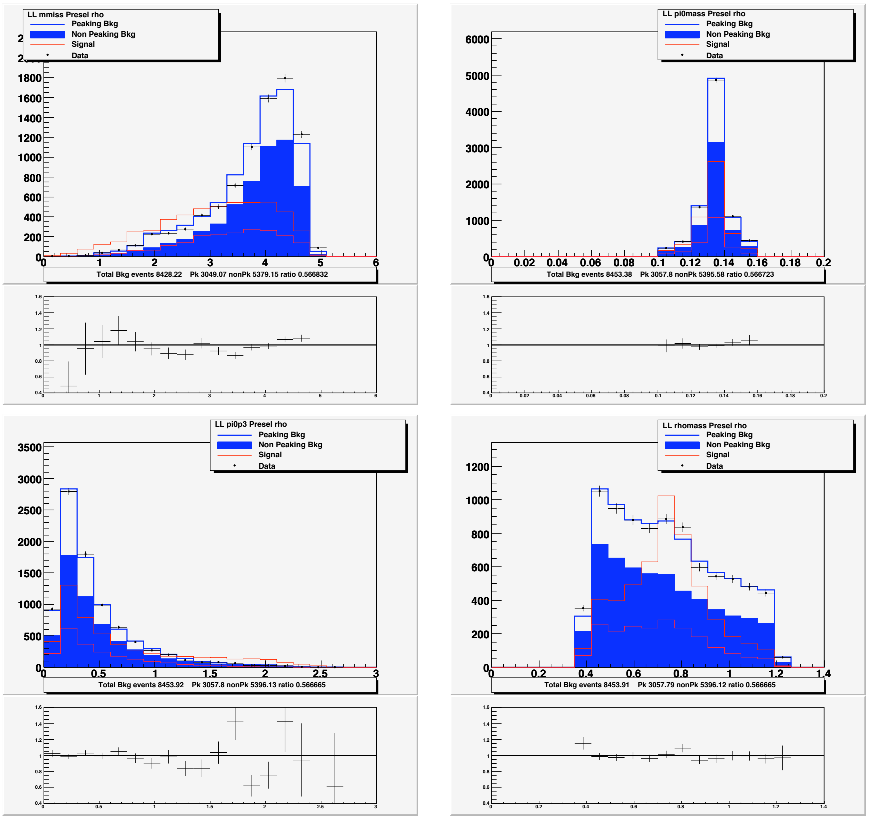

Figure 3.15: Data Monte Carlo agreement at preselection stage for rho channel. From top-left: event missing mass, π^0 from ρ mass, π^0 from ρ momentum in the center mass system and ρ mass. The solid blue histogram is the non-peaking background; the white histogram is the peaking background, the points are data and the red histogram is the signal Monte Carlo in arbitrary scale ; the lower red histogram is the crossfeed component of the signal. The plot at bottom of each histogram is the data/Monte Carlo ratio bin by bin.

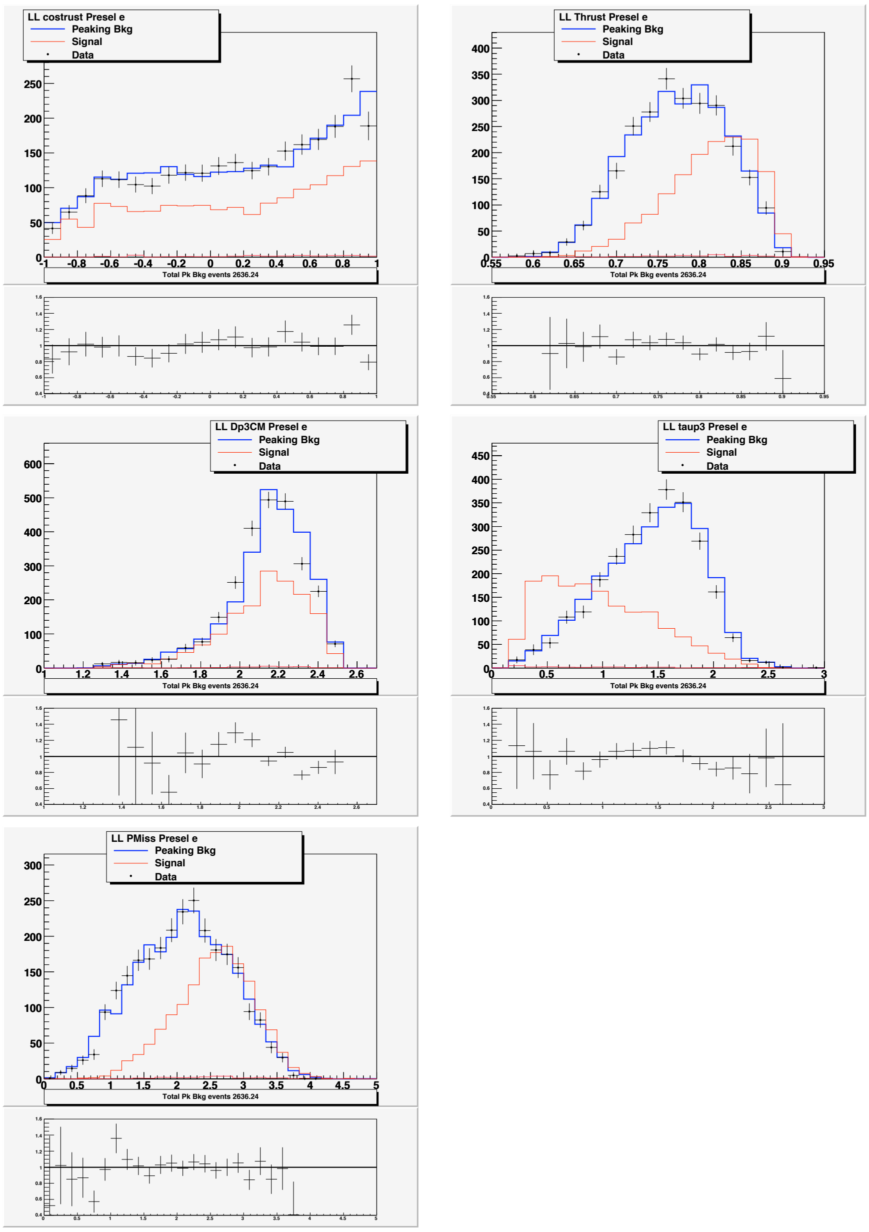

Figure 3.16: Data Monte Carlo agreement of peaking component at preselection stage for electron channel. From top-left: $\cos\theta_T$, Thrust magnitude, p^*_D, p^*_e and p_{Miss}. The white histogram is the peaking background, the points are data and the red histogram is the signal Monte Carlo in arbitrary scale; the lower red histogram is the crossfeed component of the signal. The plot at bottom of each histogram is the data/Monte Carlo ratio bin by bin.

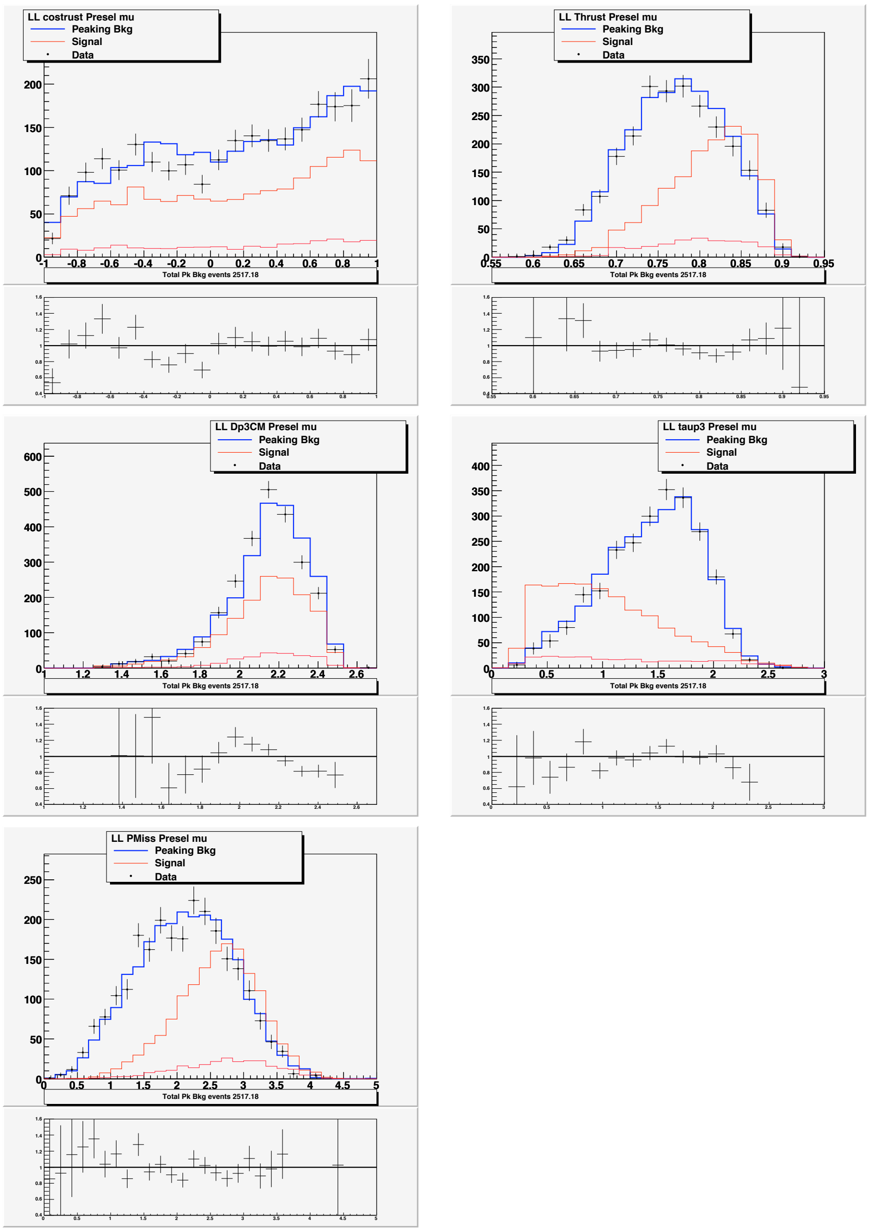

Figure 3.17: Data Monte Carlo agreement of peaking component at preselection stage for muon channel. From top-left: $\cos\theta_T$, Thrust magnitude, p^*_D, p^*_μ and p_{Miss}. The white histogram is the peaking background, the points are data and the red histogram is the signal Monte Carlo in arbitrary scale; the lower red histogram is the crossfeed component of the signal. The plot at bottom of each histogram is the data/Monte Carlo ratio bin by bin.

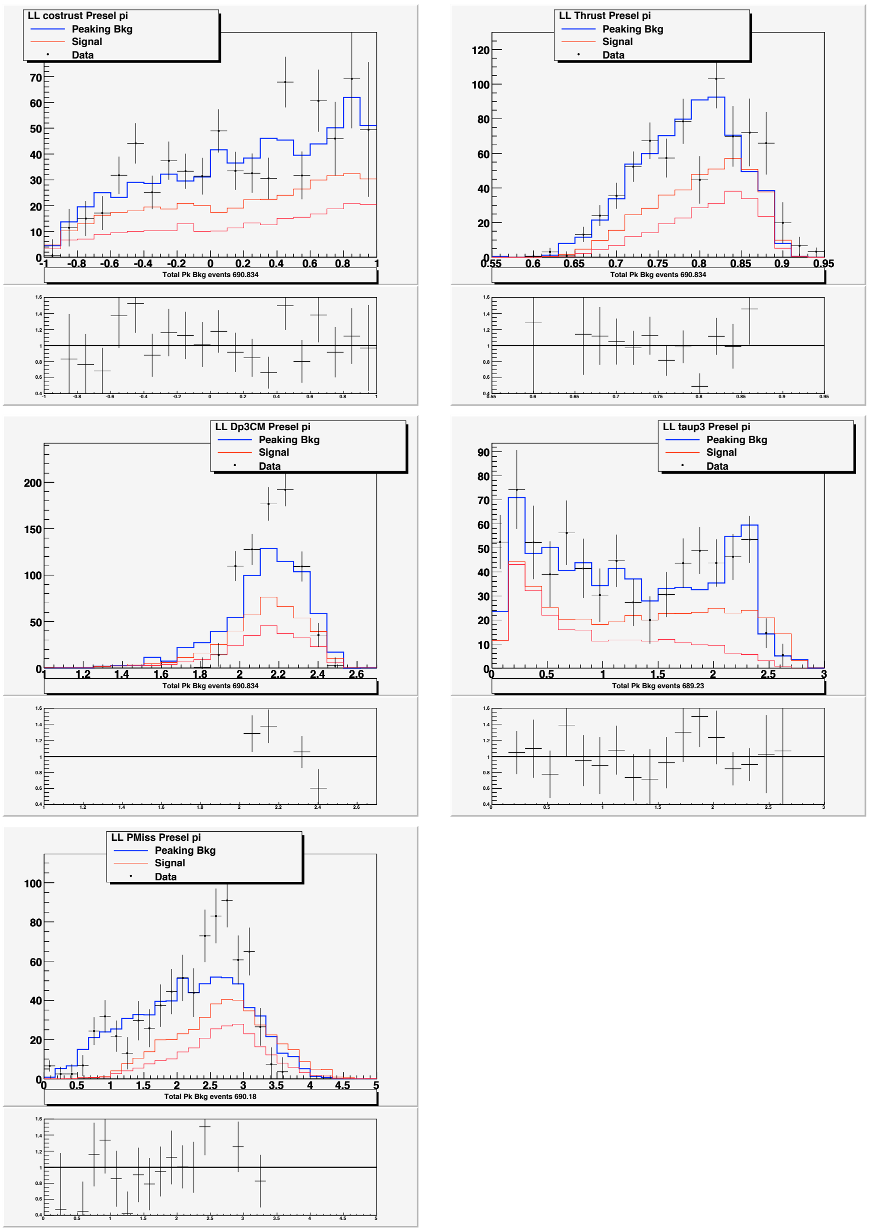

Figure 3.18: Data Monte Carlo agreement of peaking component at preselection stage for pion channel. From top-left: $\cos\theta_T$, Thrust magnitude, p^*_D, p^*_π and p_{Miss}. The white histogram is the peaking background, the points are data and the red histogram is the signal Monte Carlo in arbitrary scale; the lower red histogram is the crossfeed component of the signal. The plot at bottom of each histogram is the data/Monte Carlo ratio bin by bin.

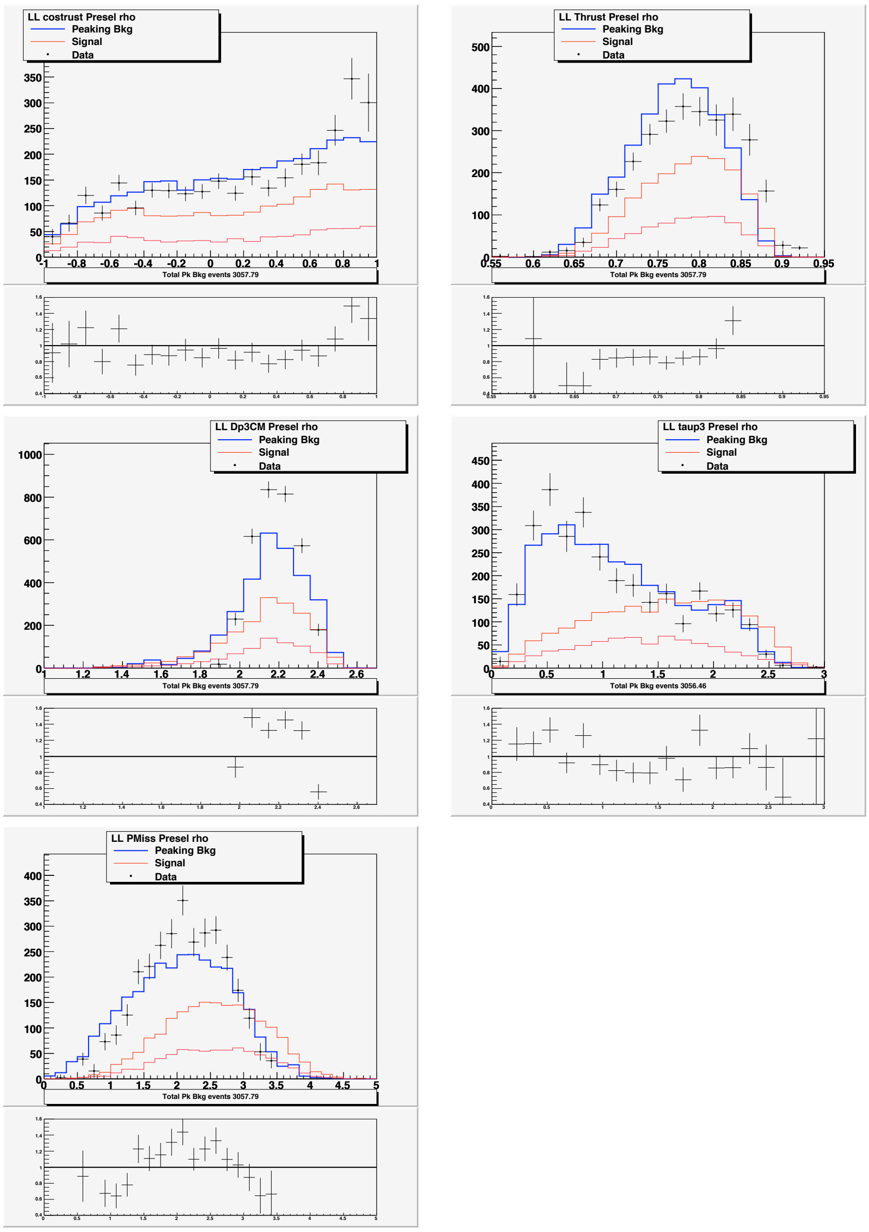

Figure 3.19: Data Monte Carlo agreement of peaking component at preselection stage for rho channel. From top-left: $\cos\theta_T$, Thrust magnitude, p^*_D, p^*_ρ and p_{Miss}. The white histogram is the peaking background, the points are data and the red histogram is the signal Monte Carlo in arbitrary scale; the lower red histogram is the crossfeed component of the signal. The plot at bottom of each histogram is the data/Monte Carlo ratio bin by bin.

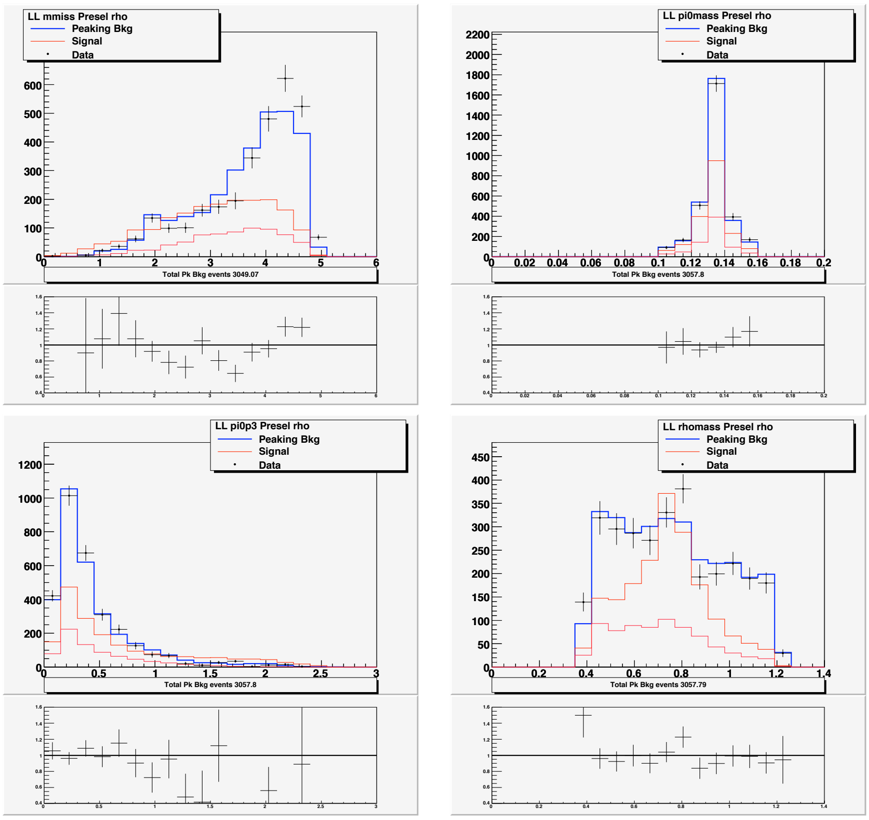

Figure 3.20: Data Monte Carlo agreement of peaking component at preselection stage for rho channel. From top-left: event missing mass, π^0 from ρ mass, π^0 from ρ momentum in the center mass system and ρ mass. The white histogram is the peaking background, the points are data and the red histogram is the signal Monte Carlo in arbitrary scale ; the lower red histogram is the crossfeed component of the signal. The plot at bottom of each histogram is the data/Monte Carlo ratio bin by bin.

3.5.1 Selection strategy and E_{extra} definition

We use two independent selectors to suppress the two background categories. We calculate a likelihood ratio based on B_{tag} reconstruction variables (L_C), with probabily density functions (PDF) from Monte Carlo simulation. By definition, if the observables discriminate signal and background and are not strongly correlated, the *Likelihood Ratio* distribution will peak toward 0 for "background" and toward 1 for "signal". In this case, "background" is combinatoric events, and "signal" is the peaking. We require a minimum value on this estimator to reject the non-peaking background. To reject the peaking background, we exploit the kinematics of the τ modes. For leptonic channels we require a maximum value on the charged track momentum in the center mass system. For $\tau^- \to \pi^- \nu$ channel we require a minimum value on the charged track momentum in the center mass system. For the $\tau^- \to \rho^- \nu$ channel we calculate another likelihood ratio (L_P) based on B_{sig} kinematics and topological quantities. To establish the level of tightness for the selection requirements we use an optimization procedure that will be described in sec. 4. This procedure is based on the E_{extra} variable, defined as:

$$E_{extra} = \sum_i E_i^{(n)} + \sum_j E_j^{(c)}, \tag{3.10}$$

where $E_i^{(n)}$ is the energy of the i-th calorimeter cluster and $E_j^{(c)}$ is the energy of the charged tracks, not assigned to any particle coming from B_{tag} or B_{sig}. The distribution of E_{extra} peaks at zero for $B \to \tau\nu$ signal events because we do not expect any neutral candidate or extra charged track, while it has an opposite behavior for the background. We can evaluate the number of signal and background events, and consequently the branching fraction, by fitting this distribution with a maximum likelihood fit. To fit a single mode E_{extra} distribution we use the background predictions and the signal Monte Carlo histograms as PDF. The likelihood function is so defined:

$$\mathcal{L} = \frac{e^{-N'}}{N'!} \prod_{i=1}^{N'} \left\{ N_S \mathcal{P}_i^S + N_C \mathcal{P}_i^C \right\} \tag{3.11}$$

where N' is the number of signal plus background events, N_S is the number of signal events and N_C is the number of background events, for the considered τ decay category. $\mathcal{P}_i^S$ and $\mathcal{P}_i^C$ are respectively the probability density functions of E_{extra} for signal and background. The background yield is left floating. The signal yield is related to the branching fraction as: $(\epsilon_i \cdot \epsilon_{corr}) \times N_{BB} \times \mathcal{B}$, where N_{BB} is the number of B pairs in the experimental data, ϵ_i is the efficiency to reconstruct the i-th τ decay mode, and ϵ_{corr} is the data/Monte Carlo correction to the tag efficiency described is sec. 3.3.2. ϵ_i is evaluated as $n_{sel,i}/n_{gen}$, where $n_{sel,i}$ is the number of signal events at the end of the selection for the i-th mode, evaluated in the signal Monte Carlo sample, and n_{gen} is the number of generated signal Monte Carlo events (22.905 × 10^6). We actually perform a simultaneous fit to the branching fraction.

Since we do not consider all the reconstructed calorimeter clusters in the calculation of E_{extra} , the PDFs for signal and background depend on the cluster to be included. We test different values for this threshold, from 30 MeV to 80 MeV, in steps of 10 MeV. The choice of the threshold to use in the final branching fraction extraction is part of the optimization procedure, aiming at the smallest statistical and systematic uncertainty (see sec. 4). We will use as notation $E_{extraXX}$ to refer at the E_{extra} quantity with a minimum cluster requirement of XX MeV. Fig. 3.21 shows the Data-Monte Carlo agreement of $E_{extra30}$ and $E_{extra60}$ for each channel; fig.3.22 shows the Data-Monte Carlo agreement of the peaking component for $E_{extra30}$ and $E_{extra60}$ variables.

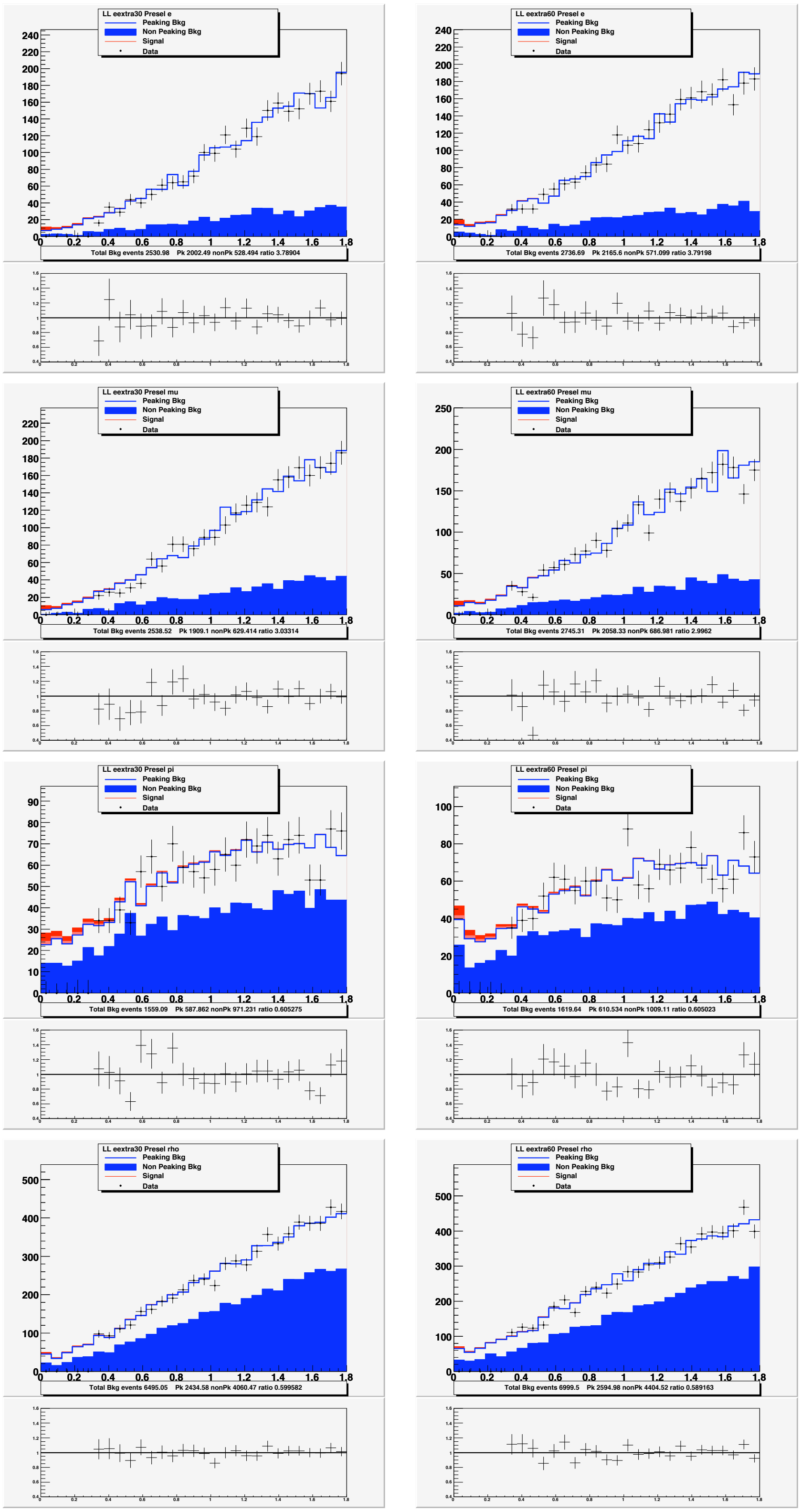

Figure 3.21: Data Monte Carlo agreement of the E_{extra} shapes for the 4 channel; rows are electron, moun, pion, rho; in the left column we show distribution of $E_{extra30}$ and in the right column we have $E_{extra60}$. The solid blue histogram is the non-peaking background; the white histogram is the peaking background, the points are data and the red histogram is the signal Monte Carlo with an imposed branching fraction of 1.4×10^{-4} (PDG workd aveage); the lighter red histogram is the crossfeed component of the signal. The first four bins of the data are blinded. The plot at bottom of each histogram is the data/Monte Carlo ratio bin by bin.

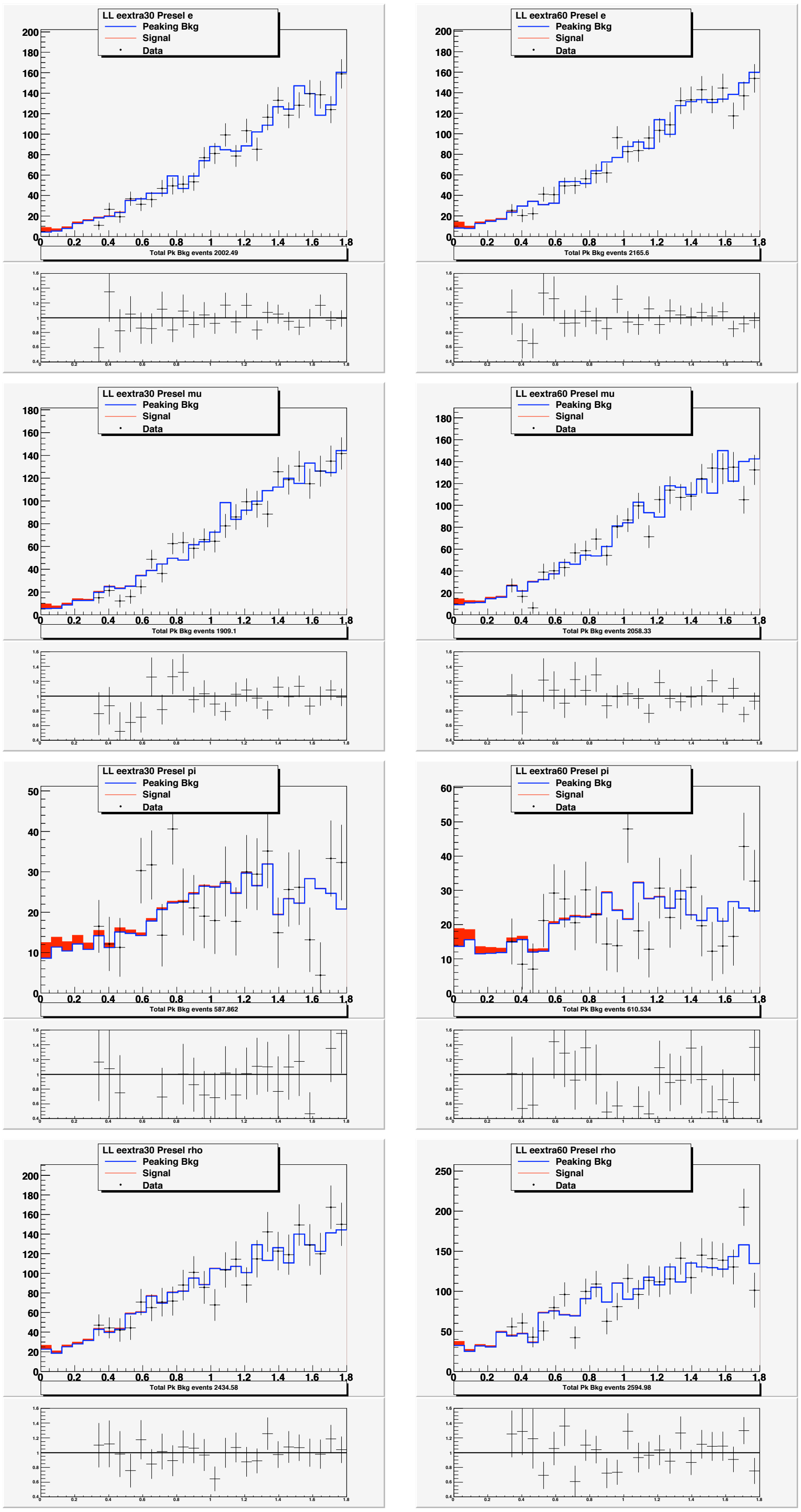

Figure 3.22: Data Monte Carlo agreement of the peaking component of E_{extra} shapes for the 4 channel; rows are electron, moun, pion, rho; in the left column we show distribution of $E_{extra30}$ and in the right column we have $E_{extra60}$. The solid blue histogram is the non-peaking background; the white histogram is the peaking background, the points are data and the red histogram is the signal Monte Carlo with an imposed branching fraction of 1.4×10^{-4} (PDG world average); the lower red histogram is the crossfeed component of the signal. The first four bins of the data are blinded. The plot at bottom of each histogram is the data/Monte Carlo ratio bin by bin.

3.5.2 Non-peaking background rejection

To reject the non-peaking background we calculate a likelihood ratio based on three variables related to the B_{tag}. The likelihood ratio is defined as:

$$L_C(x) = \frac{\mathcal{L}_S(x)}{\mathcal{L}_S(x) + \mathcal{L}_B(x)}, \tag{3.12}$$

where

$$\mathcal{L}_{S(B)}(x) = \prod_{k=1}^{n_{var}} p_{S(B),k}(x_k), \tag{3.13}$$

and where $p_{S(B),k}$ is the signal (background) PDF for the kth variable x_k. The PDFs are normalized as:

$$\int_{-\infty}^{+\infty} p_{S(B),k}(x_k) dx_k = 1, \quad \forall k. \tag{3.14}$$

We include the following discriminating variables:

- p^*_D: the three-momentum magnitude of the D (J/Ψ) particle reconstructed in B_{tag} decay chain, in the center mass system. Continuum events show lower values of p^*_D with respect to B^+B^- events.
- $\mathcal{T}$: the magnitude of the thrust vector of the B_{sig} defined as in Eq. 3.4
- $\cos(\theta_T)$: the angle between the thrust axis of the tag B and the thrust axis of the rest of the event.

To determine the PDF of the variables we use the *Monte Carlo Truth Matched* $B \rightarrow \tau\nu$ events in the m_{ES} *peaking region* for the signal and the m_{ES} *data sideband* for background. We consider only events with $E_{extra60} < 0.5\,\text{GeV}$. To avoid biases we consider only half of the selected samples, and we use the remaining half to evaluate performances. We use a *spline* [38] algorithm with a second order polynomial to smooth the histograms of the variables for the $\cos(\theta_T)$; we apply the smooth procedure four times to avoid structures in the PDF. For the other two variables, we realized that a polynomial cannot solve the peak of the distribution in a satisfactory way, so we use the unbinned kernel density estimators (KDE) algorithm[38]. The PDFs of signal and background for all channels are reported in fig 3.23, 3.24, 3.25 and 3.26. In fig. 3.27 we report the distributions of the L_C for the four τ decay channels, identifying the combinatorial background component, the peaking backround, data and signal Monte Carlo distribution.

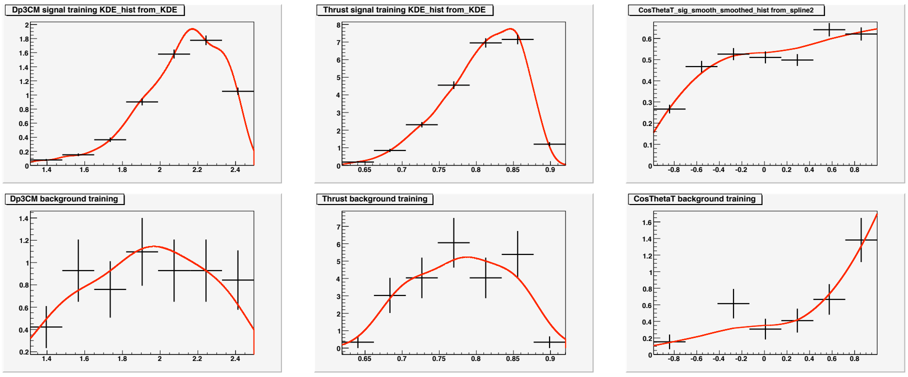

Figure 3.23: Signal and background PDFs used for the *C-Likelihood*; electron channel. Dots represent the distributions, while the red line is the PDF shape obtained by smoothing algorythm. The left column is the D center mass momentum, the middle column is the Thrust magnitude and the bottom column is the $\cos\theta_T$. Top row is for signal and bottom row for the background.

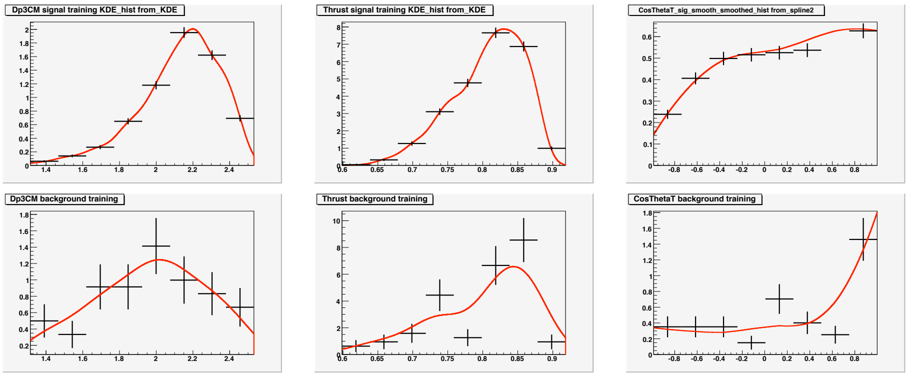

Figure 3.24: Signal and background PDFs used for the *C-Likelihood*; muon channel. Dots represent the distributions, while the red line is the PDF shape obtained by smoothing algorythm. The left column is the D center mass momentum, the middle column is the Thrust magnitude and the bottom column is the $\cos\theta_T$. Top row is for signal and bottom row for the background.

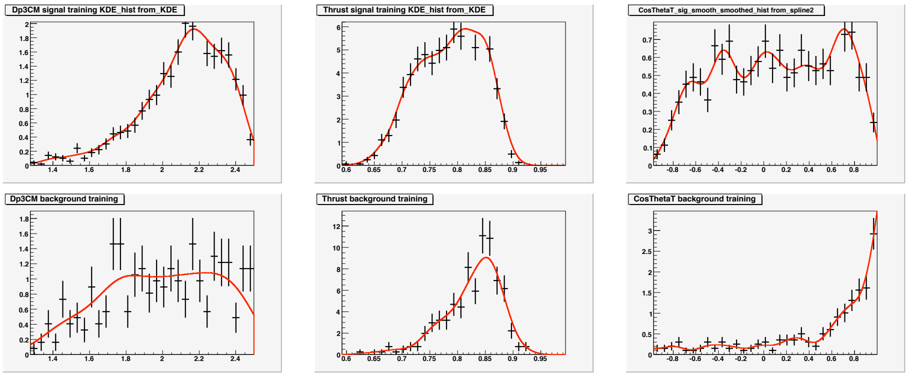

Figure 3.25: Signal and background PDFs used for the *C-Likelihood*; pion channel. Dots represent the distributions, while the red line is the PDF shape obtained by smoothing algorythm. The left column is the D center mass momentum, the middle column is the Thrust magnitude and the bottom column is the $\cos\theta_T$. Top row is for signal and bottom row for the background.

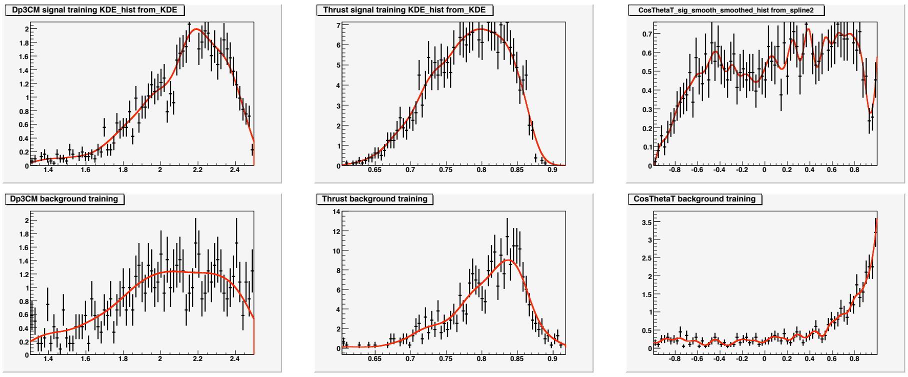

Figure 3.26: Signal and background PDFs used for the *C-Likelihood*; rho channel. Dots represent the distributions, while the red line is the PDF shape obtained by smoothing algorythm. The left column is the D center mass momentum, the middle column is the Thrust magnitude and the bottom column is the $\cos\theta_T$. Top row is for signal and bottom row for the background.

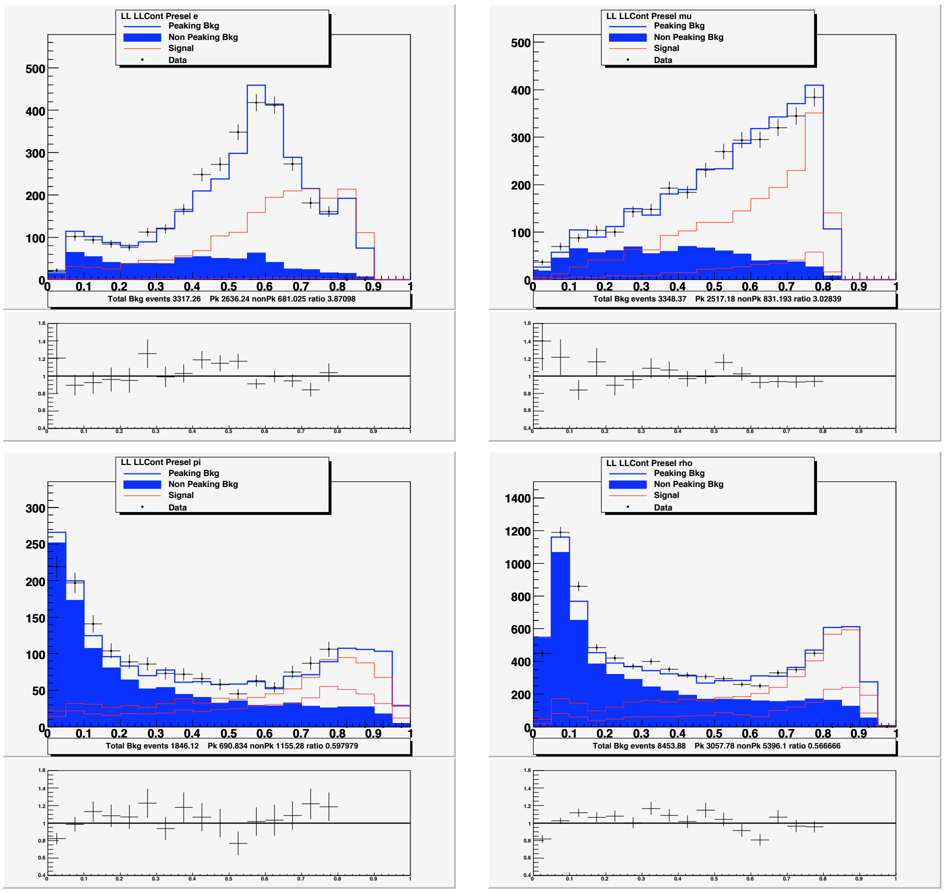

Figure 3.27: Distributions and data/Monte Carlo agreement for the L_C variable, for electron channel (top-left), muon (top-right), pion (bottom-left) and rho (bottom-right). The solid blue component is the non-peaking background, the white histogram is the peaking background, the points are data and the red histogram is the signal Monte Carlo in arbitrary scale ; the lower red histogram is the crossfeed component of the signal. The plot at bottom of each histogram is the data/Monte Carlo ratio bin by bin.

3.5.3 Peaking background rejection

The signal charged track momentum in the center mass system is the second most discriminating variable after E_{extra} for the peaking background with respect to $B \rightarrow \tau\nu$ events. Since leptonic τ modes are 3 body decays they present a lower momentum in average, so we require $p_l^* < p_{max}$, p_{max} to be determined by an optimization of selection criteria. Since $\tau^- \rightarrow \pi^-\nu$ is a 2 body decay, π momentum is higher in $B \rightarrow \tau\nu$ events with respect to the background and we require $p_\pi^* > p_{min}$. In the ρ channel, we reconstruct an additional particle in the final state (π^0), so we consider additional discriminating variables, and calculate a likelihood ratio, (L_P). the L_C case(sec. 3.5.2). We use four variables to compute the *likelihood ratio*:

- p_ρ^*: the three-momentum magnitude of the reconstructed ρ particle in the center mass system.
- m_{Miss}: the missing mass of the event defined as

  $$m_{Miss}^2 = E_{Miss}^2 - p_{All}^2 \tag{3.15}$$

  where $E_{Miss} = E_{\Upsilon(4S)} - (E_{B_{\text{tag}}}) - (E_{B_{\text{sig}}})$ and $p_{All} = p_{B_{\text{sig}}} + p_{B_{\text{tag}}}$. The quantity $p_{B_{\text{sig}}(B_{\text{tag}})}$ and $E_{B_{\text{sig}}(B_{\text{tag}})}$ are respectively the sum of the momenta and the energies of all the reconstructed particles coming from the B_{sig} (B_{tag})
- $p_{\pi^0}^*$: the momentum of the π^0 in the center mass system
- m_ρ: the mass of the reconstructed ρ.

The distribution of the above quantities at preselection level are shown in fig.3.14 and 3.15. To determine the PDFs of the variables we use the *Monte Carlo Truth Matched* $B \rightarrow \tau\nu$ events in the m_{ES} *peaking region* for the signal. We use the B^+B^- Monte Carlo for the background PDFs; to reject the non-peaking component of this background we look at the *Monte Carlo Truth* informations, requiring:

- all the charged tracks associated to the B_{tag} come from the same generated B
- one of the angles between the reconstructed B_{tag} and the two generated B $\alpha <$ 0.2 rad.

As in the previous case, we consider only events with $E_{extra60} < 0.5$ GeV in the m_{ES} peaking region and use half of the selected samples for the PDFs and the other half for the rest of the analysis. Also in this case we use a *spline* [38] algorithm with a second order polynomial to smooth the histograms of the variables for the $p_{\pi^0}^*$, where the distribution does not show a peak. For the other two variables we use the unbinned kernel density estimators (KDE) algorithm[38], better suited when the distribution shows a legal peak. The PDF for signal and background are shown in fig. 3.28, while in fig.3.29 we show the distribution of L_P at preselection level.

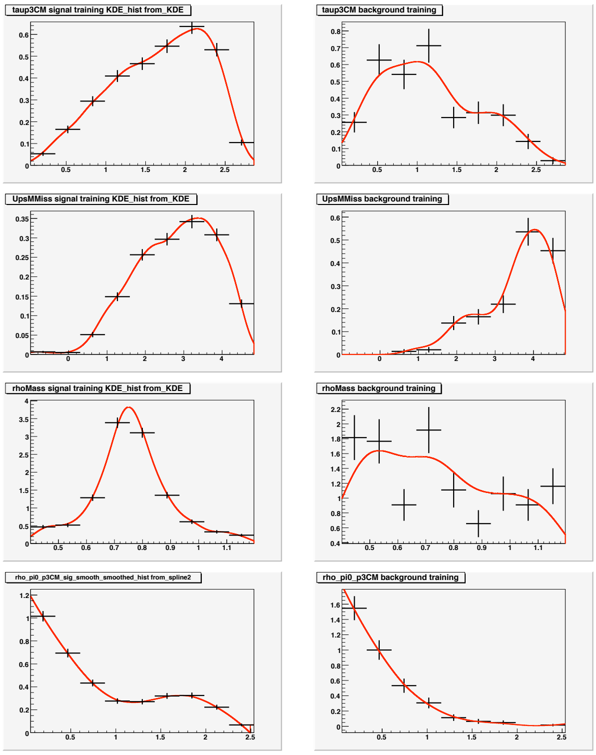

Figure 3.28: Signal and background PDFs used for the *P-Likelihood*; rho channel. Dots represent the distributions, while the red line is the PDF shape obtained by smoothing algorythm. The first row is the ρ momentum in the center mass system, the second row is the event missing mass, the third row is the ρ mass and the last row is the center mass system momentum of the π^0 used to build the ρ candidate. Left column is for signal and right column for the background.

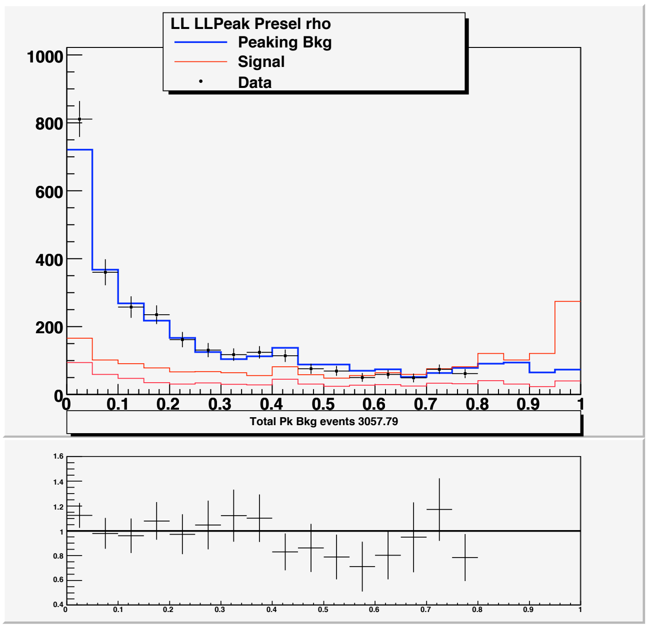

Figure 3.29: Data Monte Carlo agreement at preselection stage of the L_P variable for rho channel, with the combinatoric part subtracted. The white histogram is the peaking background, the points are data and the red histogram is the signal Monte Carlo in arbitrary scale; the lower red histogram is the crossfeed component of the signal. The plot at bottom of each histogram is the data/Monte Carlo ratio bin by bin. Last bins are blinded for data.

Chapter 4

Selection optimization

In this chapter we present the optimization of the signal selection requirements. It is based on toy-Monte Carlo experiments to estimate the statistical and systematic uncertainties, the optimal selectors being the set of requirements that minimize the expected total uncertainties. The largest contributions to the systematics come from background expectation and signal events behavior. In both cases the source of the systematic uncertainty is the shape of E_{extra} that are left fixed in the likelihood fit of the signal yields, and hence the branching fraction.

4.1 Selection optimization

We apply selection requirements on L_C and track momentum (or L_P for the ρ channel) to select the sample to fit in $B \to \tau\nu$ branching fraction. We define a two-dimensional grid of selection cuts based on the two selectors, and for each point of the grid the selected events will be distributed in E_{extra} differently. We use the histograms as templates to generate 1000 toy E_{extra} distributions of signal plus background. The background yield is fixed by data sideband for the non peaking component and Data/Monte Carlo yields ratio for the peaking component. The amount of (expected) signal is fixed by a branching fraction hypothesis of 1.4×10^{-4}(PDG world average [16]). The PDFs used in the fit are the normalized histograms of E_{extra} for each component. We obtain for each point of the grid a distribution of fitted branching fractions and a distribution of uncertainty on the branching fraction. We fit those distribution with a gaussian function. The branching fraction distribution, in absence of bias, peaks at 1.4×10^{-4}, as expected. We set the optimal selection requirements to the ones that minimize the meaurement uncertainty as estimated by means of the toy experiments. In this procedure we use 60 MeV as minimum energy for a cluster. A lower value for the cluster threshold results in a better separation of signal and background in E_{extra} shapes and to a smaller uncertainty on the branching fraction. We assume that the effects of the minimum cluster energy choice are independent from the selection requirements.
We proceed in the optimization in the following way:

- we define a fixed number of possible cuts for each selection variable, depending on the variable distribution at preselection level. We obtain a two-dimensional grid of possible selection requirements for each channel

- we calculate the uncertainty on the branching fraction for each point of the grid and select a sub-region of the grid where the uncertainties are smaller. Table 4.1 shows the mode dependent optimal sub-regions. Figures 4.1-4.4 show the selection requirements grid for each channel.

channel	$L_{C,min}$ range	$p^*_{l,max}$ range	$p^*_{\pi,max}$ range	$L_{P,min}$ range
$\tau^- \to e^- \nu\bar{\nu}$	0-0.6	1.4-2.9 GeV		
$\tau^- \to \mu^- \nu\bar{\nu}$	0-0.4	1.5-2.9 GeV		
$\tau^- \to \pi^- \nu$	0.1-0.7		0.1-0.7 GeV	
$\tau^- \to \rho^- \nu$	0.20-0.40			0.7-0.8

Table 4.1: Ranges of selection requirements regions where we observe the minimum expected uncertainty on the branching fraction extraction.

- we apply the toy-fitting procedure to the leptonic channels simultaneously, exploring all the possible combinations of selection requirements from the two sub-regions of the grids. We fix the optimal selection level for the leptonic channels as the combination of requirements that gives the smallest uncertainty. In table 4.2 we report the optimal selection level we set for the leptonic channels

Channel	L_C min.	p^*_l max	BF
e	0	1.6	1.47 ± 0.88
μ	0.3	1.9 GeV	1.39 ± 0.87
combined			1.39 ± 0.61

Table 4.2: Optimized selection requirement for electron and muon channel, and average uncertainty of the branching fraction assuming 1.4×10^{-4}, for channel independent mode and for the combined mode.

- keeping fixed the selection requirements for the leptonic channels at the optimal ones, we apply the procedure to the four channels simultaneously. We explore all the combinations of the two grid sub-regions for the hadronic channels, and fix their optimal selection levels to the ones with the lowest uncertainty. In tab. 4.3 we report the optimal selection level we set for pion and rho channels and the final result we obtain using all channels:

Channel	L_C min.	$p^*_{pi}/L_{P\ \rho}$ min.	BF
π	0.5	1.3 GeV	1.44 ± 1.10
ρ	0.2	0.7	1.37 ± 1.23
Combined (e and μ included)			1.38 ± 0.49

Table 4.3: Optimized selection requirement for pion and rho channel, and average uncertainty of the branching fraction assuming 1.4×10^{-4}, for channel independent modes and combined mode, including leptonic channels at optimized selection level.

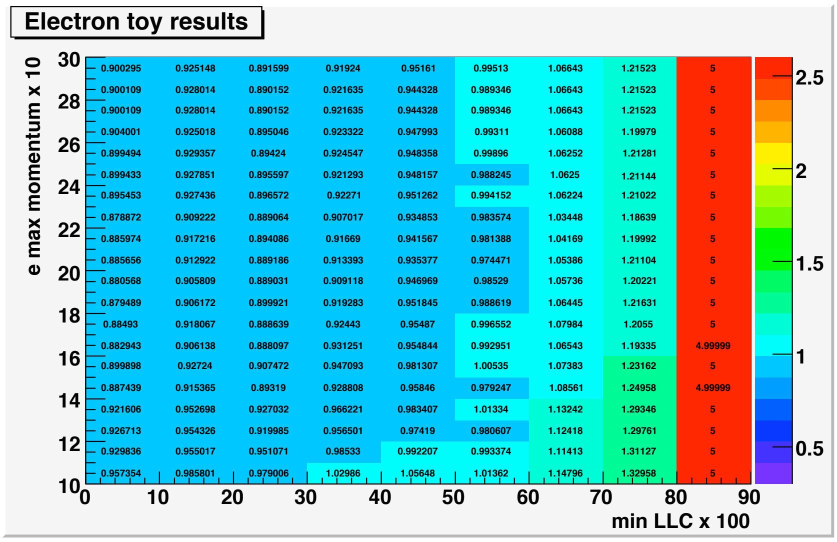

Figure 4.1: Prospect of fitted average uncertainty for each selection level in the electron channel. 1000 toys are created for each point of the $L_{C\ min} \times p^*_{e,max}$ grid.

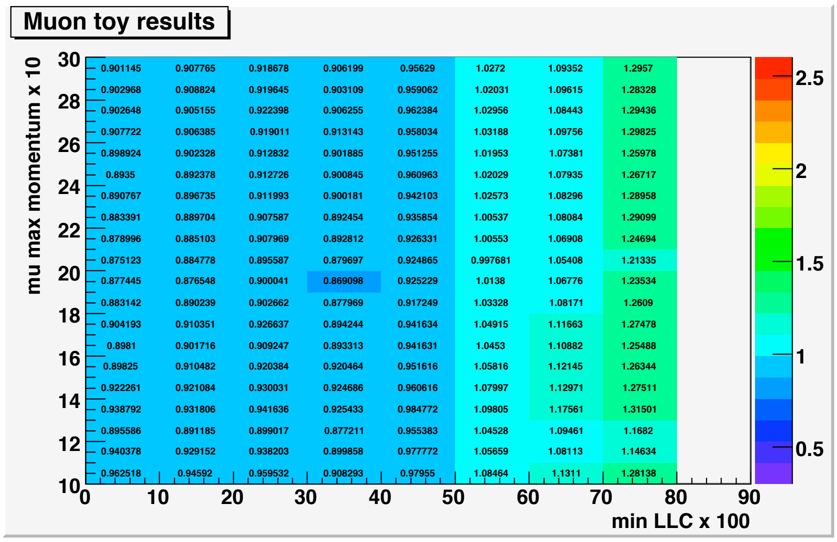

Figure 4.2: Prospect of average uncertainty for each selection level in the muon channel. 1000 toys are created for each point of the $L_{C\ min} \times p^*_{e,max}$ grid.

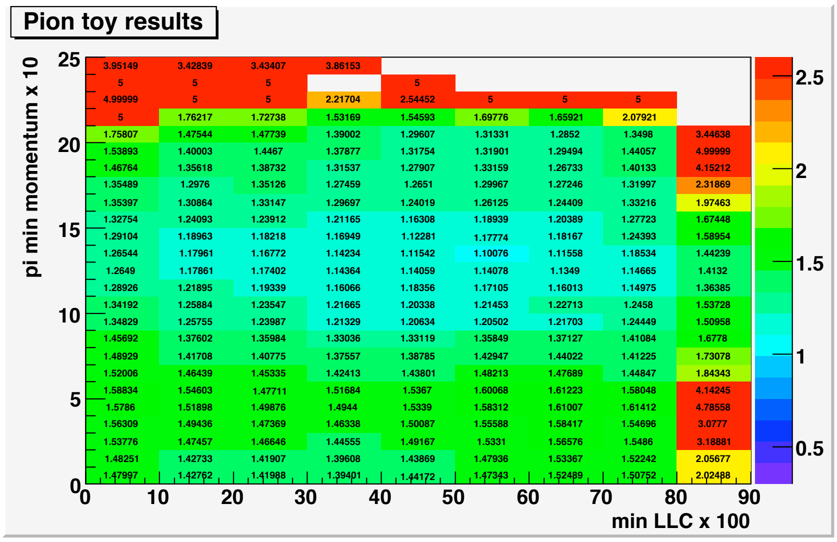

3.95149	3.42839	3.43407	3.86153					
5	5	5		5				
4.99999	5	5	2.21704	2.54452	5	5	5	
5	1.76217	1.72738	1.53169	1.54593	1.69776	1.65921	2.07921	
1.75807	1.47544	1.47739	1.39002	1.29607	1.31331	1.2852	1.3498	3.44638
1.53893	1.40003	1.4467	1.37877	1.31754	1.31901	1.29494	1.44057	4.99999
1.46764	1.35618	1.38732	1.31537	1.27907	1.33159	1.26733	1.40133	4.15212
1.35489	1.2976	1.35126	1.27459	1.2651	1.29967	1.27246	1.31997	2.31869
1.35397	1.30864	1.33147	1.29697	1.24019	1.26125	1.24409	1.33216	1.97463
1.32754	1.24093	1.23912	1.21165	1.16308	1.18939	1.20389	1.27723	1.67448
1.29104	1.18963	1.18218	1.16949	1.12281	1.17774	1.18167	1.24393	1.58954
1.26544	1.17961	1.16772	1.14234	1.11542	1.10076	1.11558	1.18534	1.44239
1.2649	1.17861	1.17402	1.14364	1.14059	1.14078	1.1349	1.14665	1.4132
1.28926	1.21895	1.19339	1.16066	1.18356	1.17105	1.16013	1.14975	1.36385
1.34192	1.25884	1.23547	1.21665	1.20338	1.21453	1.22713	1.2458	1.53728
1.34829	1.25755	1.23987	1.21329	1.20634	1.20502	1.21703	1.24449	1.50958
1.45692	1.37602	1.35984	1.33036	1.33119	1.35849	1.37127	1.41084	1.6778
1.48929	1.41708	1.40775	1.37557	1.38785	1.42947	1.44022	1.41225	1.73078
1.52006	1.46439	1.45335	1.42413	1.43801	1.48213	1.47689	1.44847	1.84343
1.58834	1.54603	1.47711	1.51684	1.5367	1.60068	1.61223	1.58048	4.14245
1.5786	1.51898	1.49876	1.4944	1.5339	1.58312	1.61007	1.61412	4.78558
1.56309	1.49436	1.47369	1.46338	1.50087	1.55588	1.58417	1.54696	3.0777
1.53776	1.47457	1.46646	1.44555	1.49167	1.5331	1.56576	1.5486	3.18881
1.48251	1.42733	1.41907	1.39608	1.43869	1.47936	1.53367	1.52242	2.05677
1.47997	1.42762	1.41988	1.39401	1.44172	1.47343	1.52489	1.50752	2.02488

Figure 4.3: Prospect of average uncertainty for each selection level in the pion channel. 1000 toys are created for each point of the $L_{C\ min} \times p^*_{\pi,min}$ grid.

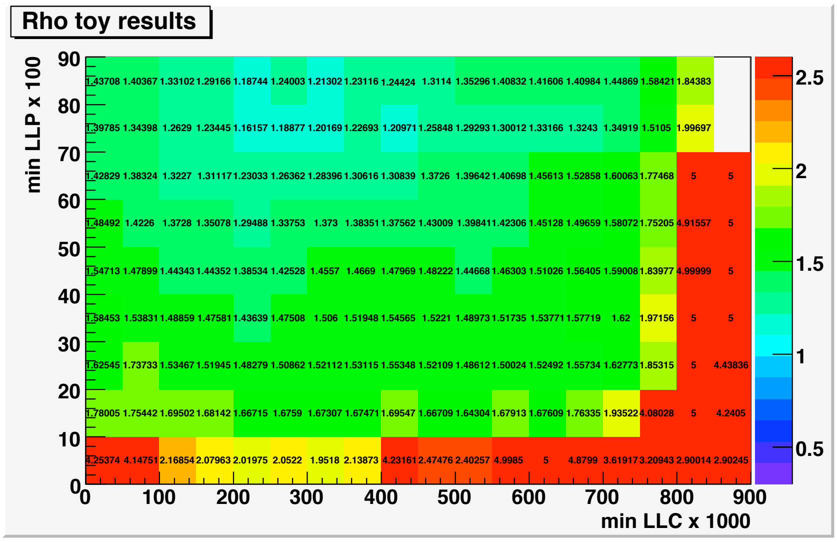

1.43708	1.40367	1.33102	1.29166	1.18744	1.24003	1.21302	1.23116	1.24424	1.3114	1.35296	1.40832	1.41606	1.40984	1.44869	1.58421	1.84383	
1.39785	1.34398	1.2629	1.23445	1.16157	1.18877	1.20169	1.22693	1.20971	1.25848	1.29293	1.30012	1.33166	1.3243	1.34919	1.5105	1.99697	
1.42829	1.38324	1.3227	1.31117	1.23033	1.26362	1.28396	1.30616	1.30839	1.3726	1.39642	1.40698	1.45613	1.52858	1.60063	1.77468	5	5
1.48492	1.4226	1.3728	1.35078	1.29488	1.33753	1.373	1.38351	1.37562	1.43009	1.39841	1.42306	1.45128	1.49659	1.58072	1.75205	4.91557	5
1.54713	1.47899	1.44343	1.44352	1.38534	1.42528	1.4557	1.4669	1.47969	1.48222	1.44668	1.46303	1.51026	1.56405	1.59008	1.83977	4.99999	5
1.58453	1.53831	1.48859	1.47581	1.43639	1.47508	1.506	1.51948	1.54565	1.5221	1.48973	1.51735	1.53771	1.57719	1.62	1.97156	5	5
1.62545	1.73733	1.53467	1.51945	1.48279	1.50862	1.52112	1.53115	1.55348	1.52109	1.48612	1.50024	1.52492	1.55734	1.62773	1.85315	5	4.43836
1.78005	1.75442	1.69502	1.68142	1.66715	1.6759	1.67307	1.67471	1.69547	1.66709	1.64304	1.67913	1.67609	1.76335	1.93522	4.08028	5	4.2405
4.25374	4.14751	2.16854	2.07963	2.01975	2.0522	1.9518	2.13873	4.23161	2.47476	2.40257	4.9985	5	4.8799	3.61917	3.20943	2.90014	2.90245

Figure 4.4: Prospect of average uncertainty for each selection level in the rho channel. 1000 toys are created for each point of the $L_{C\ min} \times L_P$ grid.

4.2 Different purity requirement optimization

We repeat the same selection procedure varying the minimum purity requirement. In particular we analyze the following requirements: 5%, 7.5%, 10%, 12.5% and 15%. In table 4.4 we show the result of the optimization at different purities. At higher purity corresponds a smaller background amount, which helps to better sensitivity, but a decrease in statistics that on the contrary spoils the statistical power.

Min. pur. req. (%)	0%	5%	7.5%
e: minL_C -maxp^*_e	0.5-1.5	0.2-1.6	0.1-1.9
μ: minL_C -maxp^*_μ	0.5-2.4	0.2-2.5	no cut-1.6
π: minL_C -minp^*_π	0.6-1.4	0.6-1.8	0.4-1.2
ρ: minL_C -minL_P	0.75-0.7	0.65-0.7	0.55-0.7
BF extraction	1.35±0.57	1.37±0.55	1.40±0.52

Min. pur. req. (%)	10%	12.5%	15%
e: minL_C -maxp^*_e	0.2-2.2	no cut-1.6	0.2-2.3
μ: minL_C -maxp^*_μ	0.1-1.9	0.3-1.8	0.1-2.4
π: minL_C -minp^*_π	0.5-1.3	0.5-1.3	0.4-1.5
ρ: minL_C -minL_P	0.45-0.8	0.2-0.7	0.5-0.7
BF extraction	1.39±0.49	1.38±0.49	1.39±0.55

Table 4.4: Results of the optimization at different purity values with the expected statistical uncertainty on the branching fraction extraction. The value of the branching fraction imposed in the toy generation is 1.4×10^{-4}.

4.3 E_{extra} signal shape corrections and systematics prediction

Using as signal PDF the E_{extra} shapes taken form signal Monte Carlo, one assumes a perfect data/Monte Carlo agreement, expecially for the reconstruction of low-energy clusters in the EMC. It is possible to take into account data/Monte Carlo differences using a data control sample and milder assumptions.

We assume that the Data/Monte Carlo differences are the same for signal events and double tagged events, so we do a bin-by-bin comparison of the E_{extra} shape for Data and Monte Carlo in the latter sample. There is one more degree of freedom: the choice of the minimum cluster energy. Since the agreement is better for higher minimum cluster energies, the inclusion of clusters with lower and lower energy deteriorates the agreement. On the other hand it is useful to include lower energy clusters because this improves the separation between signal and backround events. We use the “Hybrid” double tag to correct the leptonic channels, while we use the “Hadronic” double tag sample to correct the hadronic channel π and ρ. In fig. 4.5 we show the bin-by-bin correction plots for the E_{extra} shapes at different values of minimum energy cluster. Note that we correct only the Monte Carlo shape of E_{extra} , while the amount of signal (the integral of the distribution) is kept fixed. We perform the same toy Monte Carlo procedure described in section 4, generating 1000 toy experiments using the modifyed shapes in two ways:

- using the new shapes both for generating the toy events and for fitting the branching fraction to determine the expected statistical uncertainty in data
- using the new shapes for generating toys, but nominal shapes for fitting, to estimate the systematic uncertainties due to the data/Monte Carlo differences in the E_{extra} shape. This is a conservative estimation of the systematic uncertainty because we correct the systematic effect but we are taking 100% of the effect as systematic uncertainty.

We repeat the techinque for an ample interval of possible thresholds of cluster energy, obtaining a set of average extracted branching fraction. For each choice we expect to fit a branching fraction different from the one used to generate the toy experiment (1.4×10^{-4}). In table 4.5 we show the results of this procedure for the different analyzed purity requirements and cluster energy thresholds. We report the results of the toy-fit procedure with the two described methods and the difference of the two branching fractions; we report also the sum in quadrature of the statistical and systematic uncertainty. From the results we see that for each selection level the statistical uncertainty slightly increases increasing the cluster threshold, while the systematic uncertainty is generally higher for lower cluster energy values, as expected. The total uncertainty (sum in quadrature of statistical and systematic uncertainty) is minimum at 30 MeV and 60 MeV minimum cluster energy in almost all cases. We consider only those two values in the rest of the optimization procedures;

Purity / cluster min	BF (gen corr, fit corr)	BF (gen corr, fit nominal)	Syst error	Global error
0% / 30	1.37±0.59	1.24±0.54	0.16	0.616
0% / 40	1.40±0.58	1.23±0.55	0.17	0.601
0% / 50	1.38±0.61	1.21±0.55	0.19	0.636
0% / 60	1.38±0.60	1.28±0.56	0.12	0.617
0% / 70	1.41±0.63	1.28±0.58	0.12	0.643
0% / 80	1.36±0.65	1.26±0.60	0.14	0.664
5% / 30	1.36±0.57	1.24±0.52	0.16	0.595
5% / 40	1.38±0.59	1.22±0.53	0.18	0.621
5% / 50	1.40±0.55	1.23±0.53	0.17	0.570
5% / 60	1.39±0.59	1.29±0.55	0.11	0.601
5% / 70	1.36±0.61	1.24±0.56	0.16	0.635
5% / 80	1.40±0.63	1.30±0.58	0.10	0.636
7.5% / 30	1.39±0.55	1.26±0.50	0.14	0.570
7.5% / 40	1.40±0.57	1.24±0.51	0.16	0.593
7.5% / 50	1.38±0.56	1.22±0.50	0.18	0.593
7.5% / 60	1.42±0.55	1.33±0.52	0.07	0.557
7.5% / 70	1.37±0.57	1.24±0.52	0.16	0.594
7.5% / 80	1.38±0.59	1.28±0.54	0.12	0.600
10% / 30	1.40±0.51	1.28±0.47	0.12	0.528
10% / 40	1.40±0.54	1.24±0.48	0.16	0.566
10% / 50	1.45±0.53	1.28±0.48	0.12	0.547
10% / 60	1.39±0.52	1.29±0.49	0.11	0.531
10% / 70	1.40±0.56	1.28±0.51	0.12	0.572
10% / 80	1.43±0.57	1.32±0.53	0.08	0.572
12.5% / 30	1.37±0.51	1.25±0.47	0.15	0.532
12.5% / 40	1.40±0.53	1.25±0.48	0.15	0.553
12.5% / 50	1.37±0.52	1.22±0.47	0.18	0.551
12.5% / 60	1.43±0.52	1.33±0.49	0.07	0.524
12.5% / 70	1.40±0.54	1.28±0.49	0.12	0.551
12.5% / 80	1.40±0.54	1.30±0.50	0.10	0.548
15% / 30	1.42±0.58	1.31±0.54	0.09	0.588
15% / 40	1.41±0.60	1.26±0.54	0.14	0.616
15% / 50	1.43±0.60	1.29±0.54	0.11	0.609
15% / 60	1.38±0.57	1.30±0.54	0.10	0.577
15% / 70	1.39±0.62	1.27±0.57	0.13	0.633
15% / 80	1.39±0.63	1.29±0.59	0.11	0.640

Table 4.5: Optimization and signal shapes systematic calculation results. The first column represents the extracted branching fraction using the corrected signal shapes both for generating toys and for fitting; the second column is the expected branching fraction where the corrected shapes are used only for generating toys; the third column is the systematic error associated to the signal shapes, calcualted as the difference between the branching fractions extracted in the two different ways; fourth column is the sum in quadrature of statistical and systematic error.

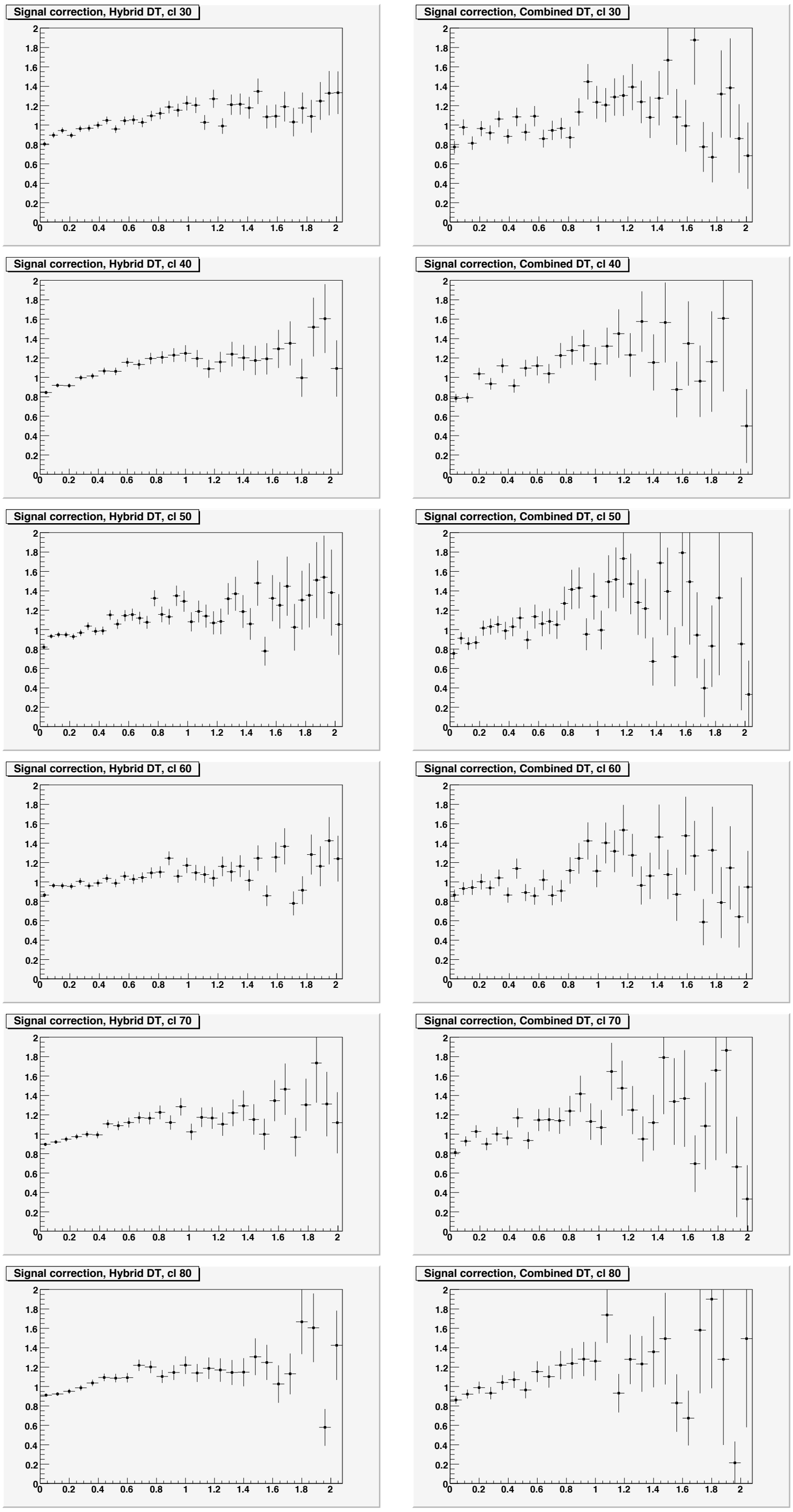

Figure 4.5: Correction plot for E_{extra} signal shapes for different values of minimum energy cluster (rows, from 30 MeV to 80 MeV). In the left plots the correction is taken from the "Hybrid" double tag; the right column shows the correction taken from "Hadronic" double tag.

4.4 Systematics uncertainty in background shapes

To evaluate this systematic uncertainty we use the following procedure:

- Each bin content of the “nominal” shape is the reponse of our experiment but we can have a different value from an hypotetical repetion of the experiment. We generate 1000 toy experiments, where each bin content in the background E_{extra} shape is randomly extracted from a gaussian distribution centered around the value of the “nominal” shape. We consider as standard deviation of the gaussian distribution the uncertainty on the bin content. The uncertainty comes from Monte Carlo and experimental data statistic uncertainty, propagated with the scaling factors coming from the m_{ES} fits (the uncertainties on the latter are included as well). We repeat this generation for the four considered channel, in order to have 1000 set of four background templates.
- for each set of templates we generate 1000 versions of E_{extra} distribution for signal and background (using the corrected signal templates), and we fit the toys using the nominal background templates; then we evaluate the average branching fraction for each set of templates
- we obtain a distribution of 1000 averaged branching fraction ($< BF >_i$), coming from randomly extracted background templates. The distribution of $< BF >_i$ is gaussian, with mean value of 1.4×10^{-4}, as expected. Fitting the distributions we use the width of the gaussian as systematic uncertainty.

Also in this case, we repeat the procedure for the set of purity requirements and for both the minimum cluster values of 30 MeV and 60 MeV, using the appropriate optimized selection requirements. Fig. 4.6 shows the fitted distribution of the $< BF >_i$ at different purities, while in table 4.6 we report the results showing the extracted branching fraction, the statistical uncertainty, the signal shape systematic uncertainty, the systematic uncertainty coming from background shapes, and the total uncertainty (sum in quadrature of the three uncertainties). We find the minimum total uncertainty with 12.5% purity. Both 30 MeV and 60 MeV choices for the minimum cluster energy show consistent results. We choose the 60 MeV option, having a smaller uncertainty in the signal shape. Using this configuration, and assuming a true value of the branching fraction to be 1.4×10^{-4}, we expect a statistical uncertainty of 0.52×10^{-4} and a systematic uncertainty of 0.31×10^{-4}.

Purity req	Min. cl. energy (MeV)	BF extraction	sig syst	bkg syst	total error
5%	30	1.36±0.57	0.16	0.36	0.694
	60	1.39±0.59	0.11	0.36	0.700
7.5%	30	1.39±0.55	0.14	0.33	0.659
	60	1.42±0.55	0.07	0.32	0.644
10%	30	1.40±0.51	0.12	0.30	0.607
	60	1.39±0.52	0.11	0.30	0.612
12.5%	30	1.37±0.51	0.15	0.29	0.607
	60	1.43±0.52	0.07	0.30	0.603
15%	30	1.42±0.58	0.09	0.33	0.674
	60	1.38±0.57	0.10	0.32	0.660

Table 4.6: Background shapes systematic calculation results. We report: 1) the extracted branching fraction and the statistical error using the corrected signal shapes, 2) the systematic error coming from signal shapes as calcualted in section 4.3, 3) the systematic error associated to the background shapes; 4) the sum in quadrature of the three errors.

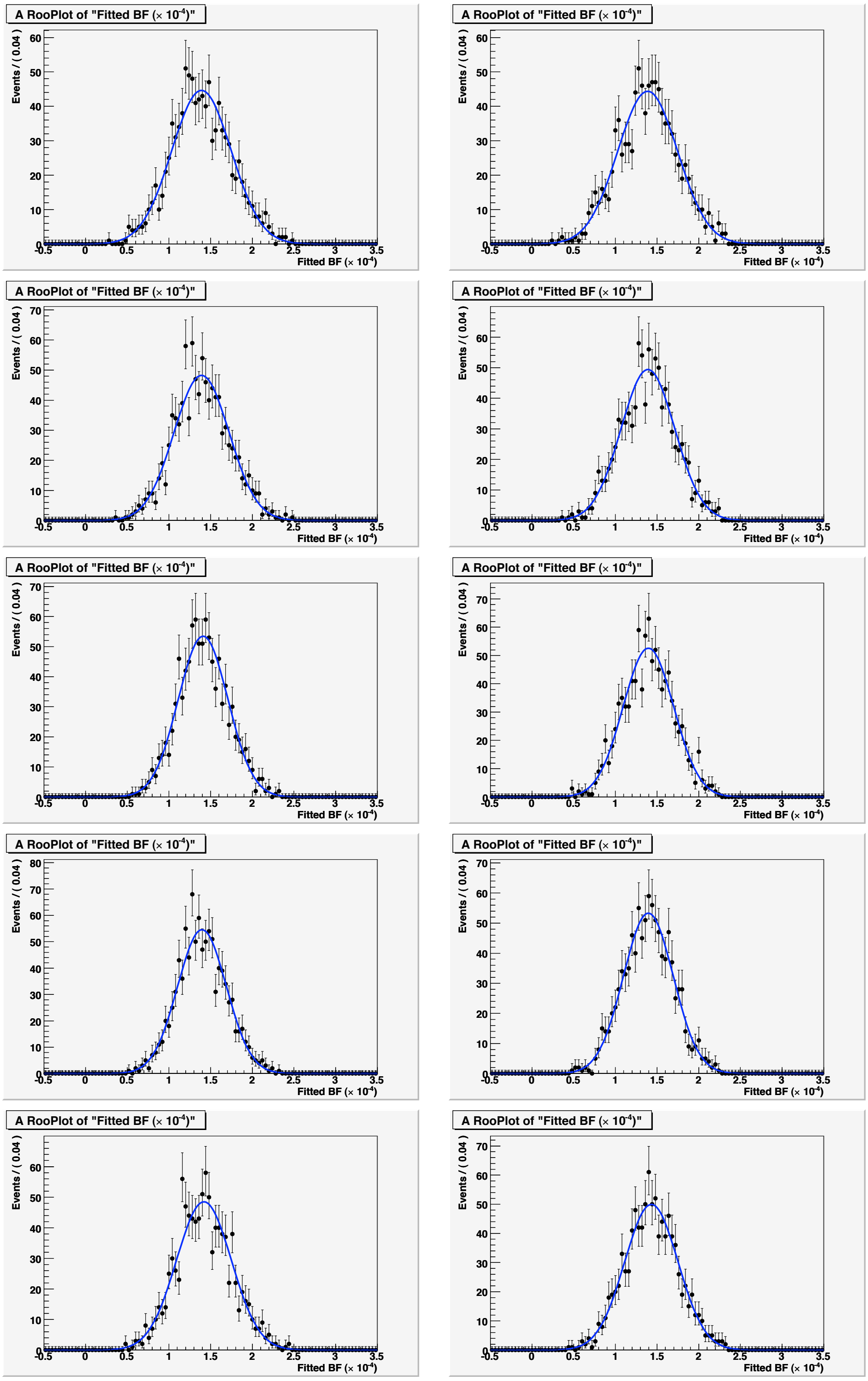

Figure 4.6: Distribution of averaged extracted branching fraction coming from the differents randomly extracted background templates. The distribution are fitted with a gaussian function. Left column if for minimum cluster energy of 30 MeV, right column for 60 MeV. The mean values are from top (30MeV-60MeV): 1.39-1.39 (purity 5%), 1.39-1.39(purity 7.5%), 1.41-1.40(purity 10%), 1.40-1.40(purity 12.5%), 1.42-1.43(purity 15%).

Chapter 5

Efficiencies and final results

In this chapter we report the selection efficiencies and the E_{extra} plots related to the selected data sample. The breakdown of the peaking background is reported and then we describe the statistical method we will use to extract the branching fraction of the $B \to \tau\nu$ decay, looking at data sample in the signal E_{extra} window.

5.1 Signal selection efficiency

We define the efficiency as the ratio of the number of signal Monte Carlo events passing the selection criteria on the tagged events that have a m_{ES} peaking B_{tag} candidate. Using the Monte Carlo truth we divide our signal sample in each of the true τ decay channels. The cross-feed among the modes is taken into account in the computation of total efficiency. The pion channel suffers an high cross-feed from the $\tau^- \to \mu^-\nu\bar{\nu}$ events due to the PID inefficiency, and from the $\tau^- \to \rho^-\nu$ events when the π^0 is not reconstructed.

The total efficiency for each reconstructed τ mode is:

$$\epsilon_i = \sum_{j=1}^{n_{dec}} \epsilon_i^j f_j, \tag{5.1}$$

where ϵ_i^j is the efficiency to reconstruct as mode i a signal event with a τ that actually decayed in mode j; $n_{dec} = 5$ is the number of generated τ decay mode and f_j is fractions of τ decaying in the j mode at the tag selection level as reported in table 3.3. Table 5.1 shows all the efficiencies and cross-feed for the τ decay mode analyzed.

5.2 Background prediction

In order to determine the amount of background we use the final selected data sample with $E_{extra60}$ between 0 and 2.0 GeV. We fit the m_{ES} distribution in data and B^+B^- Monte Carlo sample with an Argus plus a Crystal Ball both for $E_{extra60}$ sideband events ($E_{extra60} > 0.5$ GeV) and for all events. We extract the non peaking component of data sample and Monte Carlo sample from the all-events fit and the peaking component data/Monte Carlo ratio from the $E_{extra60}$ sideband fit, following the procedure described in sec 3.5. Fig. 5.1 shows the m_{ES} distribution after selection requirements for data and B^+B^- Monte Carlo samples.

mode	$e\nu\bar{\nu}(\%)$	$\mu\nu\bar{\nu}(\%)$	$\pi\nu(\%)$	$\rho\nu(\%)$
$e\nu\bar{\nu}$	**63.1±0.5**	0.39±0.07	0.30±0.06	0.03±0.02
$\mu\nu\bar{\nu}$	0.05±0.02	**56.2±0.5**	1.31±0.01	0.05±0.02
$\pi\nu$	0.16±0.05	2.5±0.2	**35.1±0.6**	4.3±0.3
$\rho\nu$	0.36±0.05	3.4±0.2	6.2±0.2	**22.2±0.4**
other	0.28±0.05	2.08±0.14	1.23±0.11	6.8±0.2
all τ dec.:	**12.0±0.5**	**12.2±0.6**	**6.6±0.7**	**8.1±0.5**
total:	**39.0±1.2**			

Table 5.1: Efficiency of different selections (columns) for the most relevant τ decay channels (rows). The last two rows show the total efficiency of the single selections, weighted by the decay abundance at the tag selection level, and the total efficiency. The uncertainty are statistical only.

5.2.1 Peaking background study

We analyze the peaking background passing the selection requirements, looking at the Monte Carlo truth to identify the contribution from different B decays. In tables 5.2-5.5 we report the ratio of each different contribution for the background events that passes the selection, both for $E_{extra60} < 2.0\,\mathrm{GeV}$ and for $E_{extra60} < 0.4\,\mathrm{GeV}$. In figg.5.2-5.5 we report the break-down of the peaking background, distributed in E_{extra} . We select the peaking component of the background from B^+B^- Monte Carlo using the same *Truth-matching* requirements we described in subsection 3.4.3.2.

B decay mode	% ($E_{extra60} < 0.4\,\mathrm{GeV}$)	% ($E_{extra60} < 2\,\mathrm{GeV}$)
$Db \to c, e$	43.0	27.4
$D^{*}b \to c, e$	42.0	57.3
$D^{**}b \to c, e$	3.0	1.0
$Db \to c, \mu$	0	0.1
$D^{*}b \to c, \mu$	1.0	0.3
$D^{**}b \to c, \mu$	0	0
$Db \to c, \tau$	3.0	2.0
$D^{*}b \to c, \tau$	4.0	5.0
$D^{**}b \to c, \tau$	0	0.3
$V_{ub}e$	3.0	2.6
$V_{ub}\mu$	1.0	0.1
$V_{ub}\tau$	0	0.3
Charmed hadronic	0	3.2
Charmless hadronic	0	0

Table 5.2: Breakdown of the decay modes from B^+B^- Monte Carlo at the final selection stage in two different $E_{extra60}$ windows. Electron channel.

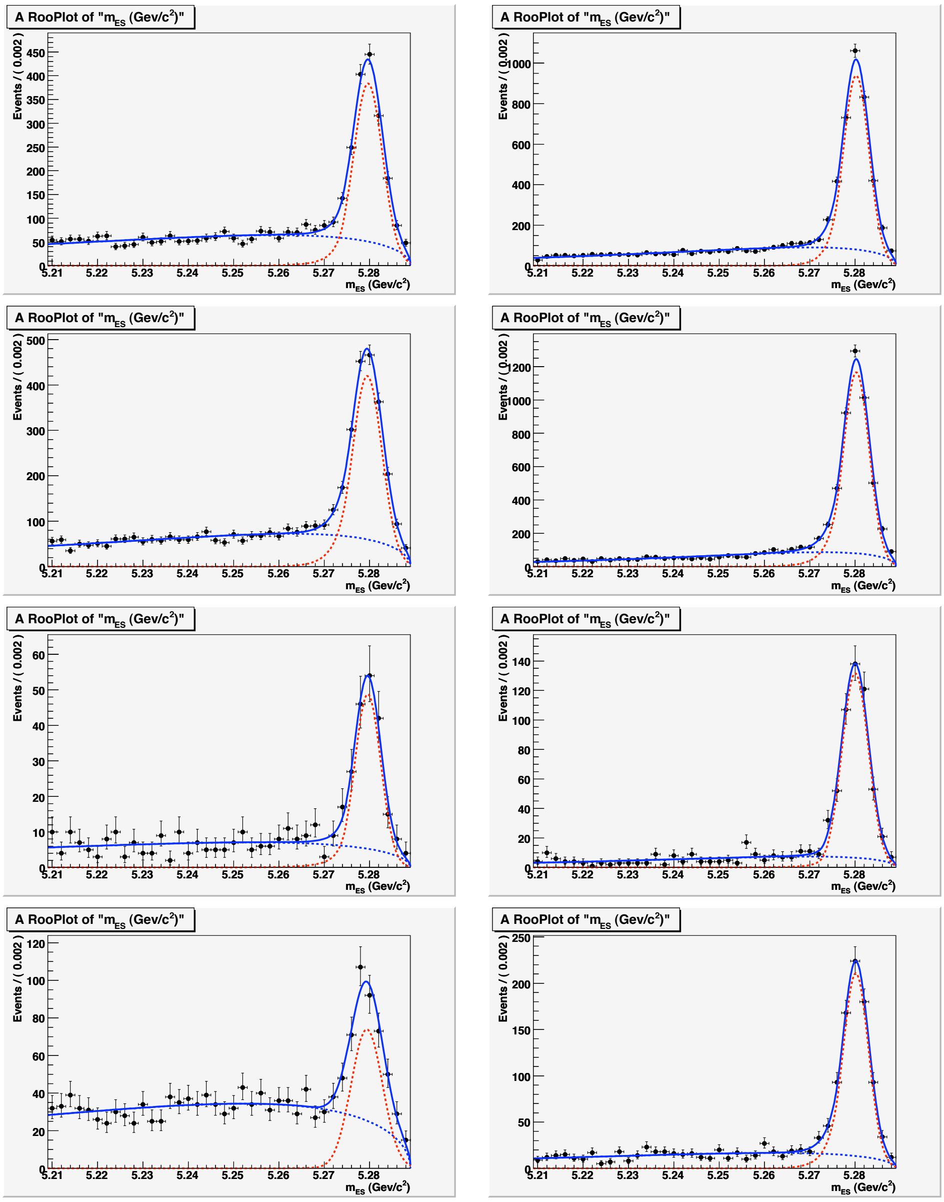

Figure 5.1: m_{ES} distributions after the selection requirements. The left column are data samples, and the right column are B^+B^- Monte Carlo samples. The rows represent the four channel: from top to bottom, e, μ, π and ρ.

B decay mode	% ($E_{extra60} < 2$ GeV)	% ($E_{extra60} < 0.4$ GeV)
$Db \to c, e$	0.8	0.2
$D^{*}b \to c, e$	1.5	0.7
$D^{**}b \to c, e$	0	0.9
$Db \to c, \mu$	26.1	23.8
$D^{*}b \to c, \mu$	53.1	60.4
$D^{**}b \to c, \mu$	0	0.9
$Db \to c, \tau$	2.3	1.8
$D^{*}b \to c, \tau$	3.8	4.2
$D^{**}b \to c, \tau$	0	0
$V_{ub}e$	0	0
$V_{ub}\mu$	3.8	2.7
$V_{ub}\tau$	2.3	0.3
Charmed hadronic	4.6	4.7
Charmless hadronic	0.8	0.1

Table 5.3: Breakdown of the decay modes from B^+B^- Monte Carlo at the final selection stage in two different $E_{extra60}$ windows. Muon channel.

B decay mode	% ($E_{extra60} < 0.4$ GeV)	% ($E_{extra60} < 2$ GeV)
Semileptonic $b \to c, e$	5.9	5.0
Semileptonic $b \to c, \mu$	32.3	26.0
Semileptonic $b \to c, \tau$	0	1.4
$V_{ub}e$	0	0.2
$V_{ub}\mu$	0	4.4
$V_{ub}\tau$	2.9	0.3
Charmed hadronic	26.5	53.3
Charmless hadronic	32.3	9.5

Table 5.4: Breakdown of the decay modes from B^+B^- Monte Carlo at the final selection stage in two different $E_{extra60}$ windows. Pion channel.

B decay mode	% ($E_{extra60} < 0.4$ GeV)	% ($E_{extra60} < 2$ GeV)
Semileptonic $b \to c, e$	10.6	3.1
Semileptonic $b \to c, \mu$	19.1	11.6
Semileptonic $b \to c, \tau$	12.8	4.3
$V_{ub}e$	0	0.3
$V_{ub}\mu$	4.2	0.6
$V_{ub}\tau$	4.2	0.3
Charmed hadronic	44.7	73.1
Charmless hadronic	4.3	6.6

Table 5.5: Breakdown of the decay modes from B^+B^- Monte Carlo at the final selection stage in two different $E_{extra60}$ windows. Rho channel.

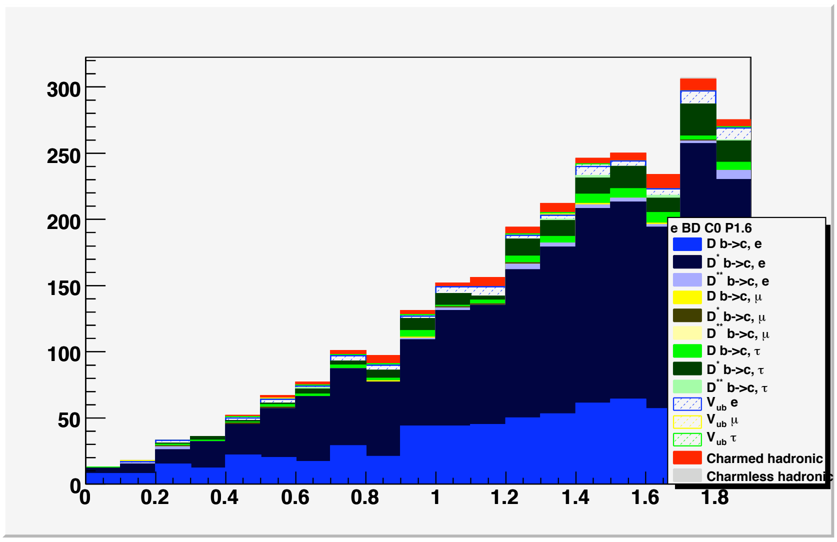

Figure 5.2: Breakdown of the decay modes from B^+B^- Monte Carlo at the final selection stage. Electron channel.

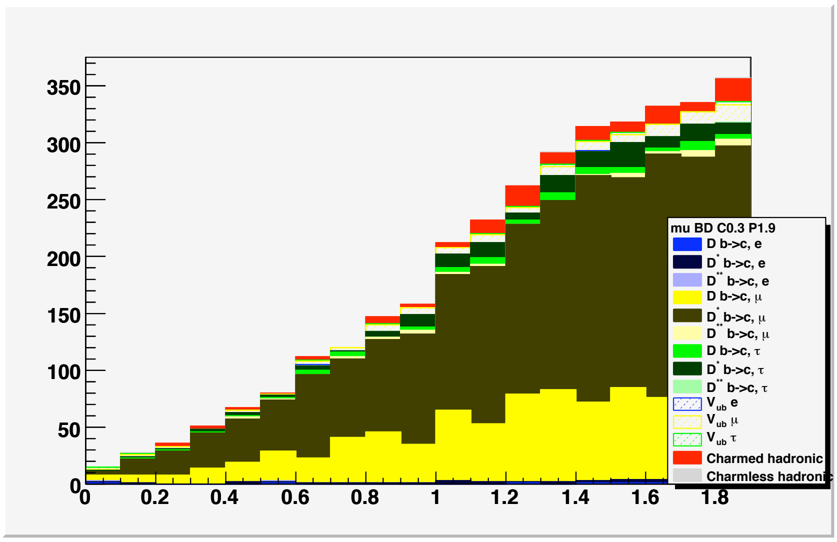

Figure 5.3: Breakdown of the decay modes from B^+B^- Monte Carlo at the final selection stage. Muon channel.

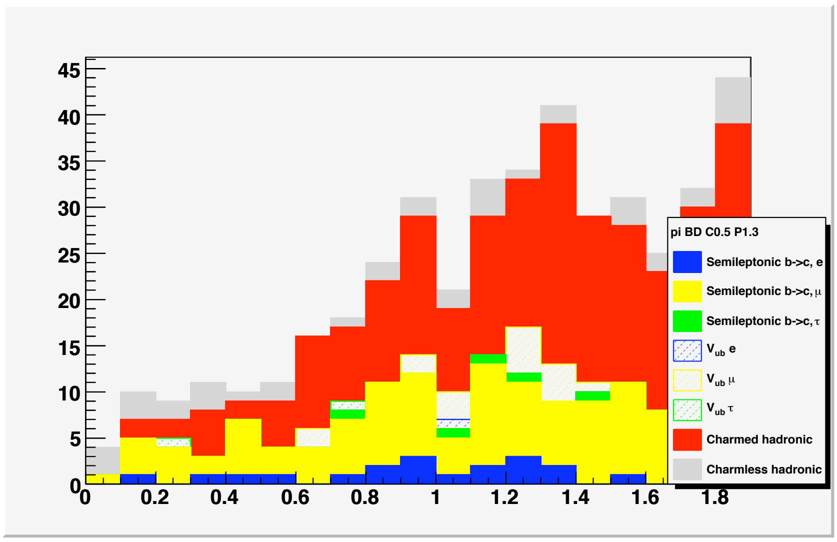

Figure 5.4: Breakdown of the decay modes from B^+B^- Monte Carlo at the final selection stage. Pion channel.

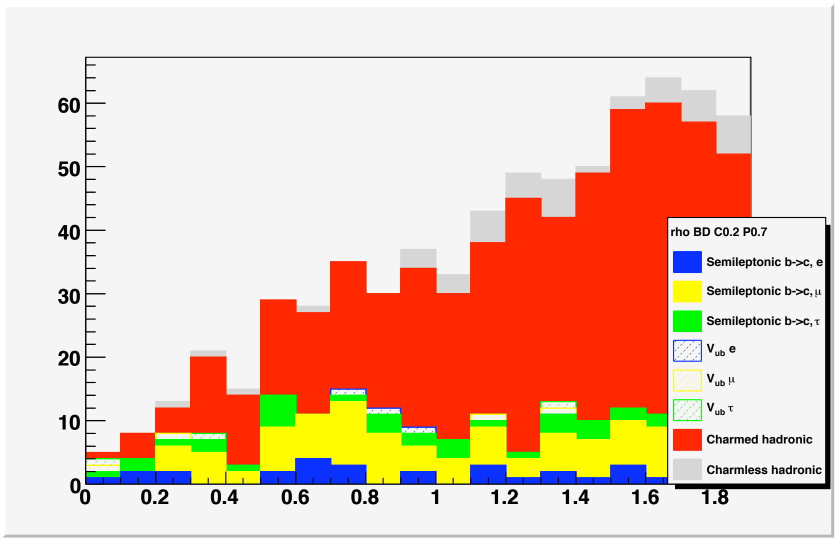

Figure 5.5: Breakdown of the decay modes from B^+B^- Monte Carlo at the final selection stage. Rho channel.

5.2.2 $E_{extra60}$ distributions

Figures 5.6-5.7 show the final E_{extra} distribution for all decay modes. The total E_{extra} distribution is shown in fig.5.10. In table 5.6 we report the number of expected background events and the number of expected signal events, using a branching fraction hypotesis of 1.4×10^{-4}. The expected signal and background events are calculated in two $E_{extra60}$ windows (120 MeV and 240 MeV).

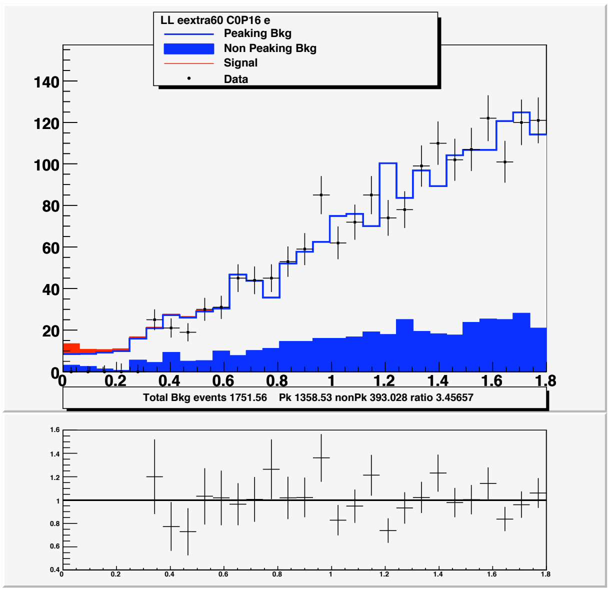

Figure 5.6: E_{extra} distribution for the electron channel after the selection requirements. The blue solid histogram is the non peaking background, the empty histogram is the peaking background, the red histogram is the number of expected signal events with a branching fraction hypotesis of 1.4×10^{-4} and the dots are data. The first bins in data histogram are set to zero (blinded).

channel	exp. sig 120 MeV	exp. sig 240 MeV	exp. bkg 120 MeV	exp. bkg 240 MeV
$e\nu\bar{\nu}$	7.1 ± 2.7	9.8 ± 3.1	17.0 ± 3.3	36.0 ± 4.9
$\mu\nu\bar{\nu}$	6.4 ± 2.5	9.0 ± 3.1	16.3 ± 3.2	39.0 ± 4.9
$\pi\nu$	3.3 ± 1.6	4.7 ± 2.4	5.3 ± 1.6	10.4 ± 2.3
$\rho\nu$	3.8 ± 1.8	5.4 ± 2.5	7.5 ± 2.0	18.5 ± 3.2
total	20.6 ± 4.4	28.9 ± 5.6	46.1 ± 5.3	103.9 ± 7.8

Table 5.6: Expected signal and predicted background events after selection, assuming $\mathcal{B}(B \rightarrow \tau\nu) = 1.4 \times 10^{-4}$.

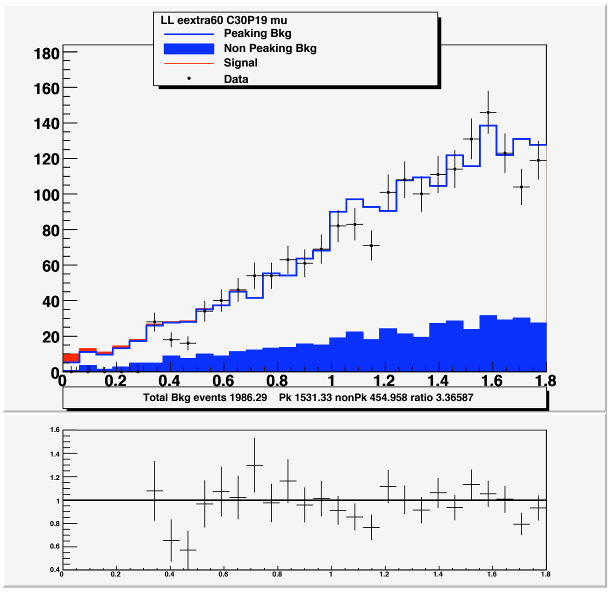

Figure 5.7: E_{extra} distribution for the muon channel after the selection requirements. The blue solid histogram is the non peaking background, the empty histogram is the peaking background, the red histogram is the number of expected signal events with a branching fraction hypothesis of 1.4×10^{-4} and the dots are data. The first bins in data histogram are set to zero (blinded).

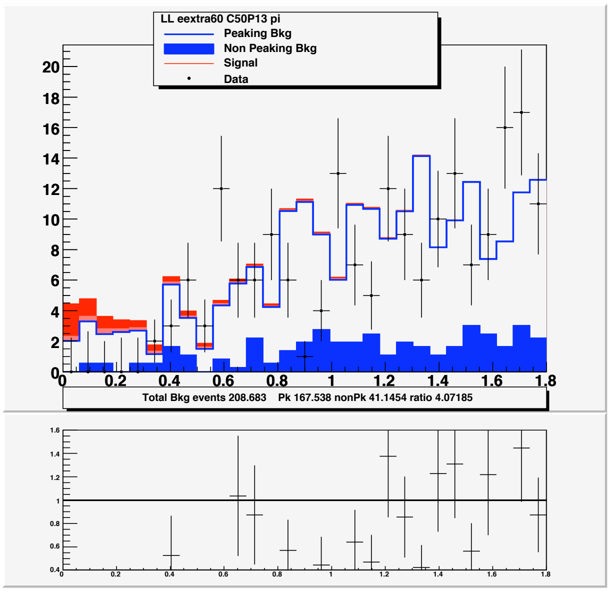

Figure 5.8: E_{extra} distribution for the pion channel after the selection requirements. The blue solid histogram is the non peaking background, the empty histogram is the peaking background, the red histogram is the number of expected signal events with a branching fraction hypothesis of 1.4×10^{-4} and the dots are data. The first bins in data histogram are set to zero (blinded).

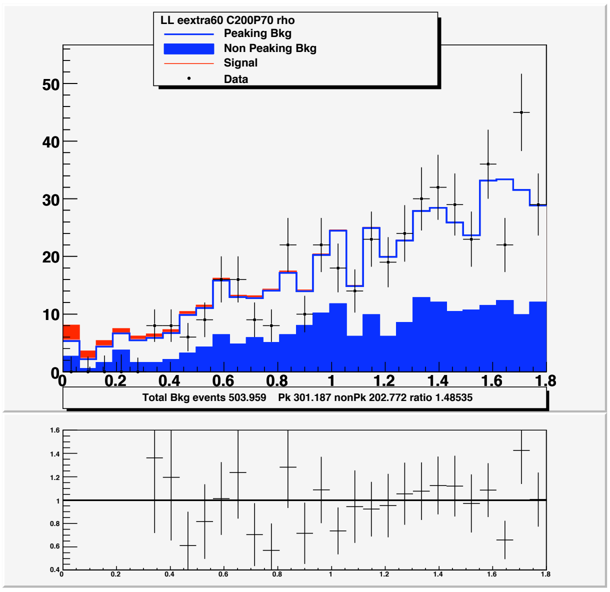

Figure 5.9: E_{extra} distribution for the rho channel after the selection requirements. The blue solid histogram is the non peaking background, the empty histogram is the peaking background, the red histogram is the number of expected signal events with a branching fraction hypotesis of 1.4×10^{-4} and the dots are data. The first bins in data histogram are set to zero (blinded).

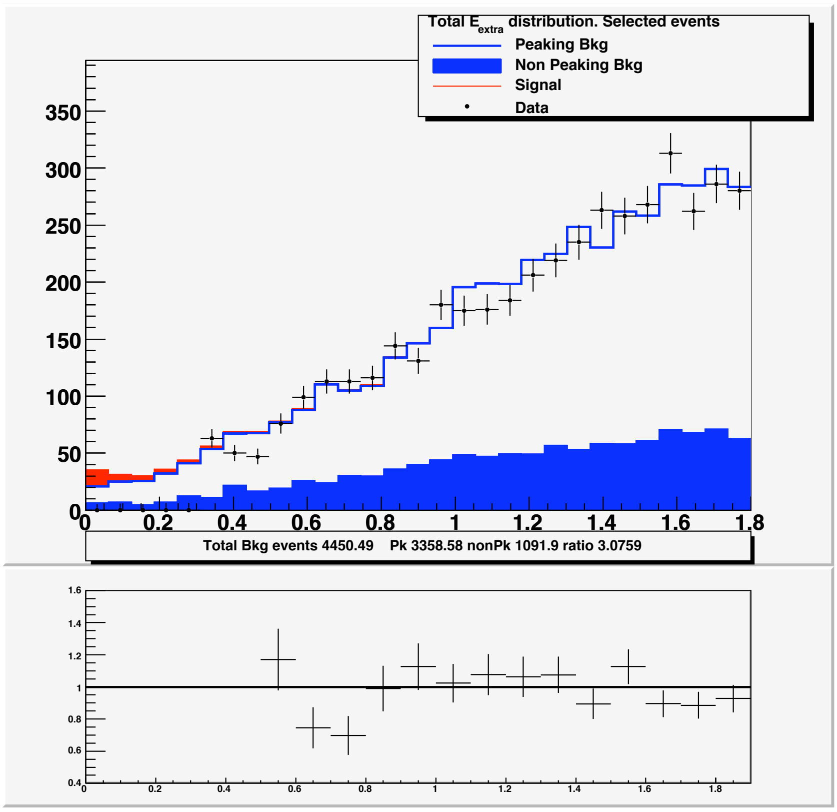

Figure 5.10: Total E_{extra} distribution (four channels combined) after the selection requirements. The blue solid histogram is the non peaking background, the empty histogram is the peaking background, the red histogram is the number of expected signal events with a branching fraction hypotesis of 1.4×10^{-4} and the dots are data. The first bins in data histogram are set to zero (blinded).

5.3 Branching fraction extraction

To extract the $B \to \tau\nu$ branching fraction we look at the data distribution and use an unbinned extend maximum likelihood fit on the E_{extra} distribution. The likelihood function for the N_k candidates reconstructed in one of the four channels k is the same of equation 3.11. We report it here for completeness:

$$\mathcal{L}_k = e^{-N'_k} \prod_{i=1}^{N_k} \left\{ N_{S,k} \mathcal{P}^S_{i,k} + N_{C,k} \mathcal{P}^C_{i,k} \right\} \tag{5.2}$$

where N'_k is the observed number of events, $N_{S,k}$ is the number of signal events and $N_{C,k}$ is the number of background events, for the τ decay category k. The number of background events in each category are floated independently in the fit. The signal yields are constrained to a single branching ratio:

$$N_{S,k} = N_{B\overline{B}} \cdot \epsilon_{tag,k} \cdot \epsilon_{reco,k} \times BF \tag{5.3}$$

where $N_{B\overline{B}}$ is the number of $B\overline{B}$ pairs in the data sample, ϵ_{tag} is the tagging efficiency, $\epsilon_{reco,k}$ is the category dependent reconstruction efficiency, and BF is the $B^+ \to \tau^+\nu$ branching fraction. $N_{B\overline{B}}$, $\epsilon_{tag,k}$, $\epsilon_{reco,k}$ are obtained as described in the previous chapters, and they are fixed in the fit, leaving the BF floating. The probability density functions (PDFs) $\mathcal{P}^S_k$, $\mathcal{P}^C_k$ for signal and background respectively, are the histogram PDFs in $E_{extra60}$ used in the optimization step.

Conclusions

The analysis of the leptonic $B \to \tau\nu$ decay is based on the whole BABAR dataset, collected in the period 1999-2007 with the BABAR detector at the PEP-II asymmetric-energy e^+e^- collider. To evaluate the behavior of signal and background events we use the real data sample and several MonteCarlo samples which describes the different contribution of signal and bakcground sources.
We reconstruct for each event a B meson (B_{tag}) using hadronic decay channels and search for the $B \to \tau\nu$ decay in the rest of the event. We reconstruct the τ lepton through its decays: $\tau^- \to e^-\nu\bar{\nu}$, $\tau^- \to \mu^-\nu\bar{\nu}$, $\tau^- \to \pi^-\nu$ and $\tau^- \to \rho^-\nu$. Using B_{tag} reconstruction variables and kinematics and topological variable related to the B_{sig} side we identify estimators used to enhance signal events and reject background. The E_{extra} variable, defined as the energy of the charged tracks and the neutral cluster not assigned to any B meson, is the most discriminating variable. We evaluate the number of signal events for each level of selection fitting the E_{extra} distribution of signal plus nackground. We generate an high number of E_{extra} distributions for each selection level, using a branching fraction hypotesis. Fitting those distribution we evaluate the uncertainties associated to the branching fraction for each selection level. Systematics errors are taken into account, and the lower global error defines the best selection level. Imposing the PDG world average for the branching fraction we expect:

$$\mathcal{B}(B \to \tau\nu) = (1.40 \pm 0.52(\text{stat}) \pm 0.32(\text{syst.})) \times 10^{-4}$$

We can calculate the $B \to \tau\nu$ branching fraction fitting the final E_{extra} distribution of data. The fit is perfomed by maximizing a *likelihood* that takes into account the E_{extra} shapes for signal and background, evaluated from data sideband and MonteCarlo. The present analysis is still under the checking of a BABAR collaboration review committe, so the procedure must stay *blind* to the signal region in real data. As soon as the review procedure ends, we will extract the final result.

List of Figures

List of Tables

Bibliography

[1] B. Aubert *et al.,*(*BABAR*Collaboration), *Phys. Rev.* ***D77*** 011107 (2008).

[2] ArXiv:0809,4027 (2009) Submitted to PRD

[3] W.S. Hou, *Phys. Rev.* ***D48***, 2342 (1993).

[4] T.D. Lee, C.N. Yang, *Phys. Rev.* 104(1956)254.

[5] C.S. Wu et al., *Phys Rev.* 106(1957)1413.

[6] R.P. Feynmann, M. Gell'Mann, *Phys. Rev.* 109(1958)193.

[7] S.L. Glashow, Nucl. Phys.**22**,579 (1961);
S. Weinberg, Phys. Rev. Lett. **19**,1264 (1967);
A. Salam, in *Proc. 8th Nobel Symp.*, ed. N. Swartholm,
Almquist and Wiksells, Stockholm (1968).

[8] Perkins, *Introduction to High Energy Physics*, (1987)

[9] N. Cabibbo, Phys. Rev. Lett. **10**,531 (1963).

[10] M. Kobayashi and T.Maskawa, Prog. Th. Phys.**49**,652 (1973).

[11] L.L. Chau and W.Y.Keung, Phys. Rev. Lett. **53**,1802 (1984).

[12] L. Wolfenstein, Phys. Rev. Lett. **51**,1945 (1983).

[13] A.J. Buras, M.E. Lautenbacher and G. Ostermaier, Phys. Rev. D **50**,3433 (1994).

[14] J.D. Bjorken, Phys. Rev. D **39**,1396 (1989).

[15] C. Jarlskog and R. Stora, Phys. Lett. B **208**,268 (1988).

[16] C. Amsler *et al.,*(Particle Data Group), Phys. Lett. B **666**, 1 (2008).

[17] J. Charles *et al.,*[CKMfitter group], Eur. Phys. J. **C41**,1 (2005) and updates in `http://ckmfitter.in2p3.fr/`.

[18] A. Gray *et al.,*[HPQCD Collaboration], Phys. Rev. Lett. **95** 212001 (2005).

[19] Y. Kao and T. Takeuchi [arXiv:0909.0042] (2009).

[20] K. Hara (Belle Collaboration) [arXiv:0810.3301] (2008).

[21] J. Abdallah *et al.,*, Phys. Lett. B **552**, Issues 3-4, 127 (2003).

[22] The BABAR Collaboration, B. Aubert *et al.,*Nucl. Instrum. Methods **A479**,1 (2002).

[23] P.F. Harrison *et al.,*, The BABAR physics book: Physics at an Asymmetric B factory, SLAC-R-9594 (1998).

[24] P. Oddone *Annals N.Y. Acad. Sci.* **578**, 237 (1989).

[25] PEP-II - An Asymmetric B Factory, Conceptual Design Report, SLAC-418, LBL-5379 (1993).

[26] T. Mattison *et al.,*, background Measurements during PEP-II Commisioning, *Proceedings of the IEEE Particle Accelerator Conference (PAC99)*, New York, N.Y., USA (1999).

[27] P. Coyle *et al.,*Nucl. Instr. and Methods A **343**, 292 (1994).

[28] G. Battistoni *et al.,*, Nucl. Instr. and Methods A **187**, 277 (1981).

[29] T. Brandt, “Likelihood Based Electron Identification”, BABAR Analysis Document #396 (2002).

[30] T. Brandt, “Studies of a Neural Net Based Muon Selector for the BaBar Experiment”, BABAR Analysis Document #474 (2004).

[31] `http://www.slac.stanford.edu/BFROOT/www/Physics/Tools/Pid/Hadrons/Description_of_the_LH_selectors.html`

[32] `http://www.slac.stanford.edu/BFROOT/www/Physics/Tools/generators/GenFwkInt/GenFwkInt.html`.

[33] `http://geant4.web.cern.ch/geant4/`.

[34] A. Drescher *et al.,*, Nucl. Instrum. Methods **A237**, 464 (1985).

[35] H. Albrecht *et al.,*[ARGUS Collaboration], Phys. Lett. **B185**,218 (1987).

[36] D. Antreasyan, Crystall Ball Note 321 (1983).

[37] G. C. Fox and S. Wolfram, Nucl.Phys. **B149** (1979) 413

[38] A. Hocker *et al.,*“TMVA User Guide”, arXiv physics 0703039, CERN-OPEN-2007-007 (2007)